2007

Plasma Processing For Retention Of Nanostructures

Viswanathan Venkatachalapathy
University of Central Florida

PLASMA PROCESSING FOR RETENTION OF NANOSTRUCTURES

by

VISWANATHAN VENKATACHALAPATHY
B.E. University of Rajasthan, 1999
M.E. Bharathidasan University, 2002

A dissertation submitted in partial fulfillment of the requirements
for the degree of Doctor of Philosophy
in the Department of Mechanical, Materials and Aerospace Engineering
in the College of Engineering and Computer Science
at the University of Central Florida
Orlando, Florida

Spring Term
2007

Major Professor: Sudipta Seal

ABSTRACT

Plasma spray processing is a technique that is used extensively in thermal barrier coatings on gas and steam turbine components, biomedical implants and automotive components. Many processing parameters are involved to achieve a coating with certain functionality. The coating could be required to function as thermal barrier, wear resistant, corrosion resistant or a high temperature oxidation resistant coating. Various parameters, such as, nozzle and electrode design, powder feeding system, spray distances, substrate temperature and roughness, plasma gas flow rates and others can greatly alter the coating quality and resulting performance. Feedstock (powder or solution precursor) composition and morphology are some of the important variables, which can affect the high end coating applications. The amount of heat a plasma plume has to offer to the particles being processed as a coating depends primarily on the dissociation of the atoms of gaseous mixtures being used to create the plasma and the residence time required for the particle to stay in the flame. The parameters that are conducive for nanostructured retention could be found out if the residence time of the particles in the flame and the available heat in the plume for various gas combinations could be predicted. If the feedstock is a liquid precursor instead of a powder feedstock, the heat that has to be offered by the plasma could be increased by suitable gas combination to achieve a good quality coating.

Very little information is available with regard to the selection of process parameters and processing of nano materials feedstock to develop nanostructured coatings using plasma spray. In this study, it has been demonstrated that nano ceramics or ceramic composites either in the form of coatings or bulk free form near net components could be processed using DC plasma spray. For powder feedstock, analytical heat transfer calculations could predict the particle states

for a given set of parameters by way of heat input from the plasma to the particles. The parameter selection is rendered easier by means of such calculations. Alumina nano ceramic particles are processed as a coating. During Spray drying, a process of consolidation of nano alumina particles to spherical agglomerates, parameter optimization for complete removal of moisture has been achieved. The parameters are tested for alumina nanoparticles with a plasma torch for the veracity of calculations. The amount of heat transfer from the surface of the agglomerates to the core has been quantified as a function of velocity of particles. Since preparation of nanostructured feedstock for plasma spray is expensive and cumbersome, alternative solution precursor route for direct pyrolysis of precursor to coating has been studied in case of nanocrystalline rare earth oxides. Thus, it has also been shown by this research that nanostructured coatings could be either from a powder feedstock or a solution precursor feedstock. MoSi2-Si3N4, Ni-Al2O3, W-HfC nano ceramic composite systems have been processed as a bulk free form nanocomposite with 60-70% retained nanostructures. The importance of selection of substrates, roughness and the substrate temperature for development of free form bulk components has been highlighted. The improvement in mechanical and high temperature properties associated with having such nanostructured coatings or bulk nanocomposites are revealed. These nanostructured coatings are known for their low thermal conductivity, high wear resistance and can be potentially used as steam and gas turbines coatings for improved thermal efficiency. In summary, bulk nanocomposite through plasma spray processing is a viable alternative to conventional processes such as sintering, HIP for high fracture toughness and hardness applications.

Dedicated to my Parents

ACKNOWLEDGMENTS

I would like to thank my faculty advisor, Prof. Sudipta Seal, for providing me the financial and moral support and also involved me in some of the research projects at plasma Nanomanufacturing laboratory. Without his motivation and guidance this research work would not have been possible.

I am very grateful to Dr. Anirudha Vaidya at Siemens Power Generation, Orlando for his help with the experiments and being on my thesis committee. I also thank Dr. Raj Vaidyanathan, Dr. Alfons Schulte, Dr. Linan An and Dr. Samar Jyoti Kalita for being on my thesis committee.

I thank Materials Characterization Facility (MCF) at UCF for offering the characterization facilities required for conducting this research work. Also, I would like to acknowledge all the students in the Surface Engineering and Nanotechnology Facility (SNF) and my friends for their cooperation and support. I would like to thank Keith Rea for his help in Plasma nanomanufacturing laboratory. I also would like to acknowledge the help of Dr. Arvind Agarwal and Dr. Tapas Laha at Florida International University, Miami. The experimental help with vacuum plasma spray by Plasma Process Inc, Huntsville, Alabama is acknowledged.

I am grateful for financial support by the Office of Naval Research Young Investigator Award Program, ONR 000140210591 and DURIP N000140310858 and Siemens Power Generation Inc. Orlando.

TABLE OF CONTENTS

LIST OF FIGURES

LIST OF TABLES

LIST OF ABBREVIATIONS

APS - Air Plasma Spray

DE - Deposition Efficiency

HVOF- High Velocity Oxy Fuel

PEG - Poly Ethylene Glycol

SCFH - Standard Cubic Feet per Hour

SLM - Standard Liters per Minute

SPPS - Solution Precursor Plasma Spray

TBC - Thermal Barrier Coatings

VPS - Vacuum Plasma Spray

Z - Atomic number

CHAPTER 1 INTRODUCTION

1.1. Nanocrystalline Materials: Introduction and Significance

Nanocrystalline materials are characterized by a grain size or particulate size of up to about 100 nm. These materials exhibit enhanced mechanical[1-3], magnetic[1] elevated temperature[4], optical[5,6] and excellent catalytic properties[7]. The commercial applications of nanocomposite beyond the boundaries of Materials Science Laboratories lie on the successful consolidation of these materials into bulk-sized components preserving the nanostructures. The traditional consolidation techniques have a strong limitation of not being able to retain the nano grain size due to the problem of grain growth.

The density of the green compact depends on the frictional forces of the powder particles that are originated from electrostatic, Vander Waals and surface adsorption forces. These forces are significantly high in nanoparticles forming hard agglomerates and inter-agglomerate which are relatively large. Based on the thermodynamic treatment of the shrinkage of the pore, Mayo[8] suggested that the finest pore size usually yields the highest densification rate. Such large pores require not only higher temperature but also prolong sintering times for their successful elimination; consequently, it becomes difficult to retain the grain size in the nanometer domain.

Large pores undergo pore boundary separation that restricts attaining the full density in the consolidated nanoparticles[6,9]. During sintering of nanoparticles, pores smaller than the critical size shrink[10], while larger pores undergo the pore-boundary separation. The fraction of grain boundaries in nanomaterials is large compared to that for coarse-grained materials. The density of the grain boundary regions is less than the grain interior due mainly to the relaxation of atoms

in the grain boundaries, and they also contain other lattice defects. Therefore, consolidated nanoparticles with retained nanostructure is expected to exhibit a density lower than the theoretical density of the bulk counterpart. There are numerous conflicting views on the sintering behavior of the nanoparticles. Nanoparticles show depressed onset of sintering temperature to the range of 0.2Tm-0.3Tm compared to that of conventional powders that normally exhibit a range of 0.5Tm-0.8Tm, where Tm is the melting point in K. Such results possibly attributed to the structural instability of these particles due to the presence of high surface area. Synthesis of nanoparticles of ceramic, metallic and their mixture has made a substantial progress in the last decade, however, consolidation of such nanoparticles into fully densified bulk components with retained nanostructures remains a difficult problem. A brief outline of the various consolidation processes is presented in Figure 1.

1.2. Plasma Spray: Background and Motivation

Plasma is basically a fourth state of matter with a medley of ionized species, atoms, molecules, photons, electrons. The plasma that is of interest to materials processing is the one generated by inert gases such as Argon, Helium, Nitrogen, Hydrogen either alone or in combination. The amount of heat input to the particles being sprayed through the flame is based on the combination of gases being used. Selection of monatomic gases or diatomic gases depends on the power of the gun being used.

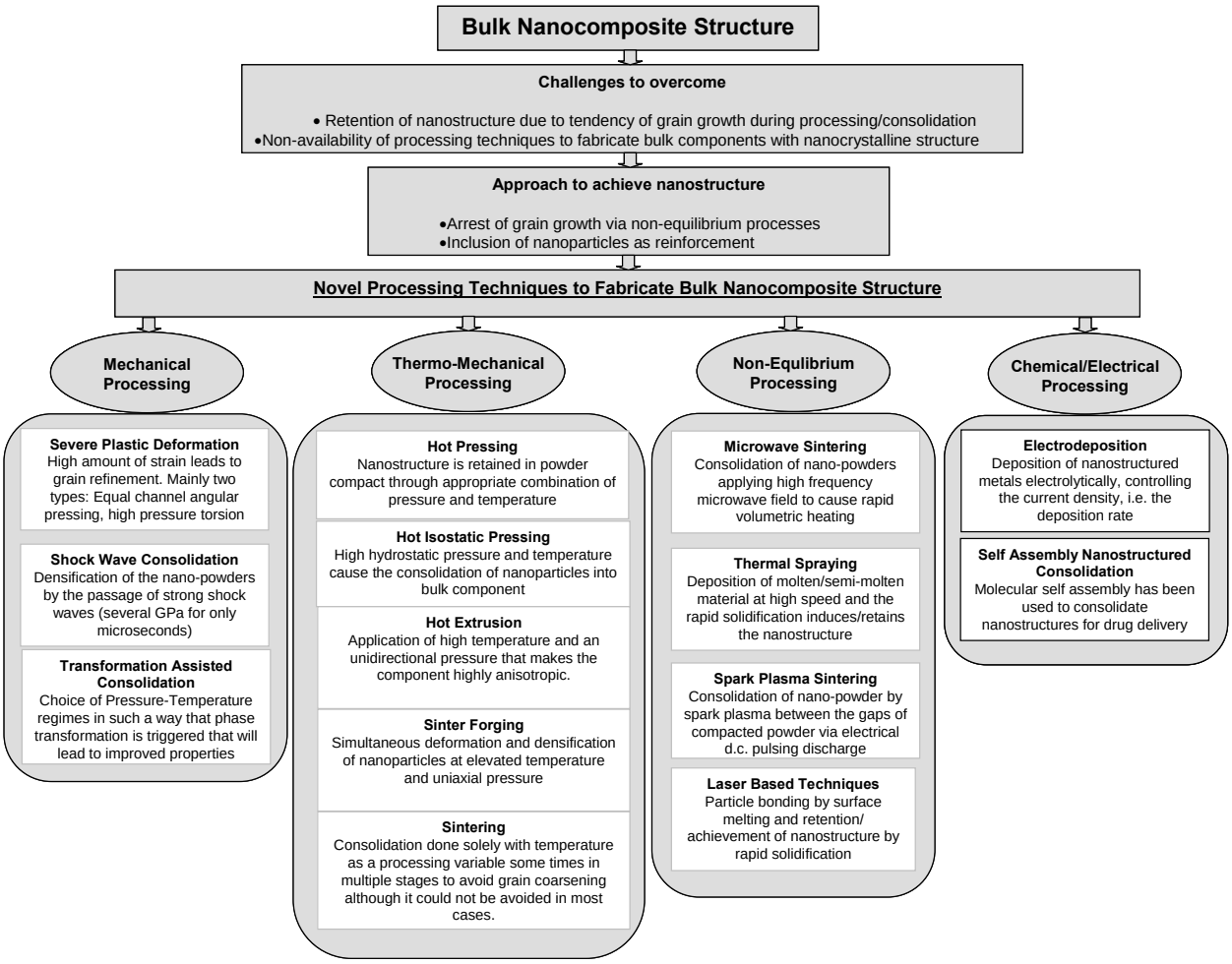

Figure 1 Overview of different consolidation techniques

Nitrogen molecules need more energy to first get dissociated in to atoms and then ionize as against a Argon atom which is readily available in atomic form. As shown in Figure 2, it is evident that Argon is widely being used as a primary gas for the fact that Argon gets ready for ionization the moment it enters the gun chamber where as Nitrogen or Hydrogen has being diatomic in nature has to be dissociated first before ionization starts.

$Ar \rightarrow Ar^{+} + e^{-}$	15000 K
$Ar^{+} \rightarrow Ar^{++} + e^{-}$	15000 K
$N_2 \rightarrow N + N$	7500 K
$N \rightarrow N^{+} + e^{-}$	15000 K
$N+ \rightarrow N^{++} + e^{-}$	>25000 K
$He \rightarrow He^{+} + e^{-}$	25000 K
$H_2 \rightarrow 2\,H$	4000 K

Figure 2 Gas dissociation mechanisms along with the temperature at which the process is complete[23].

The nucleus of Low Z elements have more control over the electrons orbiting around compared to high Z elements. The denouement is that Hydrogen has higher enthalpy compared to Argon. When a mixture of Argon and Hydrogen flows, Argon ionizes first and the heat emitted helps in dissociating Hydrogen and subsequently its ionization. Based on the pressures on which the plasma exists, the enthalpy values vary.

It is quite natural that, during the time the particle enters the flame during which ionization has not even started, the particle may not be melted at all when it comes out of the flame. On the other hand too much of the heat in the flame is detrimental to the particle as it may get over melted and sometimes get evaporated. The Plasma spray processing is a proven technology for development of protective coatings that serve as a thermal barrier for substrates that are in use in land base, aero-based turbines and enhances the life time of the component. The normal spray methodology for depositing TBCs on super alloys involve melting of the particles throughout the

volume from surface to core and then when it splats on to the substrate it undergoes normal solidification on the substrate liquid interface initially and substrate-splat interface at the later stages and predominantly forms columnar grain structure.With an ingenious combination of gases and a good nozzle-electrode combination, a plasma plume will measure a temperature of 20000 K, out of which less than a third of the heat is available for the incoming particles and the rest is spent on providing ionization energy or dissociation energy to the incoming Ar, He or N_2 atoms or molecules. It is to be noted that all of the reactions mentioned in Figure 2 are endothermic and need continuous heat energy to keep the flame up and running. Time of flight, the duration for which the particle stays on the flame is critical from the point of view of properties of the component. Too less a time will result in unmelted particles and lots of porosity in the sprayed component. Gas flow rates and current can be tweaked to retain the particles in the flame for the desired time. Online measurements of velocity using diagnostic equipments come handy in measurements of time of flight indirectly. Shaw et al have mentioned that the critical spray parameter for retention of nanostructures is directly proportional to the power of the spray gun and inversely proportional to the gas flow rate. Gas flow rates can be kept intermediate between that of complete melting and no melting to just have the surface melting and not having the core getting melted. From the point of view solidification, mandrel supercooling by means of external sources such as liquid Nitrogen can eliminate columnar grain growth and induce equi-axed ultra fine grain (nanometer dimensions). A flow diagram summarizing the process parameters to get to nanostructure retention is given below. (Figure 3).

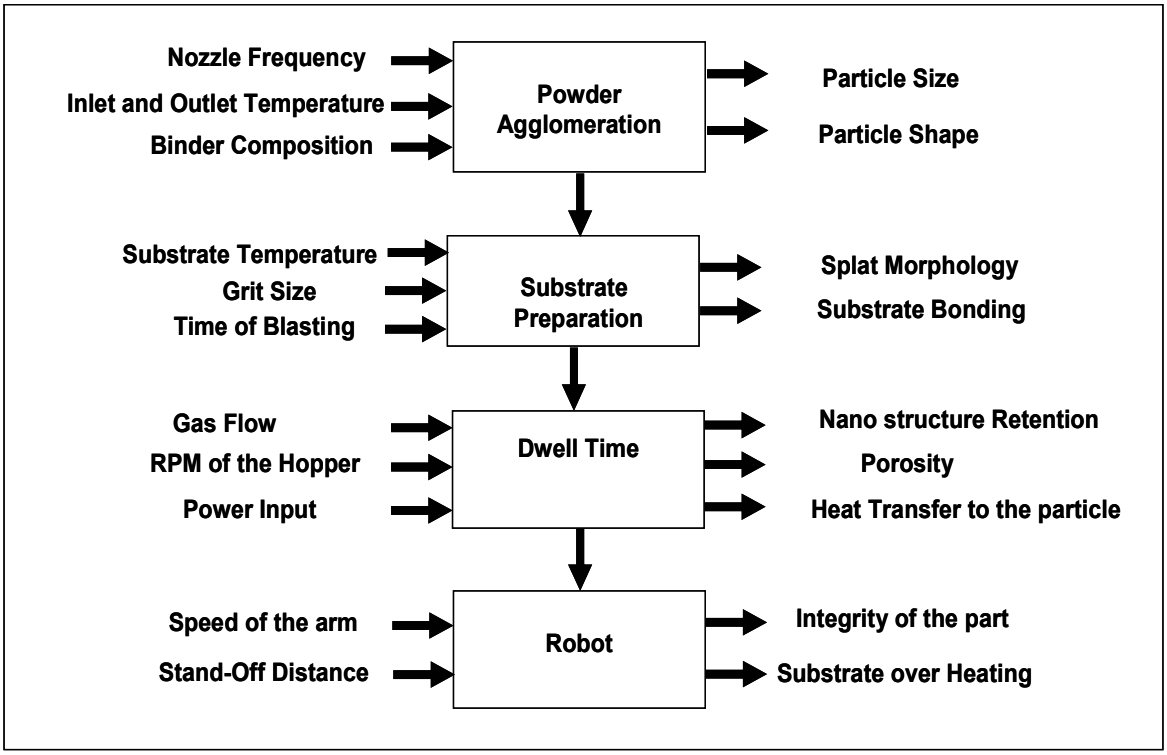

Figure 3 Flow diagram revealing the process intricacies that are involved in retaining the nanostructures.

1.3 Organization

The research has been focused on identifying the important process parameters that will yield a nanostructured coating or a bulk nanocomposite free form component. Alumina and Ceria both high temperature material systems that are coated from powder feedstock and solution feedstock respectively. The powder feedstock of nano alumina has been agglomerated using spray drying process to facilitate the coating process while ceria coating is deposited directly as a coating from cerium nitrate solution precursor. The objective is to develop nanostructured coatings with a given set of parameters selected through with analytical heat transfer calculations Bulk nanocomposites of Tungsten, Alumina and $MoSi_2$ matrices have been fabricated using plasma

spray processing and mechanical properties improvements associated with these nanocomposites have been highlighted.

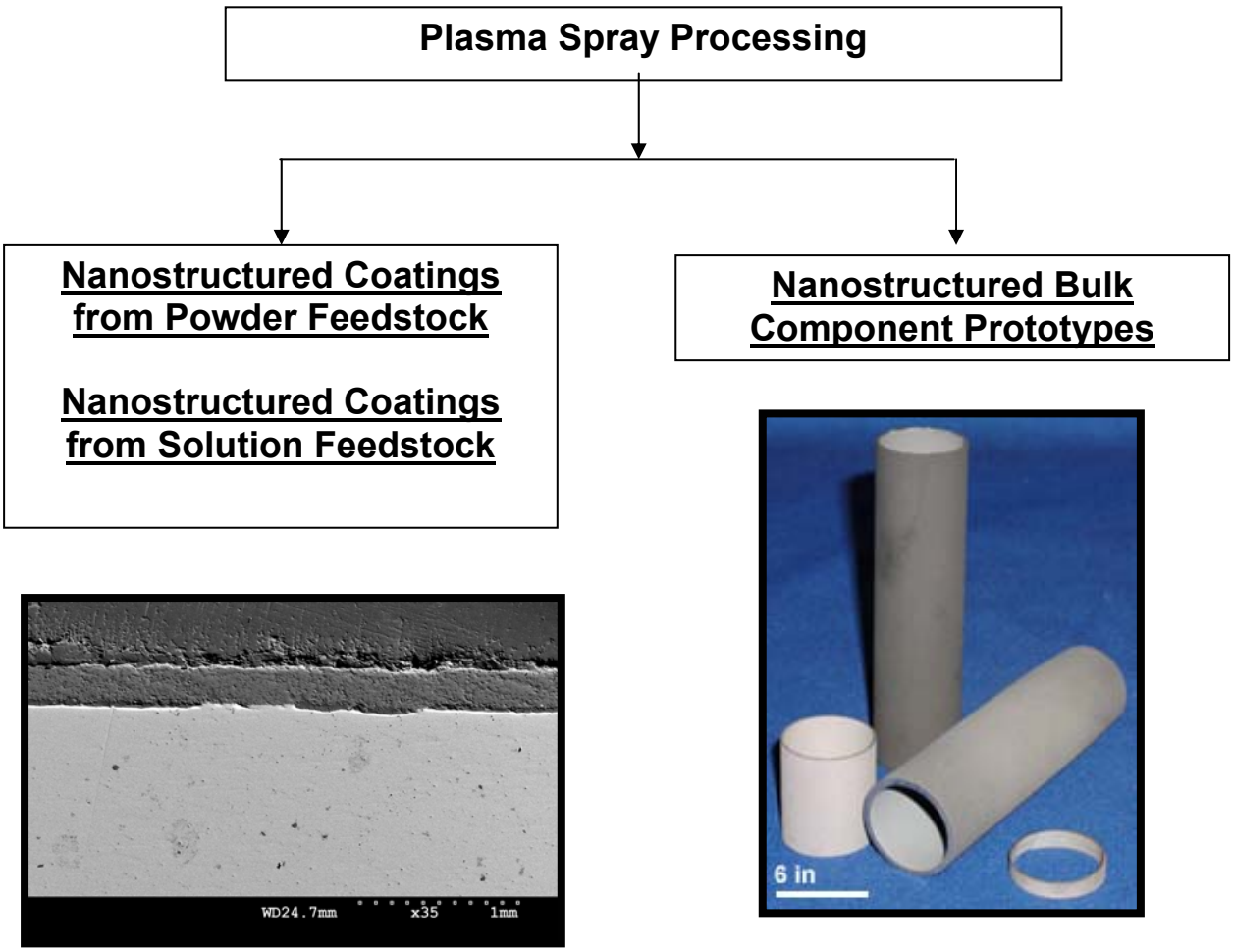

Figure 4 Plasma Spray Processing utilized for development of Coatings or bulk components

CHAPTER 2 INTRICACIES IN PLASMA PROCESSING OF NANO MATERIALS

2.1 Introduction

Nanostructured ceramic particles are difficult to handle through the plasma spray torch and are hazardous to the personnel handling them. The size and density of the powder is of primary importance due to its effect on deposition, solidification, and retention of the properties associated with nanostructures. Some of the process alternatives to spray drying[11] are formation of chemical precursors that forms nanoparticles insitu[12] or using a suspension and feeding in to the flame[13]. Each process has its own merits and demerits. Nano powders could be consolidated as a feedstock using several techniques such as blending, sintering/crushing, spray drying etc. It has been reported that[14] thermal barrier coatings developed from spray dried feedstock had longer thermal shock lives than coatings by other processes. It could be due to the less porosity in the coating as a result of using spray dried feedstock. Hence the technique of spray drying has been utilized to prepare the feedstock. Spray drying is a two-stage process whereby a liquid is atomized in the first step and then the droplets or ensuing particles are dried in a hot gas flow to become an agglomerate solid powder in the final step. With the ability to control the mechanical and thermodynamic environment; including temperature, relative mass flow, solution concentration, liquid breakup, and other factors, the atomization and drying of solids is could be controlled to engineer the particle size distribution and its bulk density which are the essential attributes of feedstock to be plasma sprayed. A general trend towards the change of attributes of spray dried powders such as agglomerate size and bulk density as a function of spray drying parameters irrespective of the material composition is revealed in Table 1.

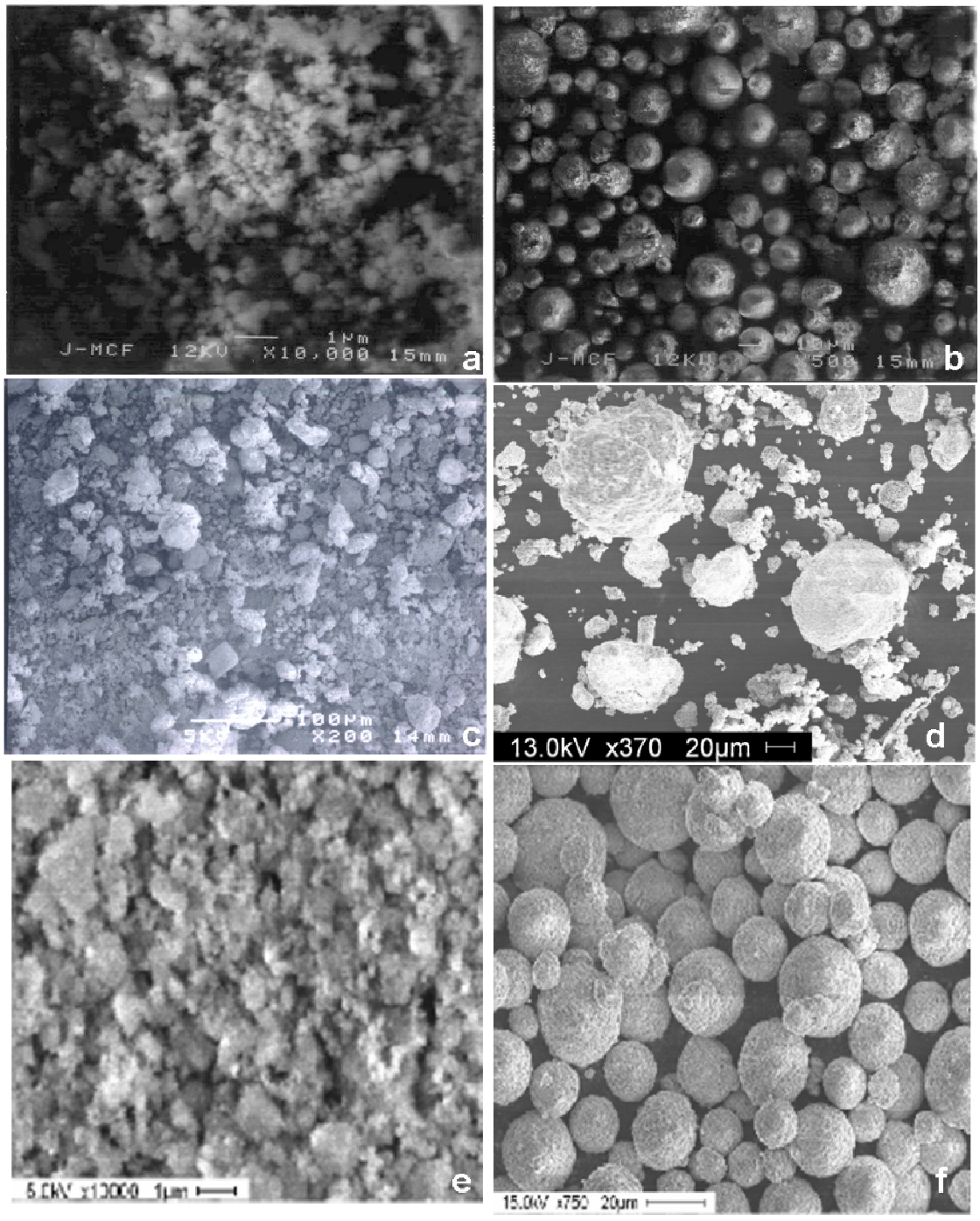

Figure 5 Particle morphology of $MoSi_2$-Si_3N_4 (a and b), W-HfC (c and d) and alumina particles (e and f) before (a, c,and e) and after spray drying (b,d and f).

Figure 5 reveals the particle morphology of different material systems that have been plasma sprayed after agglomeration using spray drying process.

Table 1 Experimental trends in the agglomerate characteristics as a function of spray drying parameters

Parameter	Increase	Bulk Density	Agglomerate Size
Liquid Feed Rate	↑	↓	——
Nozzle Frequency	↑	——	↓
Volume fraction of solid in the feed	↑	↑	↑
Binder Composition	Too much of binder leads to a loosely bound structure		
Spray Drying Temperature	↑	——	↑

2.2 External vs Internal Injection

Unlike micron grain size particles that are typically used for deposition of TBCs, nano grain sized feedstock could not be externally fed in a plasma torch because of deposition efficiency issues. Due to lack of momentum, an increase in Argon flow rates above 50 slm leads to a turbulent flow behavior of the plasma that eventually scatters the particles in all directions leading to a reduction in deposition efficiency. While a low argon flow rate and low stand off distances is quite good for improvement of deposition efficiency, an further improvement of 2-5 % DE could be achieved by choosing internal injection as against external feeding. A series of experiments with constant Argon and Hydrogen flow rates and amperage setting with SG 100

torch could confirm that internal feeding is a wise option to improve the productivity of nano ceramic coatings.

Table 2 Deposition Efficiency of the nano alumina using internal (experiments 1-5) as well as external injection (experiments 6-10)

Experiment	Current (Amp)	Ar (slm)	H_2(slm)	Spray Distance(mm)	Feed rate(g/min)	DE (%)
1	650	60	6	90	15	56.8
2	650	60	6	100	15	53.3
3	650	60	6	110	15	51.6
4	650	60	6	120	15	45.6
5	650	60	6	130	15	40.5
1	650	60	6	90	15	49.8
2	650	60	6	100	15	46.7
3	650	60	6	110	15	43.9
4	650	60	6	120	15	42.4
5	650	60	6	130	15	38.4

CHAPTER 3 ALUMINUM OXIDE

3.1 Introduction

Thermal sprayed coatings of alumina are intended for tribological and thermal barrier applications.[15,16] Paper manufacturing industries typically utilize alumina coatings to protect the rolls from wear. α- alumina is the most preferred phase for thermal barrier applications as the volume expansion and contraction during thermal cycling for this phase is the lowest. Alumina coatings are deposited by both APS and HVOF techniques. Due to low heat energy available with HVOF process, APS process is more popular to deposit alumina coatings. In this study, ,nano alumina has been sprayed as a coating and the challenges faced in terms of preparation of feedstock and selection of spray parameters during coatings have been highlighted.

3.2 Experimental

3.2.1 Powder Feedstock

The nanosized γ-Al_2O_3 powder (40 nm) was acquired from Sigma-Aldrich Co, St. Louis, MO. The pre-agglomerate powder morphology was investigated using a Scanning Electron Microscope (SEM) (Figure 6a). The physical properties of the feedstock chosen are listed below in Table 3.

Table 3 Physical properties of nanoalumina feedstock

Material	Melting Point	Boiling Point	Density(g/cm^3)	Surface area(m^2/g)	Phase
Alumina	2318 K	3253 K	3.65	70-100	γ

γ-Al_2O_3 powder feedstock with high surface area of 70-100 m^2/g has been chosen so that binders used in spray drying could be effectively attached to the surface of the particles which will enhance the agglomeration. The as-received nano powders are irregular and non-spherical. The high surface area particles can easily get adhered to the powder hose, gun interiors during plasma spray which will lead to process delay and material wastage due to choking. Hence spray drying process is essential which could alter the morphology and bind the particles through Van der Waals forces[17].

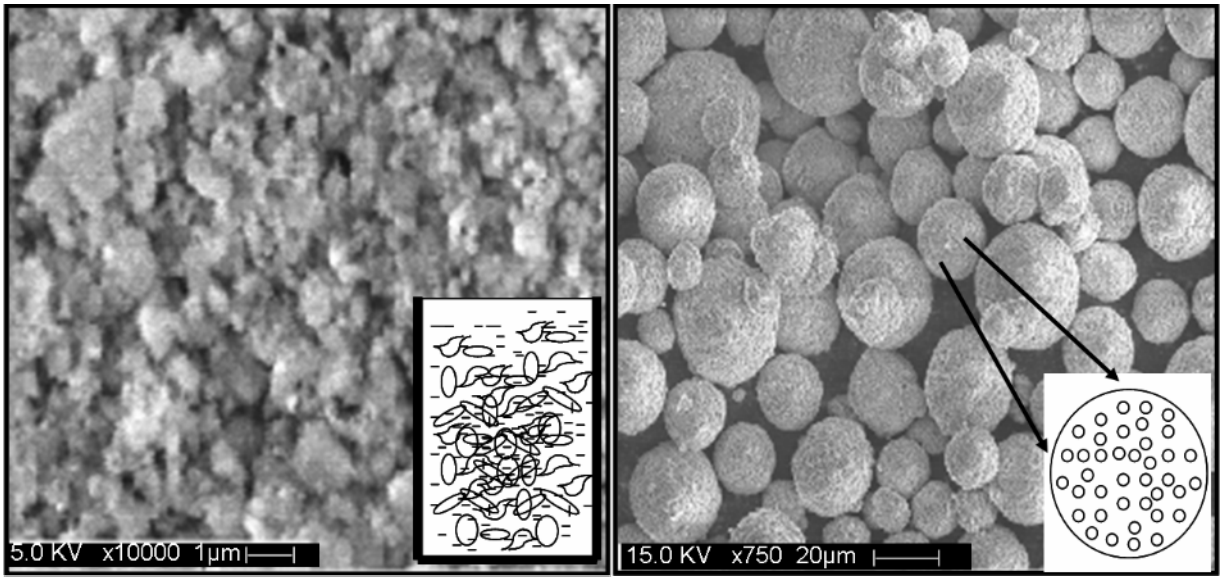

Figure 6 SEM morphology of alumina (a) before and (b) after spray drying. (Inset (a) showing a schematic of alumina nano particles in suspension. Inset (b) showing how nano particles are loosely bound together in each of the spherical agglomerates.

3.2.2 Spray Drying

The agglomeration of nano-Al_2O_3 was carried out in a Büchi B-290 (Büchi Corp. Newcastle, DE) research model spray dryer. A suspension of the nanoparticles was prepared using 300 ml of de-ionized H_2O, 7 g of Polyethylene glycol (PEG) and 70 g of nano- Al_2O_3 (Figure 6a Inset).

This composition works well for better flowability in nanoagglomerates. The polymeric binder, PEG, in solution uses Van der Waals forces to bind the nanoparticles together and forms spherical droplets during atomization. The nano-alumina slurry was attained via vigorous magnetic stirring for 30 minutes and heating to 363 K (90 ºC). The pre-heating of the solution assists in the slurry formation and lowering the enthalpy needed during the drying process for moisture removal. The final product is a feedstock of 20-30 μm spherical agglomerates of 30-40 nm nanoparticles (Figure 6b Inset).

3.2.3 Atmospheric Plasma Spray

APS process is used for coatings and near net shape structure of ceramic matrix nanocomposites[18-19]. In this process, the agglomerated powder is fed through a plasma gun to a high temperature (10,000–15,000 K) plasma arc produced between the nozzle and the electrode. A Praxair SG 100 DC plasma (Model SG 100 Praxair TAFA, Concord, NH) torch with standard hardware mounted on ABB 6 axis robot (ABB Inc., Detroit, MI) was used for spraying. The robot has been programmed to carry the torch both to the spray diagnostics (section 2.4) and the substrate location. Argon and hydrogen gases were used as primary and secondary gases, respectively. A representative set of four processing parameters have been chosen for the APS as listed in Table 4. The standoff distance used for all these spray conditions was 100 mm. Spray dried nanoalumina feedstock is coated on mild steel coupons for SEM and TEM characterization. The substrates were air cooled using part coolers.

Table 4 Spray Parameters used for spraying Nanoalumina agglomerates

Spray Condition	Current Amps	Voltage, V	Primary Gas Argon, slm	Secondary Gas, Hydrogen, slm	Carrier Gas, slm
I	500	55	33	2.3	2.8
II	600	60	35	4.7	3.7
III	700	45	38	4.7	4.7
IV	700	45	38	4.7	6.1

3.2.4 Particle State Diagnostics

Since the state of the impinging alumina droplet is crucial to the characteristics of the coating, monitoring the particle states on its way to the substrate is important. Theoretically, coating microstructure depends on the molten state of the particle. For all practical purposes, the particle temperature is regarded as an indicator of the molten state. Amount of flattening of particles on to the substrate depends on velocity of the particles. Thus monitoring these two particle states can be a good practice to decide on what type of microstructures to achieve in the end coating. Accuraspray diagnostic equipment (Tecnar Automation Inc., Montral, Quebec, CA) is used to monitor the particle velocity (V) and temperature (T). The measurement principle and instrument details are available elsewhere[20]. The method of measurement is shown in Figure 7. Torch parameters were stabilized before the measurements were made.

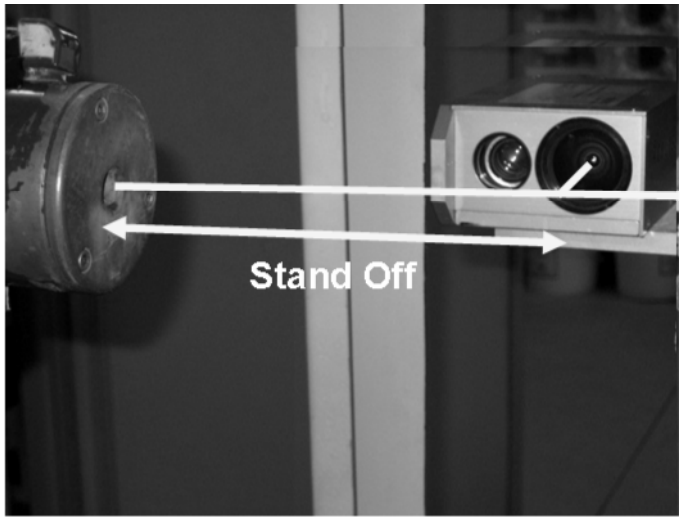

Front View of the torch-camera alignment

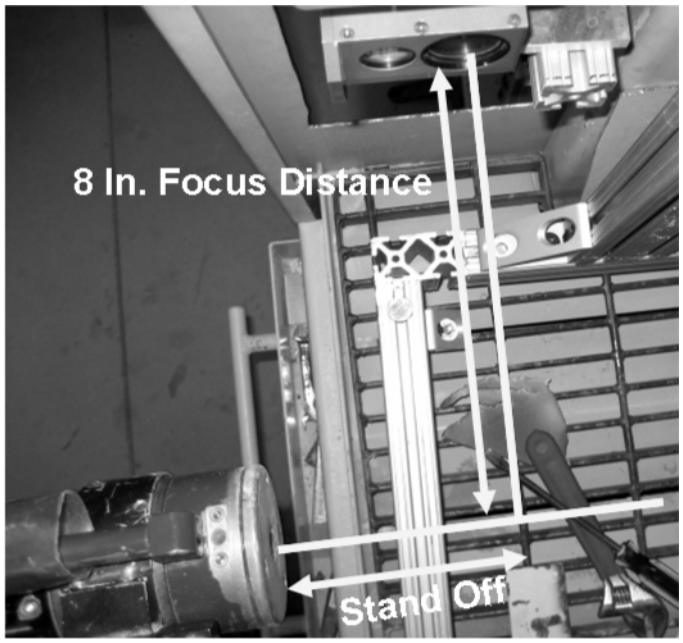

Top View of the torch-camera alignment

Figure 7 Front and top view of the torch-camera alignment used for measurement of particle temperature and velocity during plasma spray of nano alumina.

3.2.5 Characterization

Scanning Electron Microscopy: The morphology and the size of the feedstock before and after spray drying was studied using scanning electron microscope (SEM; Model JEOL 6400F, JEOL, Tokyo, Japan) with 5-15 KV operating voltage.

Brunauer–Emmett–Teller (BET) Analysis[21]: The BET equipment (Porous Materials Inc., Ithaca, NY) was used to measure the pore volume and particle size of the agglomerated feedstock (model BET 201-A; Porous Materials Inc.). A few milligrams of agglomerated alumina were taken in a quartz 'U'-tube for the measurement. The sample was outgassed at 2000C in vacuum for 30 min. Ultra-high purity nitrogen gas was used as adsorbate at the liquid nitrogen temperature. The adsorption of nitrogen gas on the sample in the 'U'-tube was measured for different pressures (P) at the testing temperature of −195.76 ^{0}C. A standard reference sample, a silica–alumina powder with a surface area of 258 ± 5.29 m^2 g^{-1}, was used before the measurement to ensure the reproducibility of the BET spectrometer.

Focused Ion Beam and Electron Microscopy: To study the retention of nanostructure and the impact of splats to form a dense coating, Transmission electron microscopy (TEM) and Scanning electron microscopy (SEM) have been respectively employed. TEM is performed using a field emission transmission electron microscope (Model Tecnai F30, FEI company, Hillsboro, OR) at an acceleration voltage of 300 keV. A Focused Ion Beam (Model FEI 200, FEI Company, Hillsboro, OR) equipped with a 25–50 kV gallium liquid metal ion source (LMIS) has been employed for TEM sample preparation. Figure 8

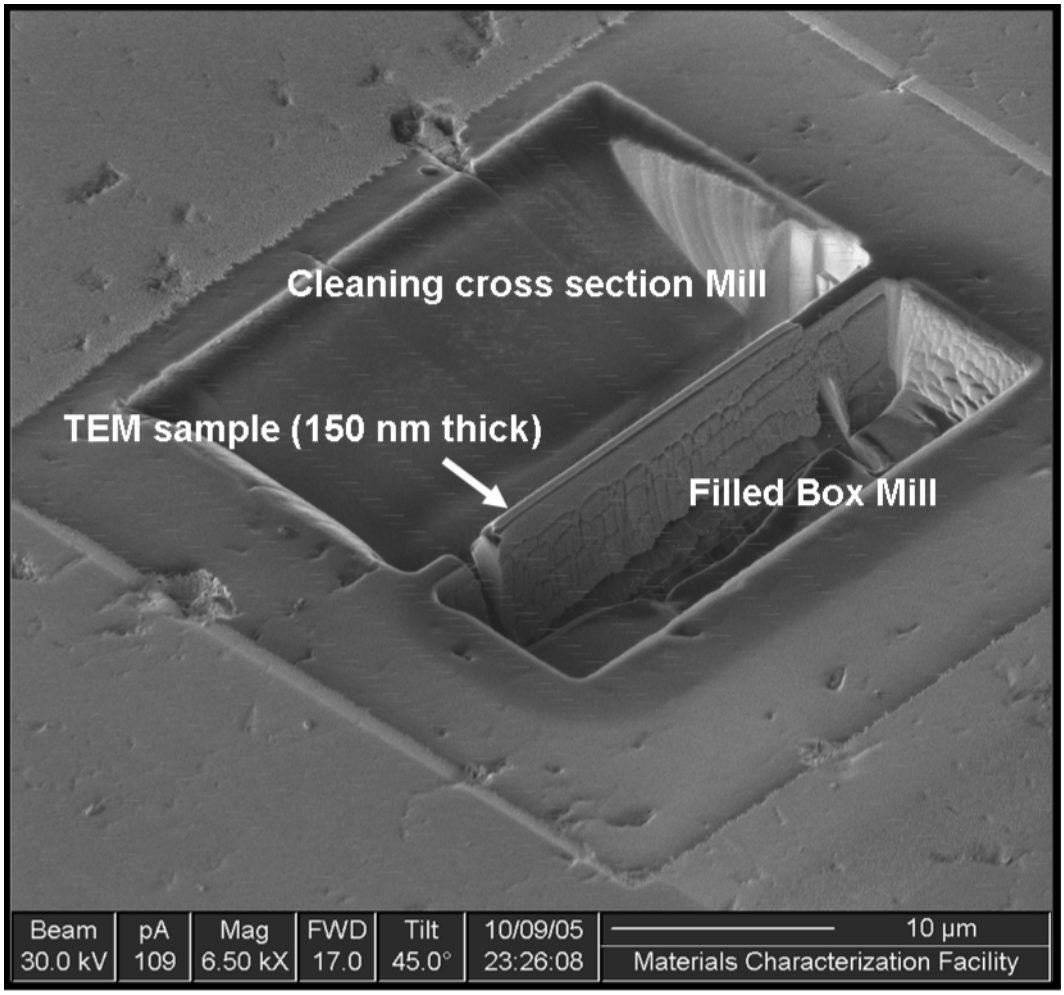

Figure 8 Focused Ion Beam equipment being used to create a TEM sample from the coated sample. The sample is thinned to ~150 nm to enable the nanostructures to be clearly imaged.

X-Ray Diffraction: The phase transformation of the alumina deposit after plasma spraying was studied using a XRD equipment (Rigaku Inc., TX) with Cu Kα radiation operating at 30 kV and 30 mA.

3.3 Results and Discussion

3.3.1 Mositure removal through spray drying

In a co-current spray where the hot air and the spray are following the same direction, the moisture removal can be optimized by controlling the aspirator rate. Before any spray droplet gets completely devoid of moisture, there is a vapor pressure gradient between the droplet and the surrounding air. Moisture tries to flow from the high vapor pressure (core of the droplet) region to the surrounding air (Inset bottom left Figure 9) In this process, optimum aspirator rate should be maintained inside the spray drier chamber. The vapor pressure difference between the wet agglomerate (P_{wa}) and the air (P_{air}) could be related to the temperature difference ΔT between the surface and air as follows[22]:

$$Pwa = Pair + \frac{29}{18}\frac{C_P P_T}{\lambda}\Delta T \quad \text{(1)}$$

where, C_p is the specific heat of vapor at constant pressure, λ is the latent heat of evaporation,. Figure 9 is a plot of pressure difference ($P_{wa} - P_{air}$) and temperature difference (ΔT) for alumina particles. With a large difference in vapor pressure between the wet agglomerate and the surrounding air, the droplet is still wet and there is an appreciable temperature difference between the surrounding air and the droplet (State A in Figure 9). It could be seen that more moisture gets entrapped if sufficient aspirator rate (the rate at which the air flow rate is maintained inside the chamber that will eventually dictate the residence time of the agglomerates in the spray drying chamber) is not maintained. Trapped moisture leads to donut shaped particles that will not flow properly during the plasma spray. It has been determined through experiments

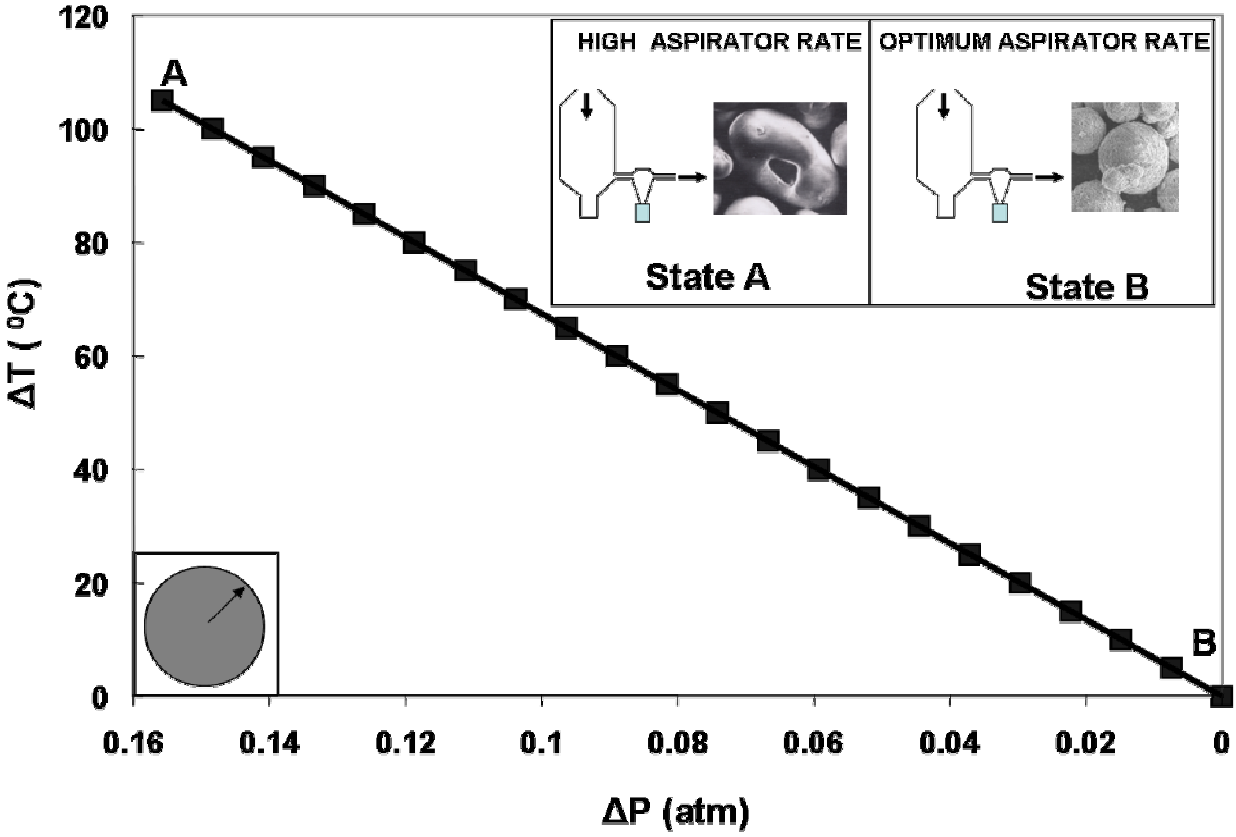

Figure 9 The effect of aspirator rate on the agglomerate moisture content. High aspirator rate leading to particles losing the integrity (state A) as against an optimum aspirator rate that will yield moisture free agglomerates (State B).

that an aspirator rate of 65 % is perfect for the alumina particles to get rid of all its moisture (State B) on its way to the collection chamber. (Residual Moisture could be visually seen and there is no direct measurement of the moisture of the particles. If there is considerable amount of moisture, the particles will stick to the container and the flow will be poor which is an indicator.)

3.3.2 Attributes of spray drying

Inlet temperature of the drying medium, retained porosity and agglomerate size are some of the attributes that are to be controlled in order to accomplish the spray process more efficiently. All three attributes as a function of inlet temperature of the air is plotted as a histogram in Figure 10.

The amount of moisture retained depends upon the ratio of the enthalpy (kcal/kg) of the feed entering the spray drying chamber to the enthalpy of the feed exiting the chamber. Lower the enthalpy ratio, the higher is the heat utilization in the spray drying. For non-adiabatic chamber walls, measurement of the enthalpy ratio is important for optimization and effective utilization of the spray drying resources (Figure 10a). It has been found that four inlet temperatures (see Figure 10) were found to have optimum enthalpy ratios well within the expected range. If the agglomerate has fewer pores, it will increase the momentum of the agglomerates when passing through the plasma torch. Therefore, it is quite important to quantify the pore volume. From Figure 10 (b), the pore volume was the lowest (0.02 cc/g – through BET) among all the four at 130^0C. During plasma spraying low pore volume is favored because the heat transfer to the core of the particle could be faster than by convection in presence of the pores. At 130^0C, there is a low shrinkage during cooling (leading to low pore volume) compared to that of other inlet temperatures. However, pores could not be totally eliminated during the spray drying process. The size of the agglomerate is a function of spray nozzle vibration frequency as well as the inlet temperature of the drying medium. In order to achieve a mean agglomerate size of 25 μm, an inlet temperature of 130^0C is used (Figure 10c). Higher inlet temperatures leads to low agglomerate size particles (~20μm) due to increased shrinkage

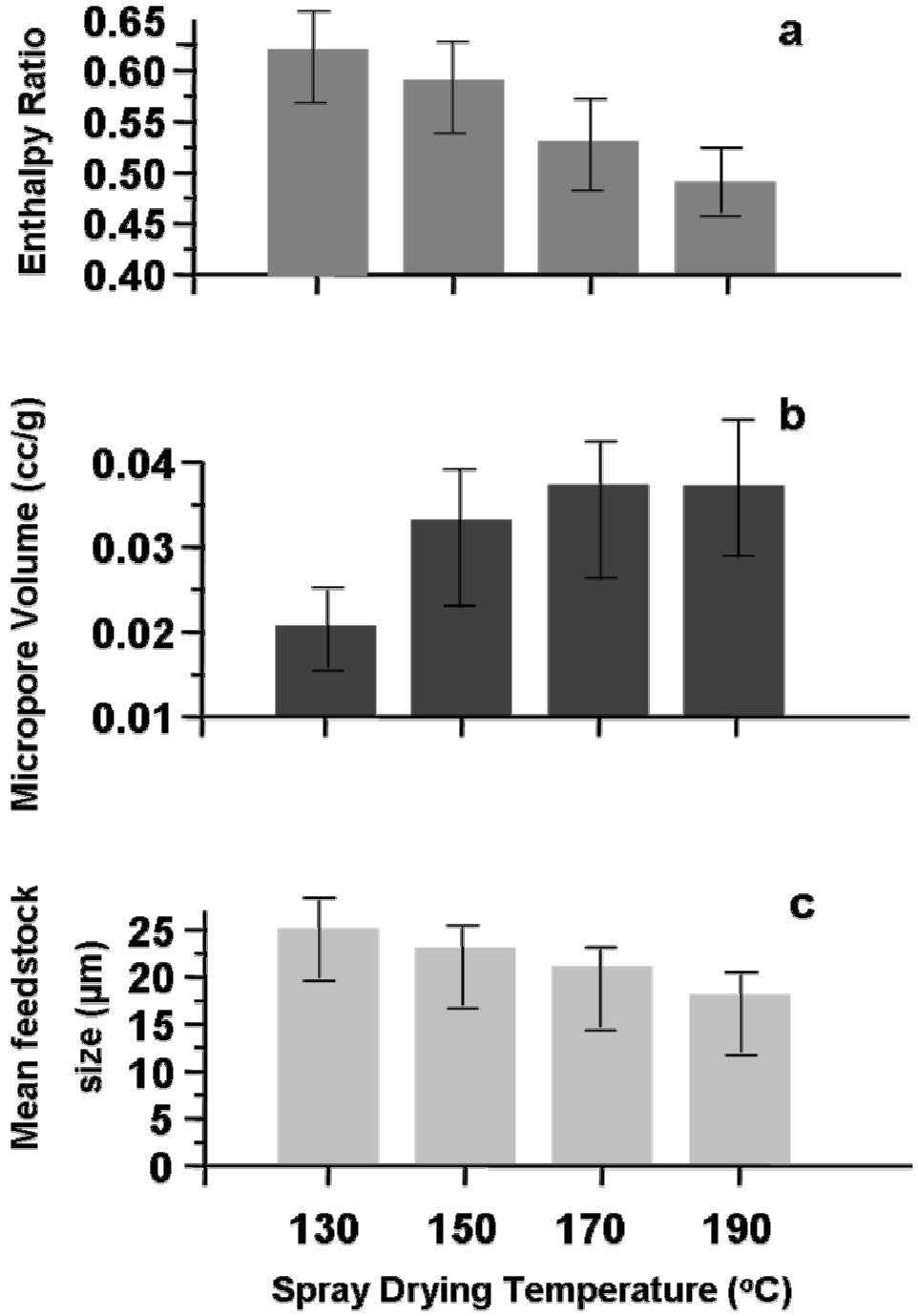

Figure 10 Effect of enthalpy ratio (a), pore volume (b) and agglomerate size (c) on the spray drying temperature.

3.3.3 Heat transfer during Plasma Spray

Selection of gases for generation of plasma is an important step in the processing of nanostructured coatings. Nitrogen molecules need more energy for dissociation in to atoms and then ionize as against an argon atom which is readily available in atomic form. Hydrogen has higher enthalpy compared to argon. When a mixture of argon and hydrogen flows, argon ionizes first and the heat emitted helps in dissociating hydrogen and subsequently its ionization. Using the analytical heat transfer calculations, the plasma that is of interest to nano alumina coating is chosen from inert gases such as Argon, Helium, Nitrogen, Hydrogen either alone or in combination. The momentum (p) of the particle after its injection in to the plasma plume changes according to the drag force (F_d) exerted by the plasma[23-24].

$$\frac{dp}{dt} = F_d \quad \text{-----} \quad (2)$$

Since the agglomerates are perfect spheres, drag force could be quantified based on their relationship between the diameter of the particle (d_p), velocity of the particle (v_p) and viscosity of the plasma gas (υ_g).

$$F_d = 3\ \Pi\ d_p\ v_p\ \upsilon_g \text{ -------} \quad (3)$$

Combining equation 2 and 3 and further integration lead to a relationship of distance versus time that could be used to calculate the residence time for the ceramic particles with different gas mixtures (Figure 11).

$$\frac{Vt}{Vo} = \exp\left(\frac{-18\nu_g t}{\rho_p d_p^{\ 2}}\right) \text{--------} (4)$$

The diameter of the agglomerates from experiments was measured as 25 μm and so this value has been used for the calculations. (SEM picture (Figure 6b))

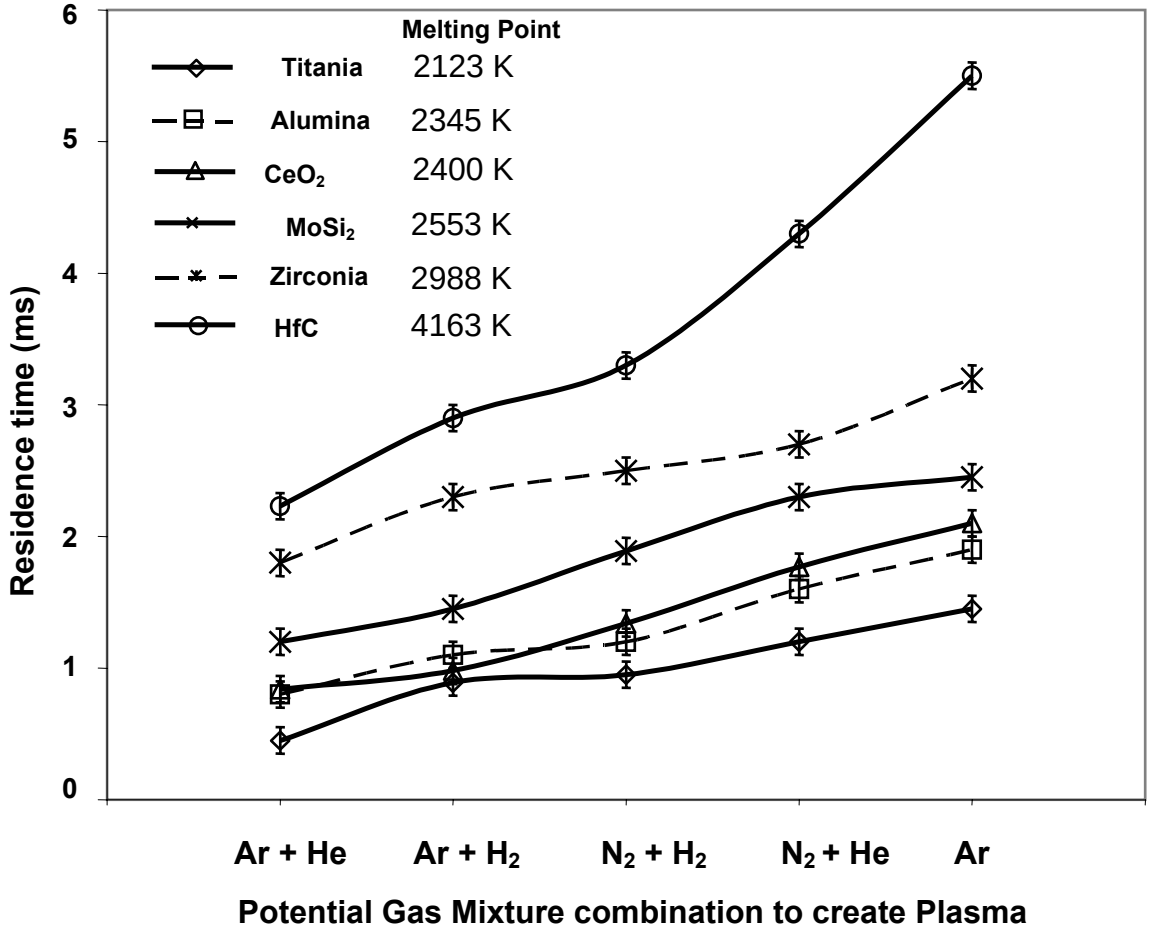

Figure 11 Residence time required for different materials for the heat to be transferred to the core of the agglomerate as a function of different gas mixtures. $Ar+H_2$ mixture has been determined to be more suitable and economical for this purpose.

3.3.4 Fraction of melted particle

The velocity range within which the agglomerates become fully molten have been determined using heat transfer calculations and also correlated with the microstructures. The ratio of the portion of the melted zone in the particle (r) to the radius of the particle (R) is calculated as a function of the velocity of the particles in flight. In this calculation, the particle has been

assumed to have both conductive and convective heat transfer as there are small pores in between the bound nanoparticles. Such pores have air entrapped in them and heat is supposed to transfer through convection (Figure 12 (bottom inset)). The rate of change of fraction of particle molten, x_c (= r/R) is calculated using Eq. 5 [25]

$$\frac{dx_c}{dt} = \frac{(Q_{cd} + Q_{cv})}{mL_m} \quad \text{------} \quad (5)$$

where L_m is Latent heat of fusion of the particle J/kg, m is the mass of the particle, kg, Q_{cd} is the heat transfer rate due to the conduction and Q_{cv} is the heat transfer due to the convection. Q is calculated from the heat transfer equation,

$$Q = a_p [h.(T_f - T_p) - \varepsilon.\sigma.(T_p^4 - T_a^4)] \text{ -------- } (6)$$

where a_p is the surface area of the particle, T_p is the temperature of the particle, T_a is the temperature of the surroundings, T_f is the temperature of the plasma plume, σ is the Stefan Boltzmann constant and ε is the emissivity of the particle and h is the heat transfer coefficient of the particle . Heat losses due to radiation have been calculated assuming the alumina particle as a black body and follow the Stefan-Boltzmann law

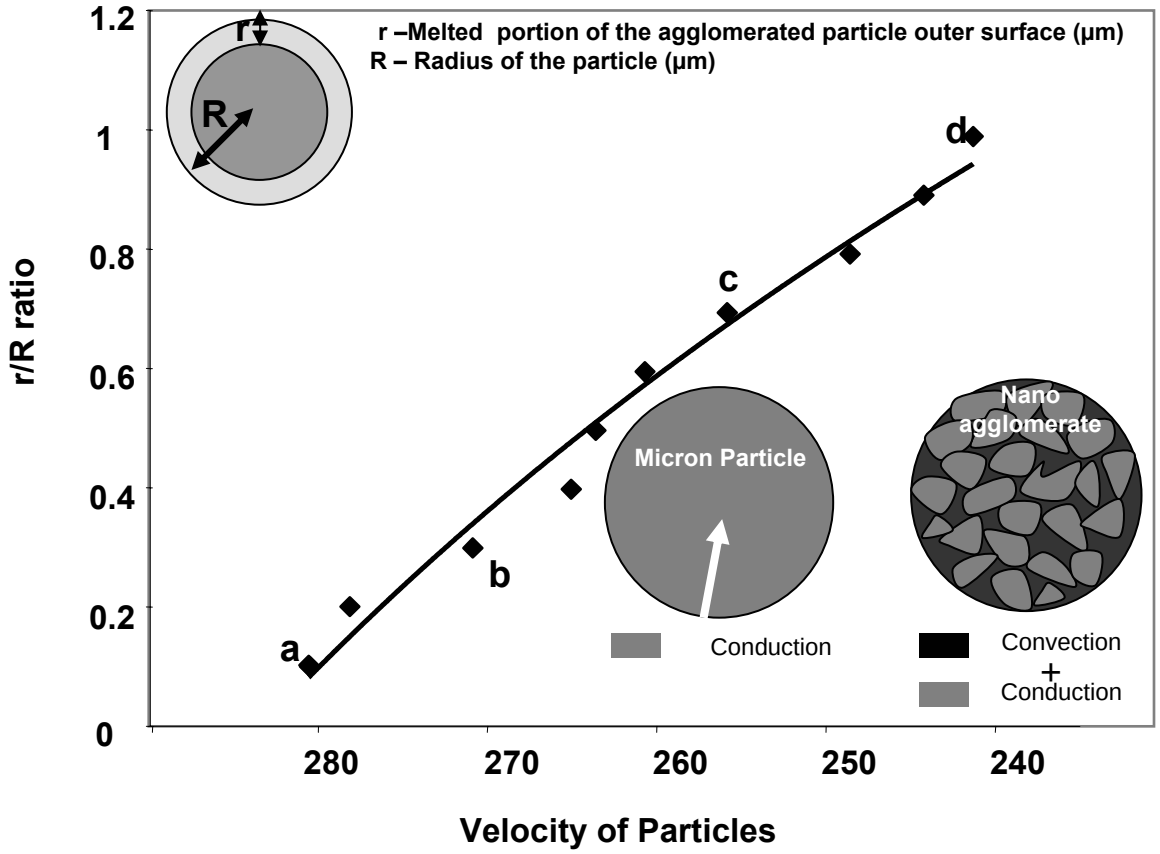

Figure 12 Heating transfer calculation involving fraction of particle getting melted as a function of their velocity during the spray process. An optimum velocity of 240 m/s is required for the heat to fully transfer to the core.

. Equation 6 is a quintessential outcome of the heat transferred to the particle as a result of both conduction and convection. From (5) and (6), the fraction of particle molten as a function of velocity of the particle is plotted as shown in Figure 12. It could be seen that 240 m/s velocity is required so that the heat can penetrate to the core of the agglomerates. Points a, b, c and d are locations corresponding to 10 %, 30 %, 75 % and 100 % melting at velocities 280, 270, 255 and 240 m/s respectively. This plot is valid for Ar + H_2 since Argon-Hydrogen mixture is economical and can melt the agglomerates in a relatively less time compared to other mixtures (Figure 11)

3.3.5. Experimental correlation of fraction particle melt

In order to confirm the portion of the particle melted from the surface, nano alumina agglomerates have been internally fed through the SG100 plasma torch with Ar- H_2 plasma at the velocities of 280, 270, 255 and 240 m/s. The velocities are monitored using accuraspray^{TM} diagnostic camera till there is a substantial stability in the particle velocity. Carrier gas flows are controlled accordingly to achieve the respective velocities. The particles sprayed are collected and subjected to SEM analysis. The microstructures of individual particles sprayed at these velocities are depicted in Figure 13. In Figure 13 a, b, c and d correspond to points a, b, c and d in Figure 12. It could be seen that there is a correlation between the fraction of melted particle (Figure 13) to the calculated values (Figure 12). Gun hardware quality, industrial gas purity also has an influence in these values which is not taken in consideration during calculations. These calculations are important to confine the process parameters in a narrow window for desired microstructures with less iteration. A 100 mm standoff distance is maintained throughout the experiments. In order for nano alumina nano agglomerates to be melted completely, a maximum velocity of 240 m/s is allowed, beyond which only partial melting will occur (Figure 13b, c). The velocities lesser than the threshold velocity of 240 m/s yields fully molten particles but the impact of these particles on to the substrate decreases which yields low density coatings. Therefore, optimum velocity for achieving highly dense coatings (95%) is 240 m/s.

3.3.6 Phase determination of nano alumina coatings

X-ray diffraction analysis of the as-received nano γ-Al2O3 particles, the agglomerated spray dried powder and the coating is shown in Figure 14. As indicated in the spectra, the

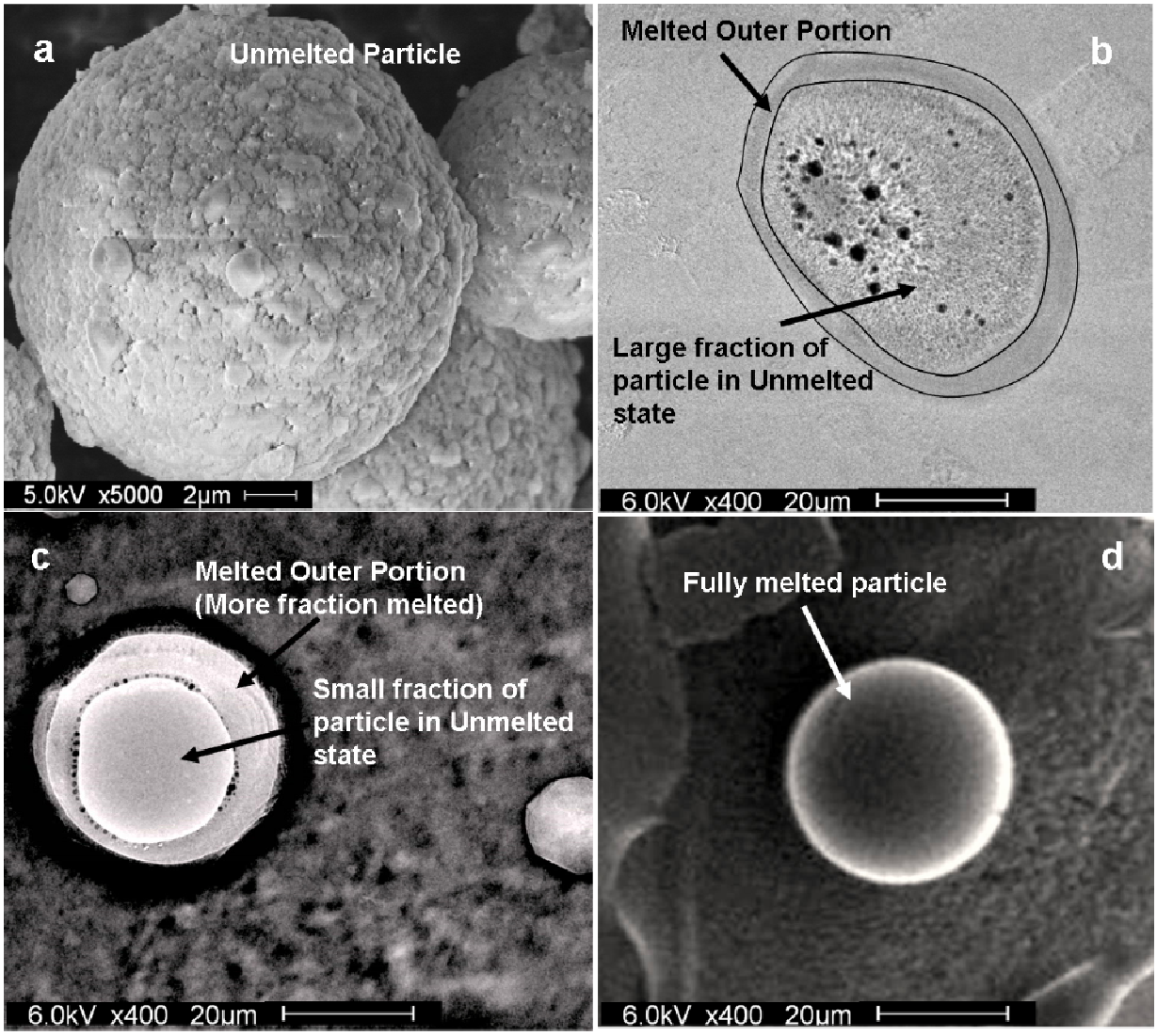

Figure 13 Scanning Electron Microscopy revealing the fraction of melted portion of particle at points a, b, c, d corresponding to Fig. 12

major phases present in the nano-alumina and the agglomerate prior to plasma spraying are stable phase α-alumina (trigonal), the metastable polymorph γ-alumina (cubic), and most likely the metastable polymorph δ-alumina (tetragonal or orthorhombic).Aluminum oxide has many metastable polymorphs including the polymorphs mentioned above[26]. The phase determination

during and after the plasma spraying of alumina is important because the grain growth behavior is related strongly to this phase transformation[27]. Although it is very difficult to determine the

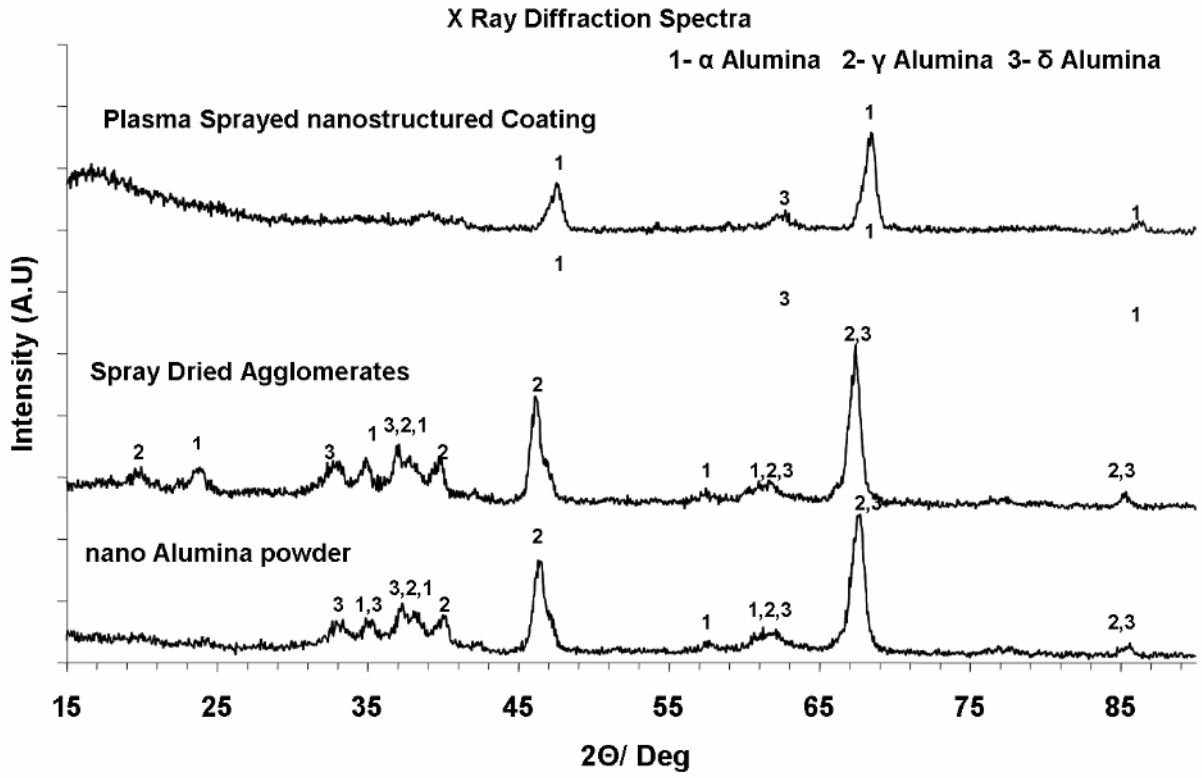

Figure 14 X-Ray diffractogram revealing the presence of high temperature phase α-alumina confirming the rapid solidification of nano alumina during deposition on to the substrate.

exact transformation sequence from the polymorphs to the stable cubic structure, the remaining presence of the stable α phase (high temperature phase) after plasma spraying is quite apparent in this study and similar to findings in previous literature[28]. Rapid solidification prevented the transformation of the high temperature α phase to γ phase during the formation of coating on the substrate. The density of the stable α-alumina trigonal structure is 3.99 g/cm^3; whereas the density of the polymorphs, both γ and δ, are 3.6-3.65 g/cm^3. Therefore, presence of unit cells

with high packing factors lead to less defect in the structure thereby avoiding any adverse diffusion of the species from the substrate that is being protected. Calculations of the surface energies of different orientations of the polymorph γ-alumina introduced by Levin and Brandon[27] would also explain why the surface energies are much lower than that of the stable α-alumina, and further, the high specific surface area observed for the γ-Al_2O_3. Using the following Scherrer relationship[29]:

$$B = \frac{0.9\lambda}{t.Cos\Theta} \quad \text{-------} \quad (7)$$

where, B is the broadening of the diffraction line measured at half its maximum intensity (radians), t is the diameter of the crystallite (or particle), and λ is the wavelength of the Cu Kα radiation, a study of the crystallite (particle) size was performed. The crystallite sizes were 51 nm. The phase determination is quite important in this study because the presence of α-alumina leads to less volume expansion due to temperature fluctuation thereby preventing spallation due to thermal fatigue[30].

3.3.7 Experimental process map for parameter microstructure relationship

Plasma spray is carried out using the parameters listed in Table 4 Spray Parameters used for spraying Nanoalumina agglomerates. These parameters have been chosen in such a way that the maximum velocity is 240 m/s to ensure full melting of the agglomerates. Carrier gas flow rates were different in each of these parameters with spray condition (I) having the lowest carrier gas flow and (IV) having the highest. A standoff of 100 mm is maintained during spraying. Figure 15 summarizes the spray velocity and temperatures achieved with these conditions and the

microstructural variation (SEM) and nanostructures (TEM) for the select conditions II and IV. At a spray velocity of 180 m/s (Condition I), the particles could not gain enough momentum and are scattered with a low yield. With spray condition II, the particles could be injected on to the substrate at a velocity of 200 m/s. TEM microstructures revealed the retention of nanostructures with the particle size of 40 – 50 nm (Figure 15) . SEM pictures revealed a relatively porous coating. Spray condition III and IV have the same parameters except that the carrier gas flow is higher in IV. A melting temperature of 2340^{o}C is recorded during the spray with this condition and the velocity is clocked at 240 m/s. Due to the high velocity, the splat formation was better and there is a significant increase in the density of the coating (Figure 15(SEM picture corresponding to parameter IV) . TEM analysis confirmed the retention of the nanostructure (Figure 15) With these given set of parameters (Table II), nanostructures could also be retained as well as the density of the coating could also be manipulated using nano agglomerates.

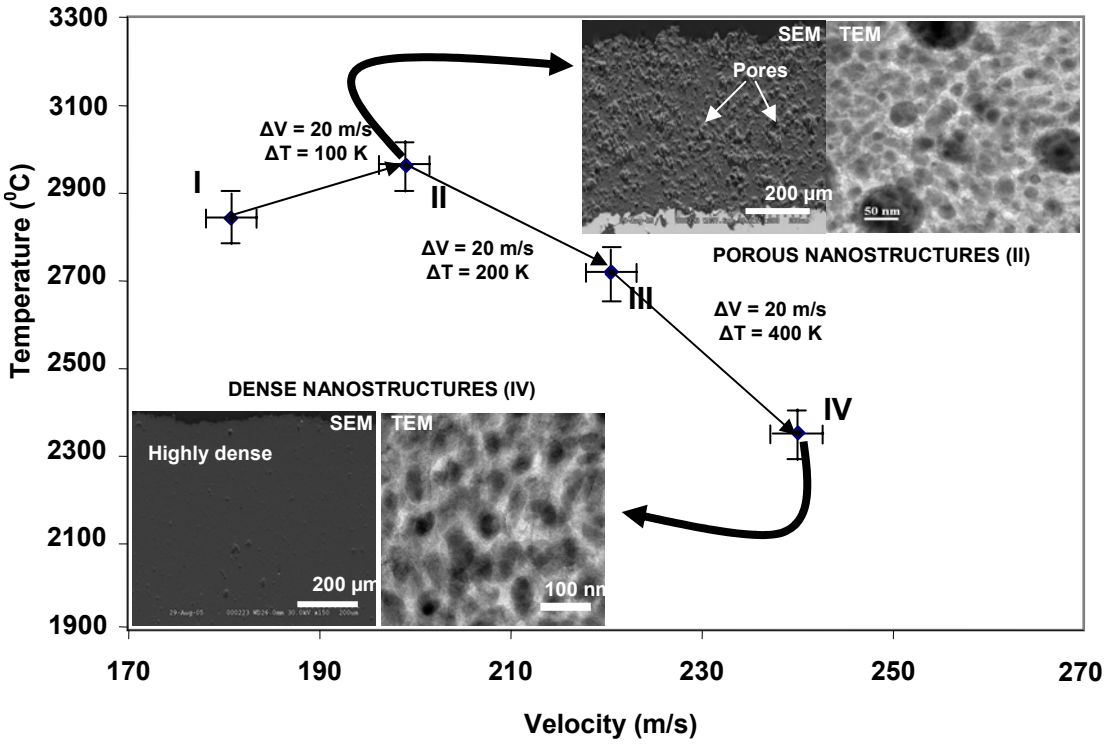

Figure 15 Experimental process map revealing the parameter-microstructure relationship of alumina coating. Shown at the inset are the SEM and TEM pictures for parameters II and IV.

In an effort to determine the density of the coating, the spray has been carried out on a copper substrate, using the plasma system parameters (Parameter II and IV), and removed as a bulk component. The density of these two components was measured using Archimedes Principle. The density of the parts formed using spray condition II and IV was 3.25 g/cm^3 and 3.78 g/cm^3 for which is showing 95% density and is quite a good density for a nanostructured coating.

3.4 Conclusions

In this study, the processing challenges and solutions in plasma spraying of nanoalumina has been reported. Spray drying temperature of 130^{0}C yielded spherical agglomerates and has yielded less micropore volume among the four temperature variants experimented for an easy

flow of nanoparticle in the plasma plume. The gases for creating the plasma in DC plasma torch and the rationale behind choosing the gas mixtures have been demonstrated through analytical heat transfer calculations. The velocity of the particles in the flight plume to achieve complete melting have been calculated and experimentally verified in the resultant APS coatings (240 m/s yields a dense nano structured coating). The density of the coating and its correlation with the particle states (temperature and velocity) are presented. A maximum density of 96-97 % is achieved by using high carrier gas (13 SCFH). Nanostructures (40-50 nm) could be retained using the given set of parameters during APS deposition. This study could be extended to any nano ceramics system intended for photo catalytic, thermal barrier and other high technology applications.

CHAPTER 4 NANOCRYSTALLINE CERIA

4.1 Introduction

Corrosion resistance is considered to be one of the most important material properties for many engineering applications. In general, stainless steel has higher resistance to oxidation in both dry and wet environments[31] due to the formation of a chromium (III) oxide (Cr_2O_3) layer compared to other grades of steel. In the class of steels, martensitic steels are appropriate for applications where the material is subjected to both corrosion and wear. Common applications include surgical instruments, bearings, spindles and hot gas turbine components[32].

Corrosion resistance can be affected by several parameters. In steels, due to sensitization (i.e., a process of formation of chromium carbide along grain boundaries), the amount of chromium available for oxidation resistance is reduced[33]. Such loss of chromium can significantly decrease the corrosion resistance. The resistance to corrosive media of martensitic stainless steels is relatively poor compared to ferritic and austenitic types[32], but as the environment temperature increases, the effective corrosion prevention of the chromium oxide film decreases. Many high-temperature alloys rely on the formation of protective Al_2O_3 and Cr_2O_3 scale on their surface to protect against oxidation[34, 35, 36]. Both cracking and spallation of the oxide scale restricts these alloys as high-temperature-oxidation resistant material.

The corrosion resistance of a stainless steel can be improved through by producing extrinsically or intrinsically a protective coating by either surface modifications or pretreatments. Elements such as Cr and Ni are frequently added to improve their resistance to atmospheric, organic and alkaline environments[37]. Various coating techniques such as, anodization, physical vapor deposition, chemical vapor deposition[38], sol-gel coating[39] are employed to produce a corrosion

resistant coating for ferrous and non-ferrous alloys. Nitriding has been studied to improve the high-temperature oxidation resistance of these types of stainless steels[40,41]. Researchers have also underscored the beneficial effects of reactive element oxide coatings on Cr_2O_3 forming alloys[42,43]. However, an applied coating offers easy processing, relatively low cost and good adhesion between the coating and the substrate.

Air Plasma Spray (APS) has found success in the extrinsic coating development[44] based on powder feed stocks. Achieving nanostructures (10-100nm) using powders is already a proven methodology[45]. Of late, solution precursor plasma spray, a process that uses APS torches with a precursor solution in the form of chlorides or nitrates of the species to be deposited is becoming increasingly important. In this process (SPPS), the precursor solution is atomized through a nozzle in front of the spray torch and deposited subsequently on to a substrate to create various corrosion resistant and thermal barrier coatings[44,46]. The SPPS process has many advantages compared to the conventional Plasma Spray, for example, circumvention of the costly powder-feedstock preparation step and better control over the chemistry of the deposit [47,48,49]. The biggest advantage of the SPPS method compared to conventional methods is that the coating is produced directly from the solution precursor and all the physical and the chemical reactions like evaporation, decomposition and crystallization takes places in one single step [48,50]. The deposited coating can be tailored to be nanostructured[47]. In this study, SPPS has been used to deposit ceria coating on a Martensitic 410 Stainless Steel to improve its high temperature corrosion resistance. Both coated and uncoated samples are subjected to high temperature and the oxidation kinetics is further compared. Post scale characterization is performed to elucidate the oxidation mechanism in the presence of rare earth nanostructured coating.

4.2 Experimental

4.2.1 Processing

Figure 16(a) is a schematic illustration of the Solution Precursor Plasma Spray process. An atomizer nozzle injects the solution precursor into the plasma flame. The martensitic 410 substrate (length 60 mm x width 25 mm x thickness 3 mm) was grit blasted using 60 micron alumina grits. Grit blasting creates enough surface roughness so that the splats are strongly bonded to the substrate. The substrate was treated with acetone to remove any grease or lubricant present in the substrate. The precursor used in this experiment was composed of 75 grams cerium nitrate hexahydrate, 99% in 1.5 liters of Nanopure distilled water. The solution was magnetically agitated for 20 min. The precursor solution was prepared and was fed through the atomizer nozzle in front of the plasma gun (Model SG 100 Praxair TAFA, Concord, NH). Both precursor feed rate and gas flow parameters are optimized before actual coating deposition. A relatively high feed rate will leave a considerable volume of droplets in non-pyrolized state. This will result in a patchy, gel like deposit. However a low feed rate may lead to little or no deposition, resulting in substrate oxidation. Initially when helium was used as a secondary gas with the nozzle location indicated, the coating appeared patchy. The secondary gas was changed to hydrogen with a lower feed rate and the coating properties were optimized. At 7 slm, the coating appeared exactly similar to a powder feedstock coating. The optimized spray parameters used for the spray pyrolysis are listed in Table 5**.** The substrate material used for this study was AISI 410 Martensitic Stainless Steel (SS) of C 0.15 %, Mn 1.00 %, P 0.040 %, S 0.030 %, Si 1.00 % and Cr 12.5 %.

Both bare and Ceria coated AISI 410 grade martensitic stainless steel were oxidized at 1273K (1000^0C) for 12 hours in still air. The oxidation kinetics were continuously monitored using

thermo-gravimetry setup with a microbalance (Saratorius model LA230P ± 0.01 mg), a vertical balance with temperature controlling accessories and a computer to gather the data continuously.

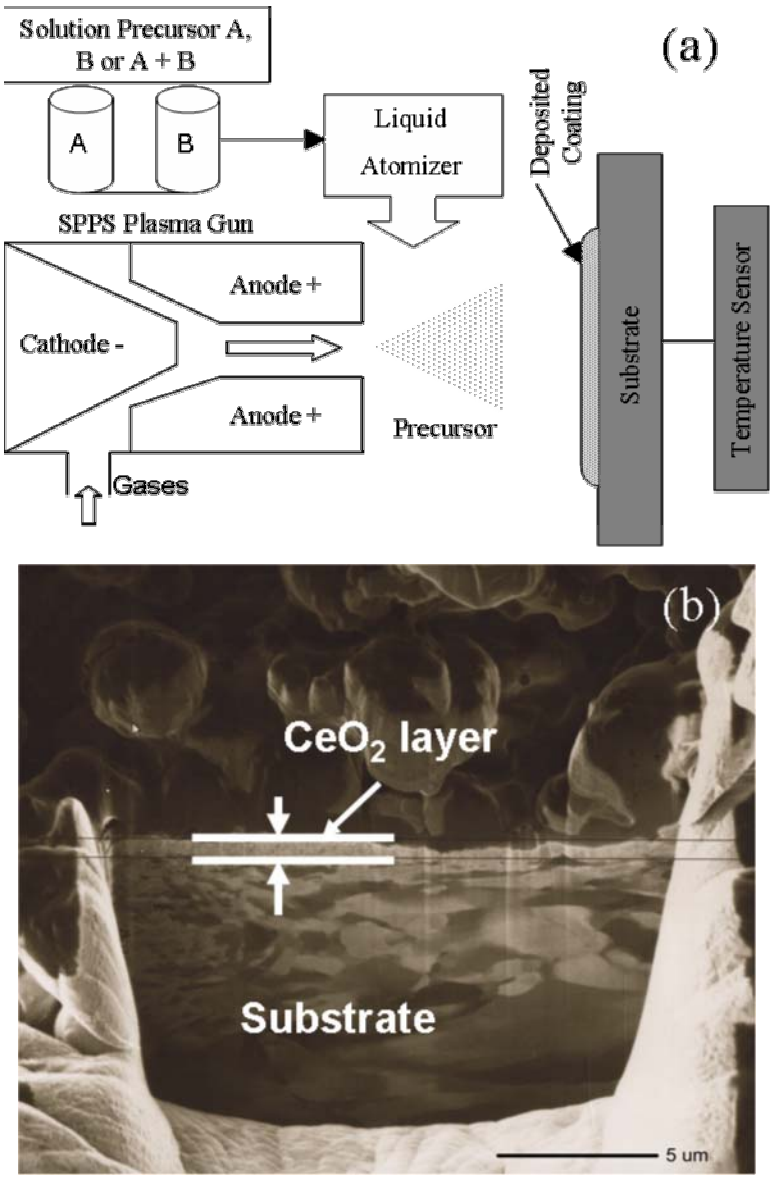

Figure 16 Schematics of SPPS process using plasma spray gun and (b) FIB cross section image of as-coated CeO_2 on SS substrate revealing the coating thickness (~1 μm).

4.2.2 Analytical Investigation

Scanning Electron Microscopy for cross section morphology: The cross section microstructures of the oxide scale on the oxidized and bare specimens were observed using a Scanning Electron Microscope (Model JEOL 6400F , JEOL, Tokyo, Japan).

Table 5 Optimized Spray Parameters from ten sets of experiments for SPPS processing of CeO_2 coating on martensitic stainless steel to obtain an adherent, nanostructured deposit.

No.	Parameter		Optimized Value
1	Liquid feed rate (ml min^{-1})		25
2	Primary gas (Ar) flow rate (slm)		38
3	Secondary gas (H_2) flow rate (slm)		7
4	Arc current (A)		800
5	Arc voltage (V)		45
6	Stand off distance (mm)		75
7	Nozzle Internal Diameter (mm)		7.5
8	Injector position (mm)	From the torch axis	15
		From the nozzle exit	10
9	Torch Efficiency		67 %

Differential Scanning Calorimetry (DSC) studies:Differential Scanning Calorimetry (Model SDT Q600 TA Instruments Inc., Newcastle, USA) of Ce $(NO_3)_3$ has been performed to study the dissociation temperature of cerium nitrate to cerium oxide. The instrument combines DSC and TGA and higher temperatures (up to 1500°C) are accessible with this instrument. Only a few mg of sample is required. Area under the curve marked PQR (see Figure 17(a)) is measured which reveals the enthalpy required for the decomposition to occur.

Focused Ion Beam for coating cross section analysis and TEM sample preparation: The Focused Ion Beam equipment (Model FEI 200, FEI COMPANY, Hillsboro, USA) has a field emission magnum column workstation with a gallium liquid metal ion source (LMIS). Ion emission of a LMIS is achieved with a current density of 10^8 A cm^{-2} at the surface. The lateral resolution for

sample preparation is approximately 5 nm. During the sample preparation, Ga^+ ions are scanned across the sample surface. The same Ga^+ ions are used to image the cross-sectional view during the milling operation. The FIB column is adjustable from 1 pA to 20,000 pA at 30 kV with a lateral resolution of 5 nm.

Transmission Electron Microscopy for nanostructure studies: Imaging the nanostructures of the as-coated specimens was done using a high resolution Transmission Electron Microscope (Model Tecnai F30, FEI COMPANY, Hillsboro, USA) with a field emission gun (FEG) with an operating voltage of 300 kV. EDX from specific locations have been taken using HAADF (High angle annular dark field detector) detector.

X-ray photoelectron Spectroscopy for Surface Chemistry: The surface characterization of the bare and the coated oxidized specimens was performed on a Physical Electronics (PHI 5400) ESCA X-ray Photoelectron Spectroscopy (XPS). Non-monochromatic X-Ray radiation from Mg Kα source at a power watt has been used to get the data from the sample. In order to achieve the maximum resolution, survey spectra and multiplex high-resolution spectra were recorded with pass energies of 35.7 and 17.9 eV, respectively. The spectrometer was calibrated using a metallic gold standard (Au $4f_{7/2}$ = 84.0 ± 0.1 eV (Spin Orbit splitting of f level to $f_{5/2}$ and $f_{7/2}$ due to ionization and the binding energy from $f_{7/2}$ level is verified)). Charging shifts produced by the specimen were removed by using a binding energy scale referred to that of C (1s) of the hydrocarbon part of the adventitious carbon line at 284.6 eV. Subsequently, nonlinear least-squares curve fitting was performed using a Gaussian–Lorentzian distribution. Curve fitting is accomplished by first smoothing the data using a Savitsky-Golay routine and then fitting this smoothed data by assuming a 100% Gaussian peak shape. The value for the full width at half

maximum (FWHM) was obtained from the standard sample analysis for curve fitting. All data smoothing and curve fitting is performed using Peak Fit ^{TM} software (version 4.05, SPSS Inc.) with modified fit routine. XPS provides both quantitative elemental and chemical states information on virtually any vacuum compatible surface (3-5 nm).

X-ray Diffraction for structural and crystallite size determination: X-Ray Diffraction analysis was done using a Rigaku XRD to study the compounds formed during the coating as well as to ascertain the structure of the oxide scales formed on the substrate after oxidation. Cu Kα radiation (λ=0.15406 nm) is used for the analysis at 40 kV and 30 mA settings. The phase identification has been carried out by referencing the software PCPDFWIN version 2.02 containing the JCPDS (ICDD) database files. The particle size calculation for ceria has been done using the full width at half maximum (FWHM) of those peaks. The Scherrer formula involves the determination of crystallite size as a function of full width at half maximum value of the peak corresponding to the compound and the Θ value of the peak location.

4.3 Results and Discussion

4.3.1 Thermodynamic Consideration:

In the SPPS process, the chemical reactions are more complex. There are competing chemical reactions that try to dissociate the nitrate precursor to its respective elements and subsequently form oxides in the environment. The chemistry taking place inside the plasma is obtained from the chemical equilibrium calculations. Cerium Nitrate is atomized in the plasma plume at a temperature between 8000 K and 13000 K with the solution canister pressurized to 310 kPa. Both Ar and H_2 are being used as primary and secondary gases respectively to generate the

plasma plume. This will cause dissociation of cerium nitrate to cerium oxide, NO_2 and oxygen as shown in the reaction as shown below in equation 1.

$$Ce(NO_3)_3 \xrightarrow{\Delta} CeO_2 + 3NO_2 + \tfrac{1}{2} O_2 \qquad (1)$$

This is an endothermic reaction that has been corroborated by DSC analysis. As shown in Figure 17(a), the dissociation reaction starts at 263^0C, culminates at 299^0C and the reaction is complete at 392^0C. The enthalpy of the endothermic reaction that triggers the formation of CeO_2 is found to be 208.8 J/g of $Ce(NO_3)_3$. A net enthalpy of 15.6 kJ of heat energy is utilized in the whole process to convert the cerium nitrate to cerium oxide. The enthalpy of the plasma comprising of argon and hydrogen gases can be calculated using equation 2 [51]:

$$\Delta H = \frac{[\sum_{i=1}^{i=k} x_i . \Delta h_i]}{[\sum_{i=1}^{i=k} x_i . M_i]} \qquad (2)$$

In equation 2, M_i, Δh_i and x_i are respectively, the mass of one mole, the enthalpy of one mole, and the molar fraction $x_i = n_i/n_t$ of the chemical species i (Ar and H_2). The enthalpy of Hydrogen (15 vol %) – Ar mixture will be 20 MJ/kg based on this calculation which is more than sufficient to convert the cerium nitrate to cerium oxide. The heat energy achieved as a result of dissociation of Hydrogen is crucial to take care of the plasma jet cooling by water vaporization. Hydrogen flow rates less than 7 standard liters per minute (slm) will quench the plasma jet significantly. The remaining heat was insufficient to pyrolyze incoming liquid to get pyrolized. Hence, a Hydrogen flow rate was optimized to 7 slm for coating deposition. The Gibbs free energy plot

for dissociation of cerium nitrate to cerium oxide is presented based on the thermodynamic calculations (Figure 17(b)). The area under the curve obtained by the DSC plots for different temperature ranges is used to calculate the specific heat capacities of the form

$$C_p = a + bT + cT^{-2} \qquad \text{——— (3)}$$

Three different algebraic equations are used at different temperature ranges to calculate a, b and c. The values of a, b, c for different temperature ranges are tabulated in Table 6. The entropy (ΔS) is calculated using values of C_p.

The overall Gibbs free energy for appropriate temperature ranges (Table 6) is calculated from equation 4 to be:

$$\Delta G = \int_{298}^{T} [(a + bT + cT^{-2}).dT + T.\int_{298}^{T} (\frac{(a + bT + cT^{-2})}{T}).dT \qquad \text{——— (4)}$$

Table 6 Values of Specific Heat Capacity constants along with temperature ranges for Cerium oxide.

a	b	C	Temperature range
1.1	8.32	0.5×10^{-4}	298-850 K
3.6	29.43	0.95×10^{-4}	851-1400 K
8.1	33.29	1.3×10^{-4}	1401-1900 K

The Gibbs free energy for the dissociation of cerium nitrate to CeO_2 (ΔG_d) as a function of temperature is presented in Figure 17(b). ΔG_d value is 0 at 298^0C and becomes negative thereafter, revealing that the dissociation reaction is thermodynamically feasible. As the temperature increases, for example at 325^0C, the ΔG_d value is -1000 J/Mole which further decreases to -4000 J/Mole at 400^0C thereby increasing the chances of formation of CeO_2 with

increasing temperature (see Figure 17(b) inset). The data presented in Figure 17(b) proves that the formation of CeO_2 coating from cerium nitrate precursor solution is thermodynamically feasible.

4.3.2 Structural Analysis using XRD

XRD analysis as revealed in Figure 18 confirmed the presence of nanocrystalline ceria (CeO_2). The h,k,l planes of the coated ceria matched with that of the JCPDS database of CeO_2. The diffractogram indexed for the hkl planes and 2θ positions matched with those of ceria and the peak broadening is due to the nanostructured nature of the coating. Debye-Scherrer formula has been used to calculate the crystallite size (D) as shown below,

$$D_{hkl} = \frac{k\lambda}{B.\cos\Theta} \quad \text{——————} \quad (5)$$

where k is a constant , λ is the wavelength of x-rays used in X-Ray diffraction experiment, B is the full width at half maximum, Θ is the diffraction angle that follows Bragg's law of diffraction. The crystallite size of CeO_2 thus calculated is in the range of 12- 40 nm.

4.3.3 Formation of Nanostructures and the Coating Chemistry

Both TEM and diffraction analysis were performed on the FIB prepared sample to calculate the particle size and the crystalline structure of the coating. Image analysis revealed average particle size around 30 – 50nm (Figure 19). The diffraction ring pattern indicates a polycrystalline fluorite structure in the layer (Figure 19b (Inset)). EDS HAADF was performed to identify the elemental concentration in the scale.

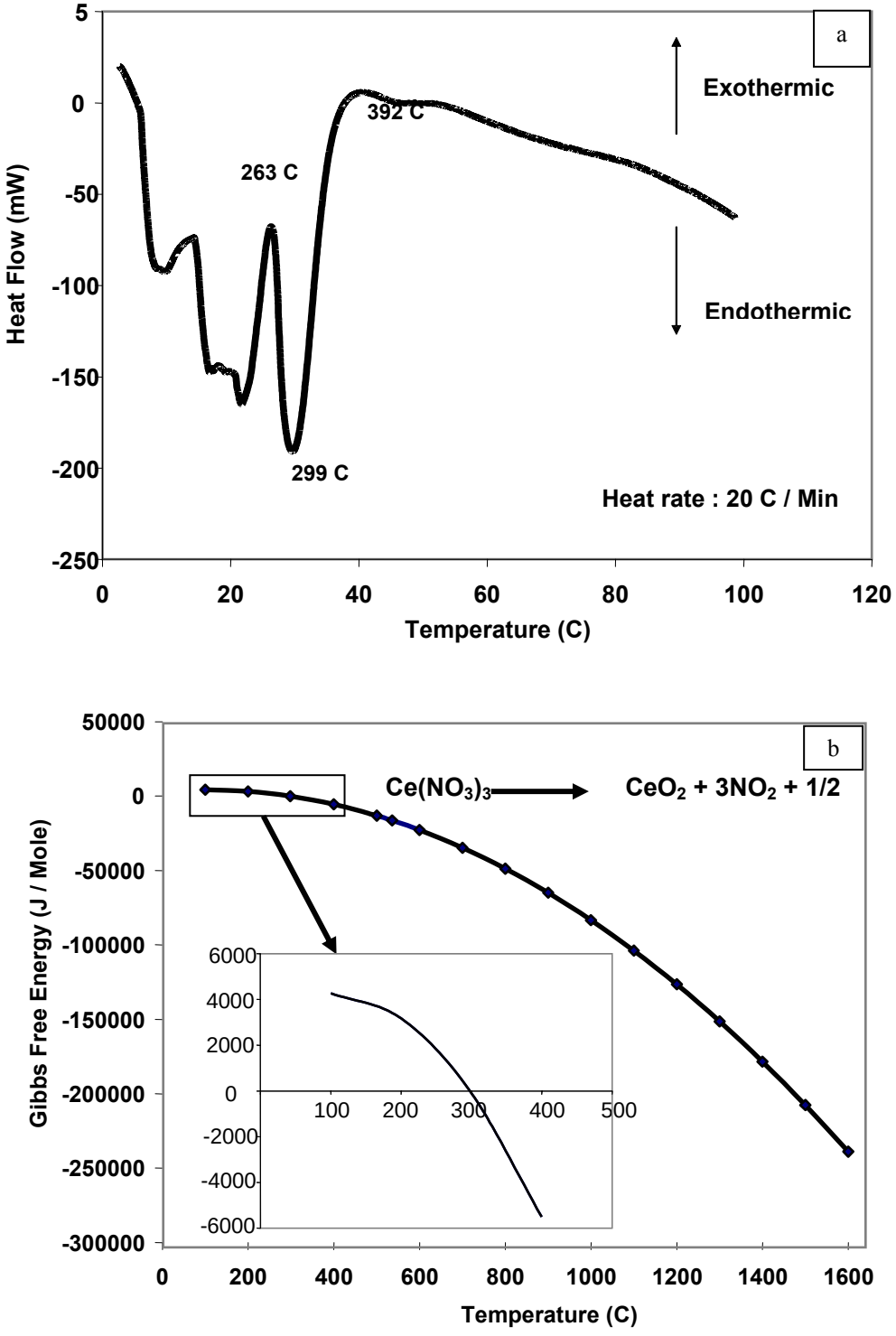

Figure 17 Decomposition behavior of cerium nitrate illustrated by showing variation of heat flow with temperature as measured using Differential Scanning Calorimetry, (b) A plot of Gibbs free energy as a function of temperature for the same.

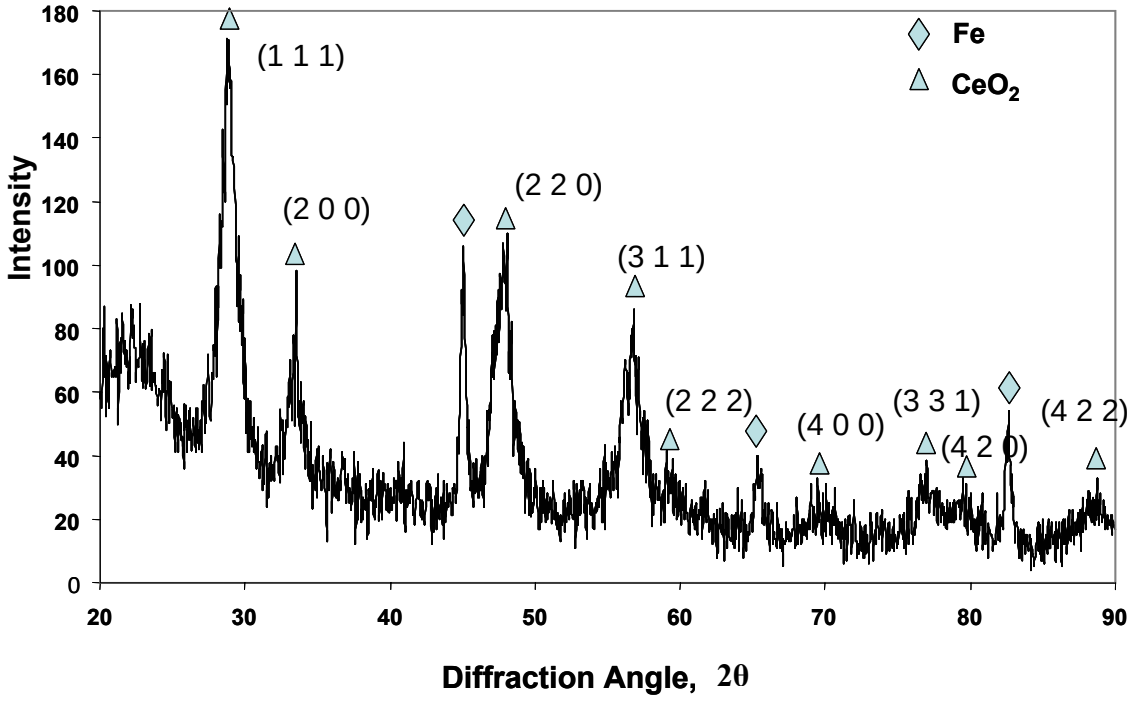

Figure 18 X-Ray Diffraction pattern of cerium oxide coating on stainless steel substrate.

Figure 19c shows the area of analysis with corresponding EDX spectrum. The spectrum (Figure 19d) indicates the presence of Ce at 6 kV energy.

In the plasma flame the temperature can approach as high as10^4 K, along with flame velocities in 200-300 m/s[47]. The rate at which the particle formation occurs is significantly higher. By varying the secondary gas flow rates, the enthalpy can be varied and thereby the particle formation rate. The whole process of formation of nanostructures can be classified in to three steps [48]viz. (1) Precursor evaporation, (2) Condensation of solid phase precursor, (3) Chemical reaction begins and the grains begin to nucleate and grow.

During the course of any of these steps, if any of the parameters such as gas flow rates, the substrate stand off distance are not appropriate, it might lead to two different extremes such as, patchy gel-like deposit or coarse grained structure. The 30-50 nm aggregates that are seen from TEM analysis are most likely formed after step 3 above.

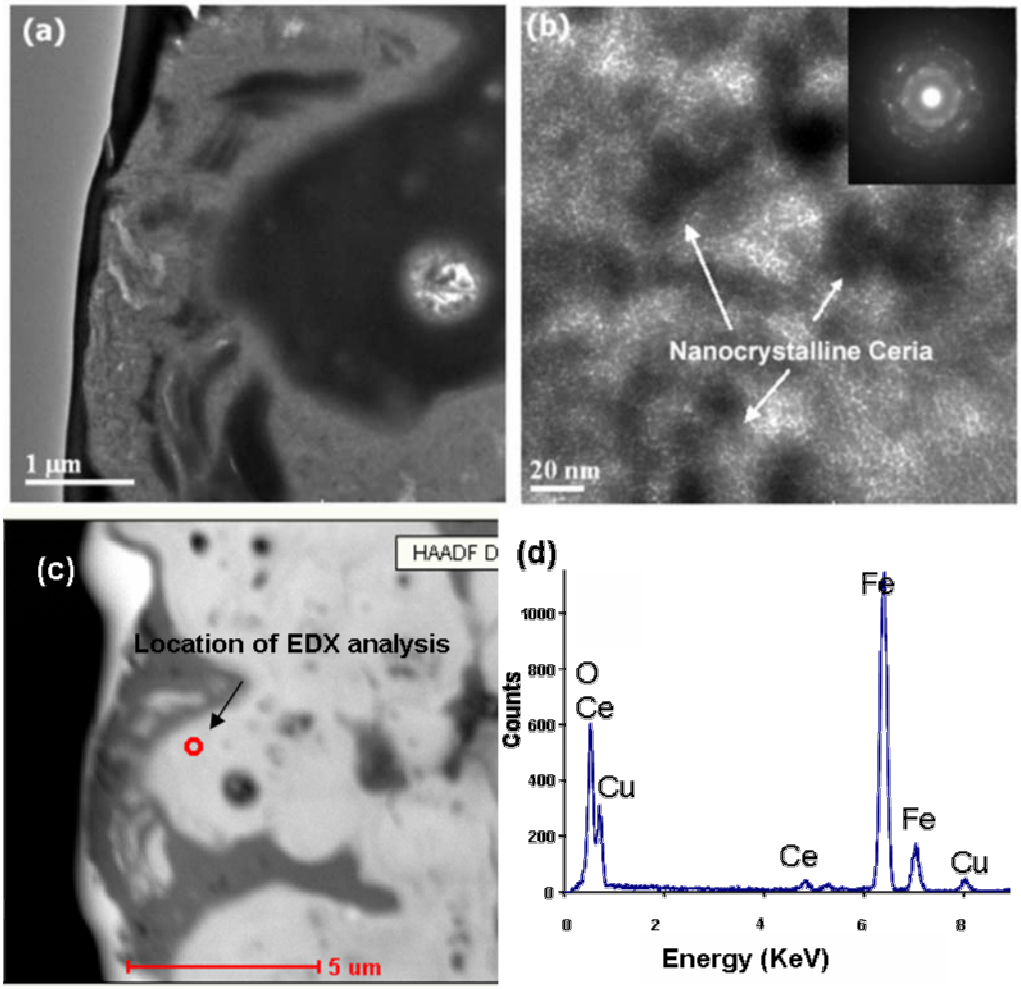

Figure 19 Transmission Electron Microscope image of (a) Overview of the SPPS Ceria coated sample and (b) high magnification image showing particle sizes around 30 –50nm.(Inset: SAED pattern indicates nanostructured polycrystalline Ceria), (c) location of EDX HAADF analysis for determination of elemental composition and (d) the results of the spectrum. Cerium and Iron concentration peaks high at 1 and 6keV energy intervals.

The XPS analysis of the as-coated surface reveals the presence of both Ce^{3+} and Ce^{4+} valence states in the coating as shown in Figure 20. The ratio of the integrated area of the curves belonging to Ce^{3+} (curves numbered I, III, VI, VIII) to the total integrated area of all the 10 curves put together will give the concentration of Ce^{3+}. The Ce^{3+} concentration was 40%., which corresponds to the presence of nanoceria grains as reported earlier by our group[52]. The presence of Ce^{3+} creates oxygen vacancies that will induce more inward diffusion of oxygen compared to its competing mechanism of outward diffusion of elements such as Cr and Fe present in the substrate. Such diffusion will help in avoiding void formation and will lead to a more adherent scale as observed in the oxidation kinetics discussed later.

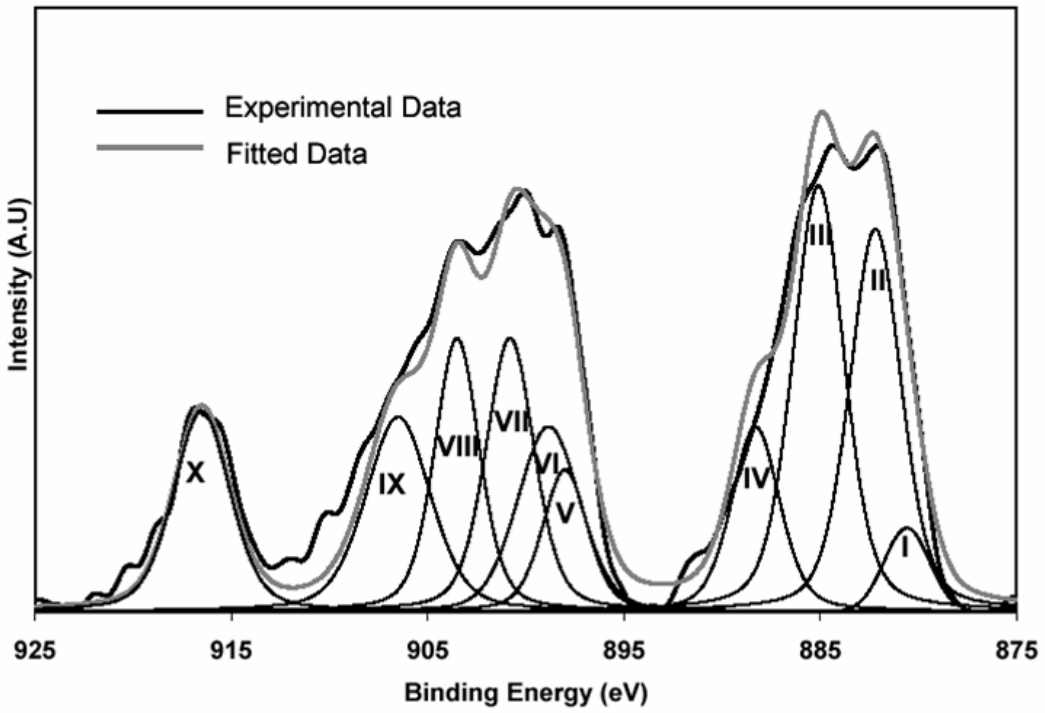

Figure 20 XPS spectrum of peak fitted Ce (3d). peaks from the SPPS processed CeO_2 coating on the 410 Martensitic substrate marked I , III, VI and VIII (880.20eV, 885.0eV, 899.50eV, 903.50eV respectively) represents Ce^{3+} while peaks from II, IV, V , VII, IX,X (882.10eV, 888.10eV, 898.00eV, 900.90eV, 906.40eV, 916.35eV respectively) are from Ce^{4+} ions. Peak marked X is a satellite peak indicating the presence of +4 states of ceria.

4.3.4 Oxidation Kinetics and Scale Characteristics

Kinetics: The oxidation kinetics at 1273 K of the bare and coated 410 martensitic stainless steel are presented in Figure 21a. The nanoceria coated sample improved the high temperature oxidation resistance to a large extent. The first oxidation cycle performance which comprised of heating at 1273 K in dry air and then furnace cooling to room temperature was re-oxidized to find out the effect of thermal cycling on these steels. The kinetic plot for re-oxidation is also presented in Figure 21b. There is negligible mass gain during such re-exposure. This is a testimony for the fact that coating is effective after a second exposure to a relatively high temperature. The isothermal parabolic rate constant (k_p) values for bare oxidized sample are calculated to be 2 x 10^{-6} kg^2 m^{-4} s^{-1} after first cycle and for SPPS ceria oxidized sample the values are 1 x 10^{-6} kg^2 m^{-4} s^{-1} after cycle I and 4 x 10^{-8} kg^2 m^{-4} s^{-1} after cycle II. The oxidation rate was reduced by 50% in the presence of SPPS nanoceria coating.

Cross-section Analysis: In order to verify the appearance of the coating and the adherence of the coating to the substrate, a FIB image of the coating cross section is shown in Figure 16(b). It is to be noted that the coating was adherent without presence of any cracks. Dense, fine spherical size particulates have been obtained by a series of events i.e precursor evaporation, condensation of solid phase precursor and the nucleation and growth of the CeO_2 particles. These particulates gain enough velocity from the plasma plume to impinge on to the substrate by a combination of sintering and entrapment in between the deposited particulates. Splat formation is unavoidable but the size of these splats are usually an order of magnitude smaller than those obtained by powder feedstock deposition using APS[53].

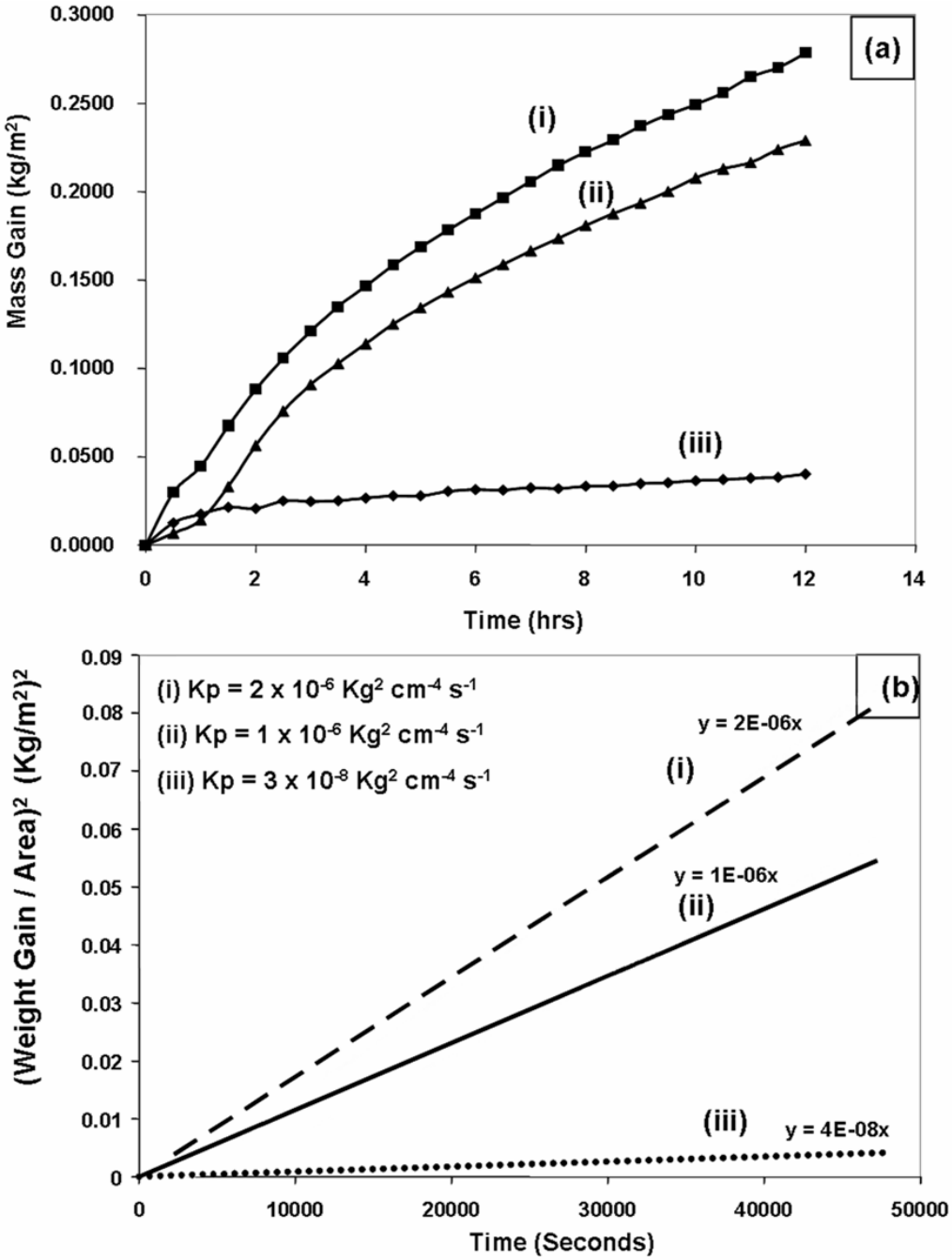

Figure 21 (i) Mass gain per unit area of bare steel sample with time during oxidation and (ii) Ceria coated sample for oxidation cycle I and (iii) cycle II. (Temperature of oxidation is 10000 C) (b) Plots showing the slope values (kp) of the square of weight gain per unit area vs time (sec) obtained from oxidation data. (i) Bare sample and (ii) Ceria SPPS coated for oxidation cycle I and (iii) Ceria SPPS coated sample for oxidation cycle 2.

SEM was employed to perform cross section analysis on the oxidized specimens at 15kV. Figure 22 shows a scale comparison of the bare oxidized sample with the SPPS coated sample. The bare oxidized sample showed a 300 micron oxide scale while the SPPS ceria coated sample showed much smaller oxide scale thickness (~10 – 15 micron), almost 30 times lower. The SEM images of the bare oxidized sample revealed the presence of horizontal cracks, which subsequently leads to the delamination of the oxide layer. Further exposure of the material underneath will lead to degradation when exposed to high temperatures.

The high temperature protection of the martensitic steels in presence of nanoceria coating can be attributed to the early formation of Cr_2O_3 healing layer. Earlier, our group[54] have discussed the beneficial effect of nano ceria in imparting high temperature oxidation resistance to 304 grade stainless steels compared to micron ceria. This provides numerous nucleation sites for Cr_2O_3formation at the initial stages of oxidation. Chromium oxide acts as an impervious layer to prevent outward migration of cations and inward migration of oxygen ions. Nano cerium oxide coating enhances the rate of Cr_2O_3 formation compared to conventional micron sized ceria. The segregation of nanoceria particles on the oxide grain boundaries might also prevent the outward cation migration and thereby imparting the necessary protection[55].

Surface Chemistry: In order to validate the surface oxide chemistry, XPS survey (Figure 23c) on as-coated sample was performed. The spectrum confirmed the presence of Ce and also indicated the presence of Fe from the substrate. The XPS survey spectra of both coated and bare oxidized samples are presented in Figure 23 a and Figure 23 b.

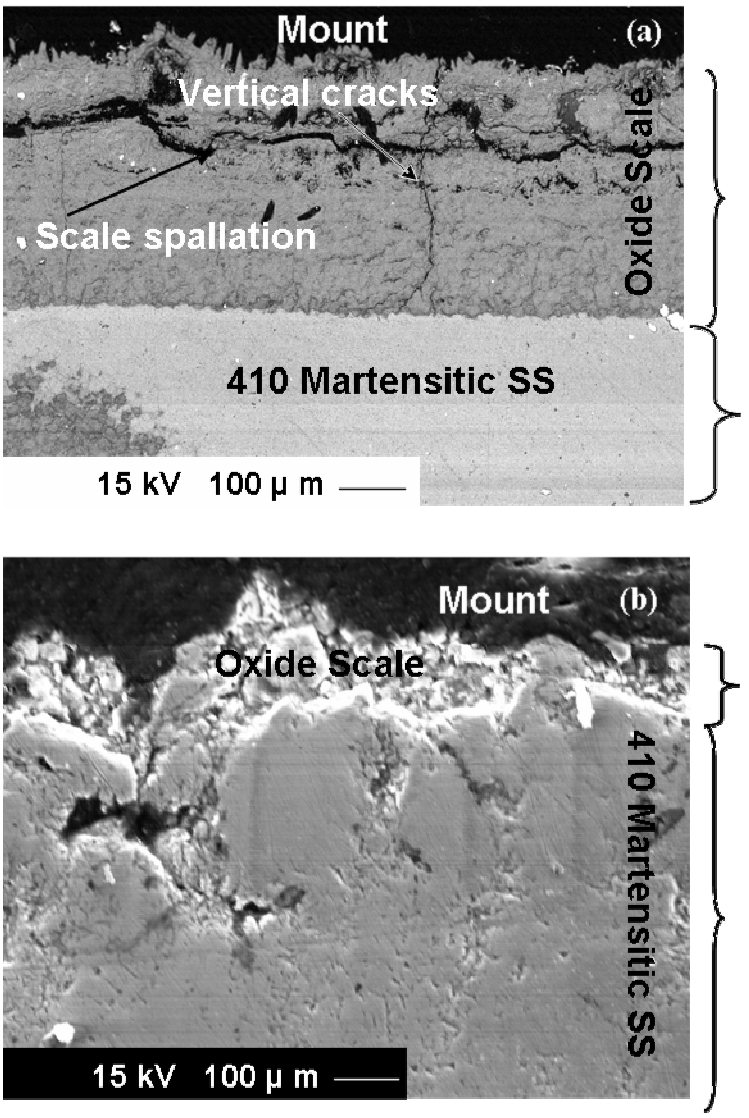

Figure 22 SEM images of 410 Martensitic Stainless steel cross section (a) Uncoated (bare) oxidized and (b) SPPS nano ceria coated oxidized sample at 1000^0 C for 24 hours

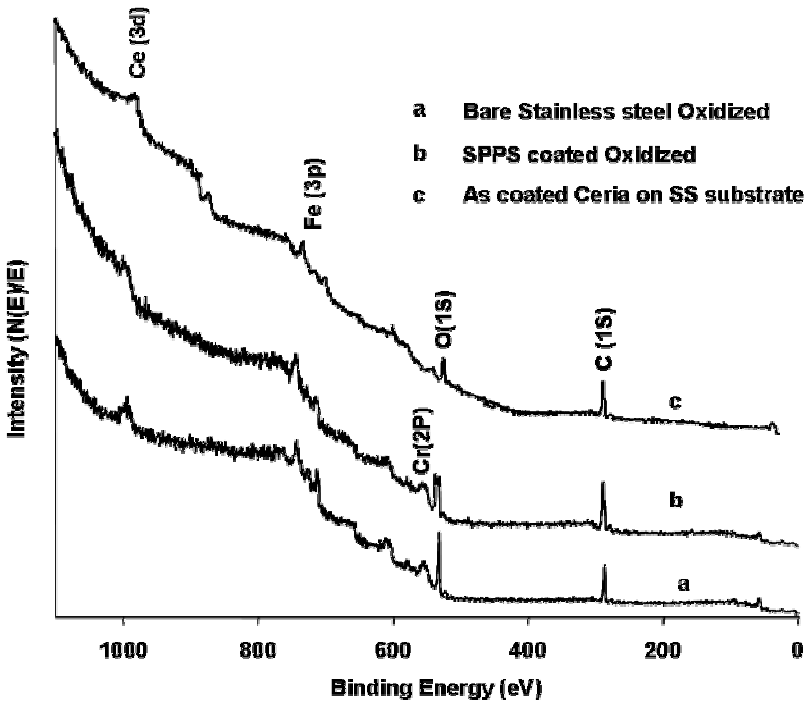

Figure 23 XPS survey spectrum of (a) nanoceria coated oxidized SS, (b) bare SS exposed at 1000^0C for 24 hours. Note the presence of Ce (3d), Fe (the formation of CeO_2, Fe_2O_3 and Cr_2O_3 type of oxides. and (c) XPS survey spectrum of the as coated ceria on 410 martensitic stainless steel (SS). Note the presence of Ce peak at 886.75 eV indicating the formation of CeO2 in the coating. The presence of Fe is from the background substrate.

At any given depth, proportion of Fe to O or Cr to O will be lower in case of bare sample compared to the coated sample which is corroborated with the XPS elemental ratio calculation (Table 7).

Table 7 Calculated Elemental ratios from the XPS survey spectrum for Bare oxidized and SPPS Ceria Samples using peak area and sensitivity factors. (Error: ± 0.15)

Ratio	Fe/O	Cr/O	Cr/Fe
Bare Oxidized	0.493	0.342	0.694
SPPS Ceria Oxidized	0.671	0.625	0.931

The difference in the Cr/Fe ratio of both the samples can be explained from the point of view of difference in the diffusion rates of Cr and Fe towards the surface. The diffusion of Fe towards the surface is lower in the coated sample. X-Ray diffraction studies on the coated oxidized samples also reveal the formation of Cr_2O_3, Fe_2O_3, CeO_2 and $CeCrO_3$. From the diffractogram (Figure 24), the nucleation of chromium oxide (from the peak intensity of Cr_2O_3) is highly favored in presence of nanoceria coating.

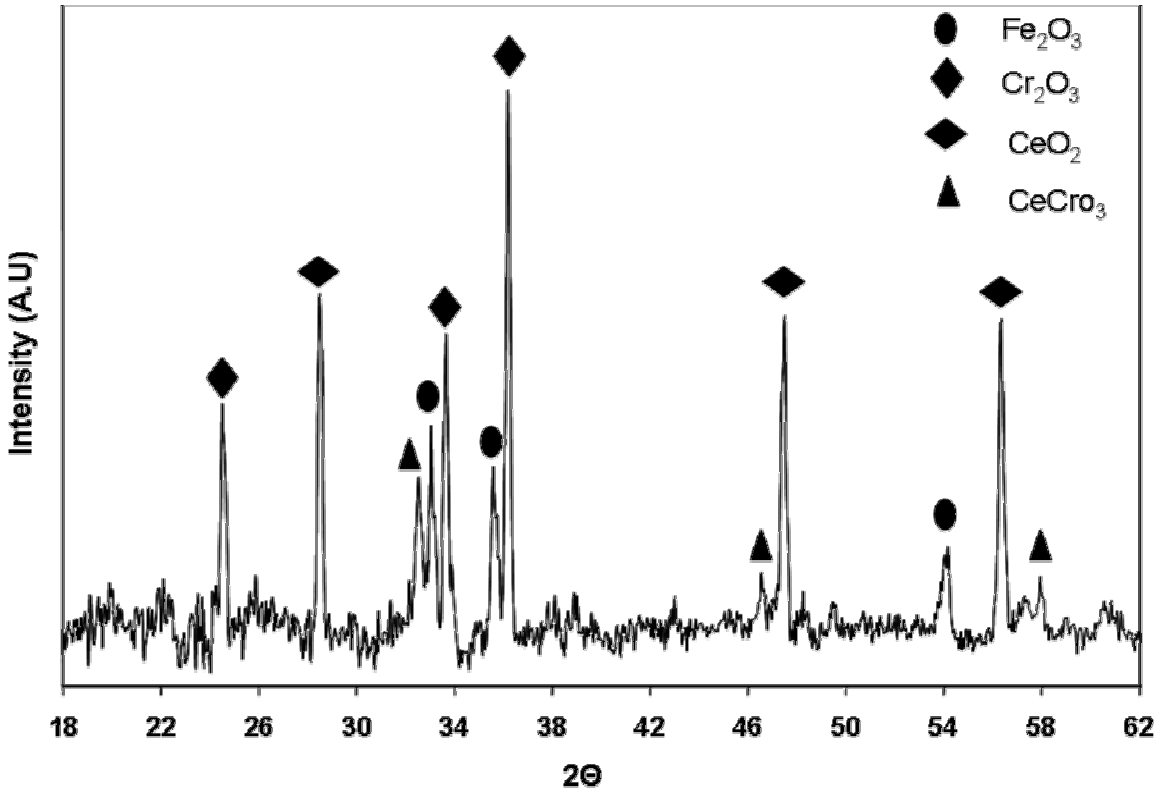

Figure 24 XRD Spectra for coated sample oxidized at 1000^0C for 2 cycles each of 12 hour duration with the formation of different oxides.

On the other hand, in the case of bare sample, the XPS elemental ratio of Cr/Fe as shown in Table 7 confirmed that more Fe is present in the surface thereby making the substrate more vulnerable to further degradation by outward cation migration. Therefore, the oxidation

protection is basically attributed to the presence of Cr species in the coated sample. The presence of the $CeCrO_3$ could also be one of the sources for the protective nature of the coating.

Individual chromium peaks from XPS multiplex data are studied in depth by deconvoluting the Cr ($2p_{3/2}$) peaks from the bare and coated oxidized samples using a Savitsky-Golay smoothing routine.

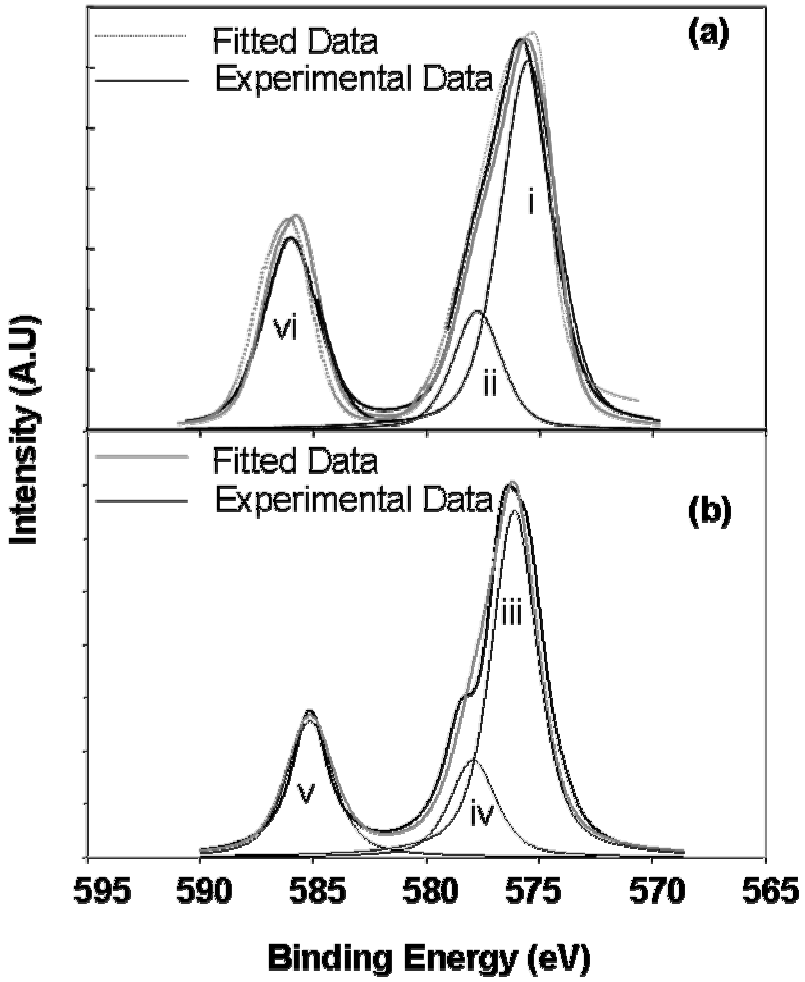

Figure 25 Deconvoluted XPS Cr(2p) peaks from (a) Bare Oxidized (i) $MnCr_2O_4$, (ii) $Cr(OH)_3$ and (b) Ceria Coated Oxidized 410 Stainless steel (iii) Cr_2O_3 (iv) Cr-Cr-O oxides, (v and vi are from Cr 2p1/2).

Similar curve fitting has been useful for studying the oxidation states of Chromium in Fe-Cr alloys[56]. The peak positions for various oxides formed during the course of oxidation are shown clearly in Figure 25. The coated oxidized samples showed presence of multiple Cr containing oxide species. In other words, Figure 25b reveals peak at 576.1 eV which belongs to Cr_2O_3[57] and, 577.9 eV which may be Cr-Ce-O oxides, where as bare oxidized samples had a few chromium oxide peaks (577.4 eV and 575.72 eV) which could be indexed for $Cr(OH)_3$[57] and $MnCr_2O_4$[57] respectively. The prominent presence of Cr_2O_3 peak (576.1 eV) in the coated oxidized specimen is conspicuously absent in case of the bare oxidized sample**.**

Thus early formation of chromium oxide in presence of nanoceria is a major factor in preventing high temperature oxidation and is consistent with the oxide kinetics results shown previously where, the rate constant was lowered by two orders of magnitude (after second cycle) as shown in Figure 21a. Outward diffusion of Iron (Ionic diffusion) occurs during oxidation of the bare oxidized specimen[56]. Cation vacancies are created at the scale–alloy interface as a consequence, which forms voids by the vacancy-condensation mechanism. As a result, the oxide layer separates from the alloy substrate as shown in Figure 22(a). However, in the presence of nanoceria, due to a possible inward movement of oxygen ions (as shown by XPS Cr/O ratio, O is less in the surface ceria coated oxidized sample due to movement of O ions inside) thwarts the formation of any voids thereby preventing the oxide layer from getting detached from the alloy substrate.[54] Figure 22(b) reveals a very thin oxide scale formation and the scale thickness is reduced to 10 μm compared to bare oxide scale thickness of 300 μm.

Thus the presence of SPPS fabricated nanostructured ceria coating protected the high temperature degradation of martensitic stainless steel but changing the oxidation mechanism

from cation outward to anion inward by catalyzing a early formation of chromium oxide healing layer.

4.4 Conclusions

SPPS was successfully utilized in the fabrication of nanostructured ceria coating on a Martensitic steel. Gas flow rates, solution feed rate, substrate stand off distance have been optimized to achieve a dense nanostructured coating. From the first principles of thermodynamics, the feasibility of the dissociation of cerium nitrate to cerium oxide is found at 298^0C and further correlated with the DSC analysis. Subsequent exposure to high temperature oxidation at 1000^0C for 24 hours revealed the protective nature of the nanoceria coating as compared to the bare substrate. The oxidation kinetics is parabolic in nature and the kp values were reduced by two orders of magnitude compared to the uncoated sample. It is hypothesized, that the presence of CeO_2 acts as nucleation sites for the chromium oxide (Cr_2O_3) formation to prevent material degradation. Further, the presence of CeO_2 nanoparticles blocks the outward diffusion of Fe and favors more inward movement of O ions negates the formation of voids which will avoid delamination of oxide scale. Oxide scale chemistry revealed the presence of mixed oxides of Cr_2O_3, CeO_2 and $CeCrO_3$, key to the development of high temperature oxidation resistance coatings.

CHAPTER 5 Ni-Al_2O_3 NANOCOMPOSITE

5.1 Introduction

Metallic particles are often reinforced in the ceramic matrix for developing materials with high toughness[58] and fracture strength[59-62]. Al, Mo are some of the metallic particle reinforcements for reinforcing ceramic matrices to improve such properties[63-64]. Of late, such metal ceramic composites are extended towards making one of the components in nanometer dimensions to further improve the mechanical properties. Nanocomposites, the term being used to describe a composite material with at least one of its phases with dimensions in nanometers. Nanocomposites have shown excellent catalytic properties[65] with improved mechanical, magnetic properties as compared to its bulk counterparts[66-68]. Such metal-ceramic nanocomposites are developed using processes such as Hot Isostatic Pressing[67], Spark Plasma Sintering[69], Laser- Based Techniques [70], Processes such as gel casting, infiltration followed by Pressureless Sintering[71-73], Soaking and pulse electric current sintering[74]. Of importance, Ni particulate reinforced Alumina composites showed promise in both mechanical and magnetic applications[67-68]. Particular interest lies in improving high fracture toughness. The strengthening mechanisms can be attributed to the blunting of cracks due to the presence of nanosized Ni particle uniformly distributed in the matrix. The reason behind using Nickel as reinforcement is its high temperature stability and chemical inertness in comparison to Copper and Aluminum. Having realized the potential of Ni-Alumina nanocomposites, it is essential to appreciate the advantages and disadvantages of each of the processing techniques listed above and to optimize the resource parameters to achieve the desired properties. So far, an optimum fracture strength and fracture toughness value for Ni-alumina nanocomposite that has been achieved is 980 MPa and 4-5 $MPa.m^{1/2}$ through a soaking and Pulse Electric Current Sintering (PECS) technique[74]

Researchers came across several obstacles such as coarsening of metallic particles[75-76] during conventional sintering processes. Since these processes involved high temperatures and time involved during sintering stage, nickel particle coarsening to the tune of at least 5 times its original particle size was inevitable. However, consolidation of nanocomposites to make a bulk part has always remained a challenge especially in terms of material fabrication. Chen et.al[71] have developed Ni-Alumina nanocomposites with a final size of 4 x 3 x 40 mm (a plate) after a sintering treatment at 1400^0C for 2 hours. Aharon et.al prepared alumina using slip casting followed by infiltration of Ni-nitrate solution. The whole operation took more than 3.5 hours get a specimen of dimension 50 x 10 x 10 mm[67]. It is evident that such processes are time consuming and even metal dispersion was challenging. Besides, bulk free form part is far from reality.

In this study, electroless coating, a technique conventionally used to increase the surface energy of ceramics for facilitating melt infiltration of ceramics in molten metals has been innovatively used for uniform distribution of Nickel in Alumina matrix prior to processing. The effect of laser and plasma in the processing of free form bulk metal-ceramic composites with nanostructure retention, and effect of processing parameters in achieving the properties are discussed.

5.2 Experimental

The material used were high purity Alumina (99.55%, 38 Alundum, Norton Materials) powders. For nickel electroless coating, Stannous chloride, Palladium chloride, and Nickel Sulphate were purchased from the Sigma Aldrich Chemical Company.

5.2.1 Electroless coating of Ni of alumina powder

Al_2O_3 powder with 15- 60 microns size range and 99.95% purity were used for coating. Alumina powders were immersed into acid stannous chloride ($SnCl_2$) solutions for sensitization of Al_2O_3

particles. Following sensitization, the powders were immersed into the acid palladium chloride ($PdCl_2$) solutions, in which Pd^{2+} reacted with Sn(OH)Cl to form Pd nuclei on the Al_2O_3 surfaces. The electroless bath composition was Nickel Sulphate containing sodium hypophosphite as a reducing agent. A flow chart indicating the chemistry of the electroless coating process is presented in Figure 26. Using the electroless coating technique, alumina particles were coated with a 30 nm thick nickel layer which corresponds to 3-4 wt% of Ni loading in the alumina matrix. The morphologies of the as-coated powders were characterized through Scanning Electron Microscopy (SEM JEOL 6400F).

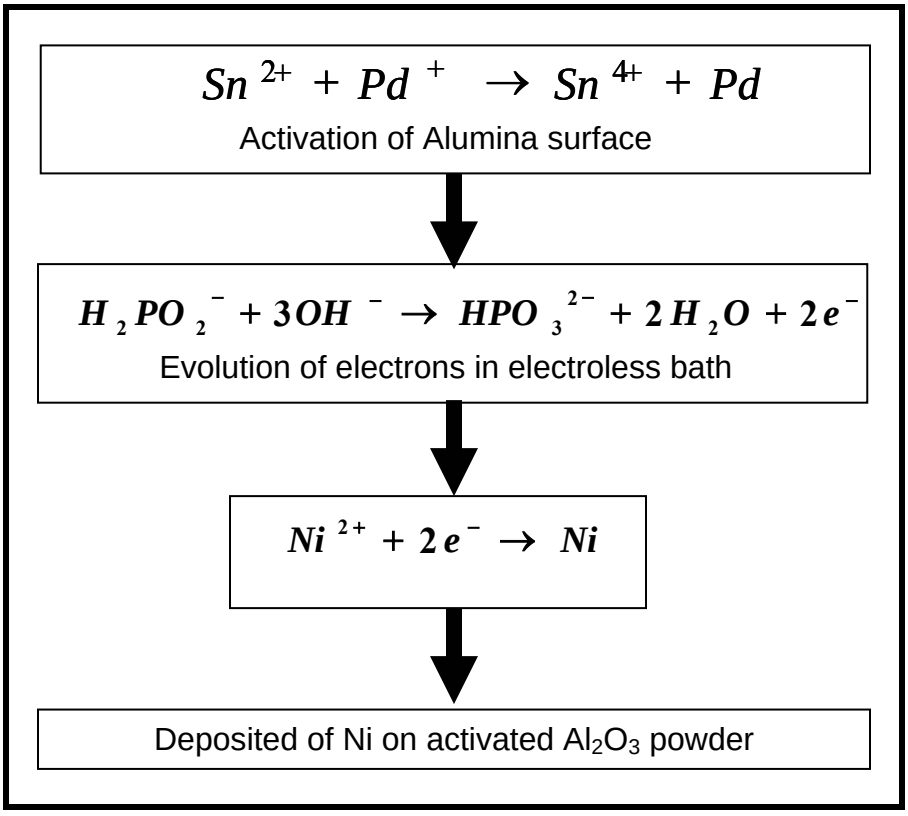

Figure 26 The chemistry of Electroless Ni-coating on Al_2O_3

The thickness of the electroless coated Nickel Layer is characterized through Focused Ion Beam (FEI 200 TEM-FIB System). The chemical compositions of the coated powders were determined by using a PHI 5400 XPS with 1253.6 eV energy of Mg-Kα X-rays at a power of 350 W.

5.2.2 Consolidation Techniques

Laser processing: Laser processing was carried out in an argon protective atmosphere where 1 mm thick preplaced coated powder layer were illuminated by a continuous Rofin Sinar 2 kW Nd: YAG laser beam (1.06 μm wavelength) at two different regimes. First, the preplaced powder was scanned (167 mm/s) with a laser beam close to its focal point (+10 mm) using four different constant laser power: 250, 300, 350 and 400 W. The laser beam has a circular shape with a Gaussian power density distribution and the beam diameter (87% of laser energy inside the particle diameter) is 2.0 mm. In the second regime the preplaced powder was illuminated for 0.3 s by the highly defocused laser beam (+50 mm; 8 mm beam diameter) with a laser power of 200 W. Illuminated samples were observed using a Philips XL30 FEG scanning electron microscope using both SE and BSE detectors.

Plasma Processing: A cylindrical mandrel made of 6061 aluminum was used to deposit the Ni-coated aluminum oxide powder. The machined mandrel had a surface finish of 0.5 micron. The mandrel was degreased and thoroughly cleaned in acetone prior to plasma spraying. Plasma spraying of the powder mixture was carried out using Praxair surface technologies (Indianapolis, IN) SG 100 plasma spray system. Argon was used as the primary gas and Helium was used as a secondary gas. Plasma spray parameters used for the process are mentioned in Table 8. Plasma spray parameters were controlled to minimize the coarsening and melting of electroless coated nano Ni layer. The mandrel has been actively cooled during plasma spraying to prevent the

particles from getting coarsened. The powder was spray deposited to a cylinder of wall thickness 3 mm. After spray deposition, mandrel was cooled with liquid nitrogen to facilitate the release of the spray formed nanocomposite shell, due to difference in the coefficient of thermal expansion values between the mandrel and the deposit.

Table 8 Plasma spray parameters for fabrication of Ni-Alumina bulk part.

Parameter	**Value**
Current (Amperes)	800
Voltage (Volts)	35
Primary Gas Flow rate (SCFH)	80
Standoff distance (mm)	3 inch
Rotational speed of the substrate (rpm)	25
Temperature of the substrate	450^0 C

5.2.3 Characterization

The spray deposited Nickel reinforced Alumina nanocomposite has been characterized using Scanning Electron Microscopy, Focused Ion Beam, X ray Photoelectron Spectroscopy (XPS) and High Resolution Transmission Electron Microscopy (HRTEM). The uniform dispersion of Nickel in Alumina is studied using JEOL 6400F Field Emission Scanning Electron Microscope (SEM). Due to the possibility of formation of Nickel oxide during spray, the sprayed bulk part has been analyzed for the presence of Nickel oxides using X-Ray Diffraction (XRD). Also, the residual stresses developed in the nanocomposite have been analyzed using the XRD technique. HMV-2 Shimadzu model microhardness tester has been used to determine the hardness and hardness of the sprayed part. Fracture toughness was calculated by measuring the length of the crack at the tip of the indentation obtained using a load of 19.6 N for 15 seconds and substitution of the crack length measured in the equation mentioned by Evans and Charles[77]. Density of the bulk nanocomposite has been determined using Archimedes displacement method. A FEI 200

TEM-FIB (Focused Ion Beam) equipped with a 25-50 KV gallium liquid metal ion source (LMIS) was used for preparing thin TEM specimens. High Resolution Transmission Electron Microscopy (HRTEM) using FEI Tecnai F30 Transmission Electron Microscope is used for revealing the finest details with better resolution.

5.3 Results and Discussion

5.3.1 Electroless coating

It is imperative that the synthesis of good composite powders needs to be efficient and cost effective as well as achieving the desired properties. The control of the microstructure of ceramic–metal composites is generally difficult to achieve by traditional techniques involving mechanical mixing of ceramic and metallic powders followed by hot pressing[78-79]. A small-scale homogeneity can be obtained using the sol-gel route[80-82]. However, the relatively high cost of some reactants and the difficulty to control the gel drying step are some of the drawbacks to this method. Electroless coating has been chosen as it is being perceived as an efficient method by which Nickel can be uniformly reinforced in to the alumina matrix to increase the mechanical properties of the composite. The chemistry of the formation of the Nickel layer uniformly over the surface of alumina is shown in Figure 26. $SnCl_2$ hydrolyzes into Sn(OH)Cl and be absorbed on the Al_2O_3 particles followed by Pd^{2+} reaction with Sn(OH)Cl to form Pd nuclei on the Al_2O_3 surfaces. This renders the alumina surface suitable for Nickel coating. The electroless bath containing Sodium hypophosphite and ammonium hydroxide react together to leave electrons which sufficient to reduce Nickel chloride to Nickel. The Nickel, thus formed gets coated on to the sensitized and activated alumina particles. The thickness of the electroless coated Ni layer over alumina particles could be revealed using Focused Ion Beam. XPS analysis on the layer presented in Figure 27 revealed peaks at binding energy values of 852.8 eV and 870.7 eV. These

peaks were confirmed to be of $2p_{3/2}$ and $2p_{1/2}$ of metallic Nickel respectively[83]. The binding energy shift due to the charging was removed by referencing the adventitious C (1s) binding energy value[84] at 284.6 eV.

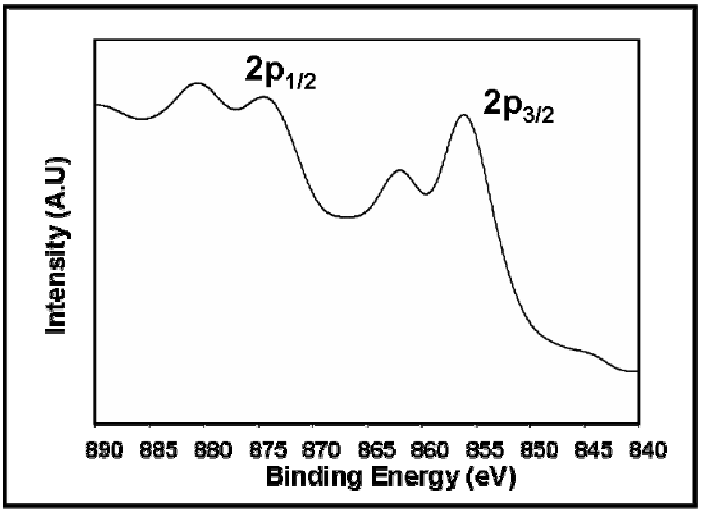

Figure 27 XPS Spectra on Ni coating confirming metallic Ni peaks

5.3.2 Concept of Wettability

The rationale behind the formation of spherical droplets of Nickel can be understood from the point of view of wettability. As the Nickel particles attain the liquid state, instead of complete wetting alumina, it makes the point contact due to surface tension constraints, as shown in Figure 28 and Figure 29. Contact angle is decided by the energies of the solid-liquid, liquid-vapor and solid-vapor interfaces involved in wetting process. The contact angle is high in case of pure metals because of the high solid-liquid interfacial energy than the solid vapor interfacial energy. It is being reported[85] that the solid-liquid interfacial energy for Ni-Alumina couple is 1.86 J/m^2

while the solid-vapor interfacial energy is calculated as[86] 0.9 J/m^2. Sessile drop test conducted to measure the Wettability angle revealed the contact angle to be at 108^0. If the wettability is less, the area immediately near the droplet will have no or little amount of the droplet composition while farther away from the droplet composition will be appreciable. This is because of a combination of the so called "evaporation-deposition" processes occurring during the process

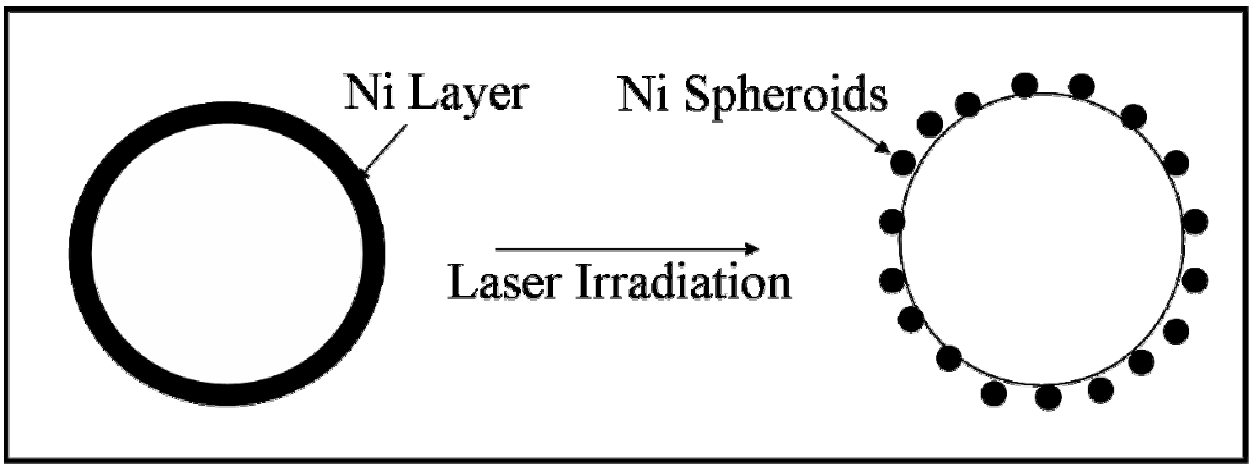

Figure 28 Schematic Illustration involving transformation of Ni layer in to spheroids

[87]. The bonding of Nickel on the Alumina surface can be comprehended based on interfacial strength. At the interface, a polycrystalline surface is prone to have more grain boundaries as a result of which roughness is high. Due to this high roughness factor, the accommodation factor for a Nickel atom to get bonded with the alumina surface is more compared to that of a smooth interface.

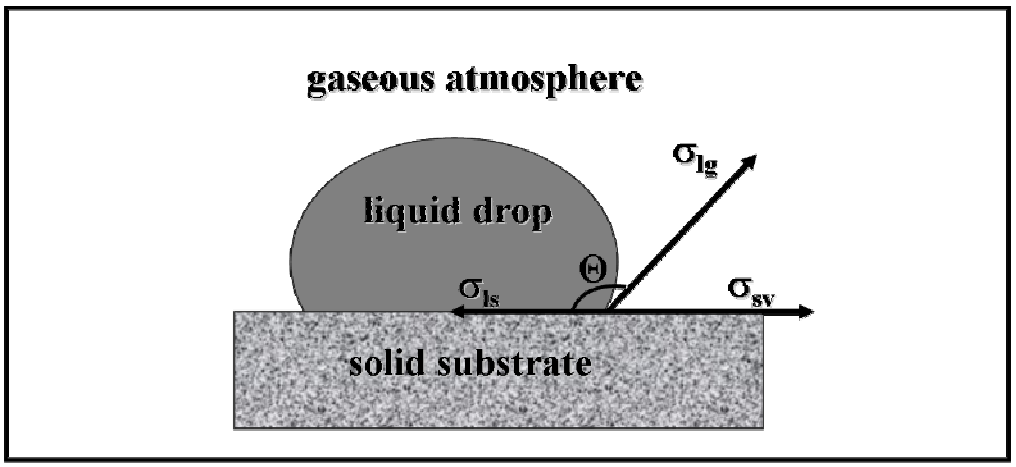

Figure 29 Nickel prefers to make a point contact in Alumina rather than completely wetting.

Recent results show the presence of interfacial cracks generated as a result of poor bonding of Nickel with a single crystal alumina surface compared to a polycrystalline alumina surface, as given in Table 9.

Table 9 Contact angle measurements of metallic Nickel on Alumina

Substrate	Dimension, mm	Contact angle, Deg	Roughness, nm		
			R_a	R_q	R_t
Al_2O_3 PC (99.99%)	20 x 5	108	100	140	1190
Al_2O_3 SC (99.99%)	20 x 1	94	2	2.5	8

5.3.3 Validation of Self-Affine Roughness Model

Saiz et.al[85] determined the contact angle for Ni-Alumina system to be 130^0 with the surface energy values of $\gamma_{lv}, \gamma_{sl}, \gamma_{sv}$ plugging these values in to the young's equation. But the experimental values measured were found to be 108^0 in this study. Considering the self-affine roughness

model[88], the apparent contact angle will be different from the contact angle θ calculated using the young's equation[85],

$$\text{Cos}\,\Theta = \frac{(\gamma_{sv} - \gamma_{sl})}{\gamma_{lv}} \quad \text{——————} \quad (1)$$

This can be explained based on the roughness of the surface of the sample. Surface roughness is described as a sine wave with an rms amplitude Δ and in plane surface roughness correlation length ξ which is the average distance between the consecutive hills or valleys on the surface. Rough surfaces are usually a combination of circular grooves and radial grooves. The apparent angle is calculated based on the root mean square value of apparent contact angles Θ_g and Θ_w which are contributions from the radial and circular grooves respectively. If the amount of circular grooves is much higher than the radial grooves at the point of contact angle measurement, apparent contact angle Θ_w will be dominating[87].

$$\Theta_w \cong Cos^{-1}\{[1 + (1/2)\rho - (3/8)\rho^2]\cos\Theta\} \quad \text{——————} \quad (2)$$

where ρ is the root mean square local slope which can be approximated to $\Delta/\ \xi^H$. H is the roughness exponent. Higher the value of H, the higher is the roughness of the surface. For theoretical values of Θ which was 130^0, solving the above quadratic equation gives the value of 110^0 for the apparent contact angle which agrees closely with the experimental values. Values assumed for Δ (amplitude) , ξ (distance between two consecutive hills or valleys) , H (Hardness exponent) are taken as 23 nm, 60 nm and 0.6 respectively because alumina being a polycrystalline and the amount of grain boundaries present are much higher compared to a single crystalline material.

As it is evident from the table, the roughness factor plays a dominant role in Wettability. A cross section of the sessile drop sample with nickel droplet on top of alumina substrate is shown in

Figure 30

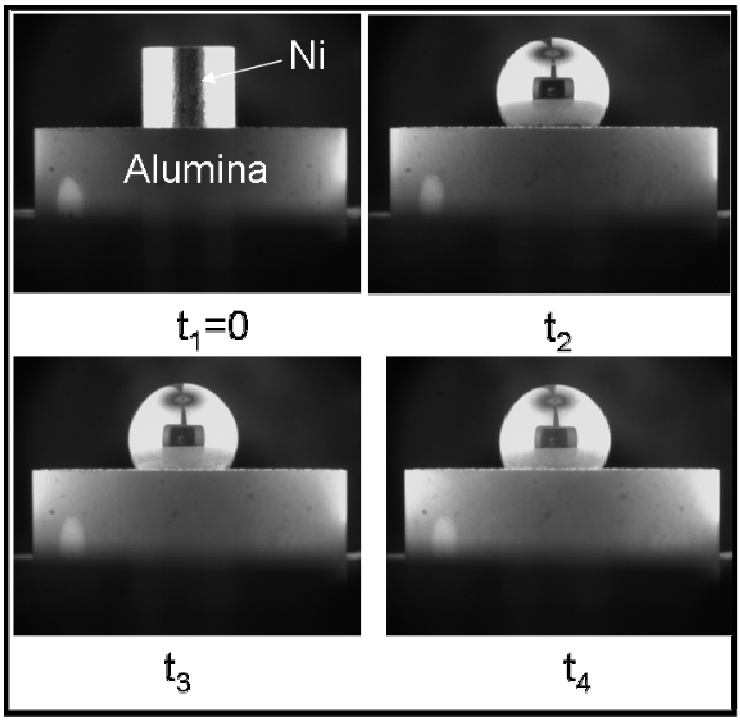

Figure 30 Illustration of Wettability of Nickel on Alumina as a function of time. $t_1<t_2<t_3<t_4$

EDS spectra from the area just near the Ni droplet showed that there is no appreciable Ni concentration. This experimentally proves that wettability of nickel is low[87] .Such uniformly dispersed Nickel particles are expected to inhibit crack propagation in the brittle alumina matrix.

5.3.4 Laser Processing

Thermal energy given to the sample during laser processing depends on the power of the laser used. The interaction time in the first regime can be estimated as the time for which the laser beam illuminates one point during fast scanning (~ 12 ms). The absorption coefficient for

metallic surfaces and Nd:YAG laser wavelength increases with surface roughness, temperature and with an angle of incidence of the beam[89]. Typical values lie in an interval 25-35 % for room temperature, polished surfaces and perpendicular beam. Absorption takes place in a surface layer approximately 10^{-4} mm in thickness.

At different power of the laser beam, the morphology of the Nickel showed variation which is shown in SEM micrograph in Figure 31 through 33. Due to the irradiation of laser beam, electroless Ni layer covering the surface of alumina melts instantaneously and due to surface tension gets converted to globules. The higher the amount of thermal energy, the more is the driving force for the globules to get coarsened. The fact that each alumina particle has its own characteristic size of Ni globules suggests that there is not enough thermal contact between individual particles to equilibrate different surface temperatures. The sizes of the Ni globules observed by SEM ranges between 0.1 and 0.5 μm. Some of the alumina particle surfaces irradiated with high laser power is free of Ni globules, but large Ni globules (~5 μm) are observed in their neighborhoods.

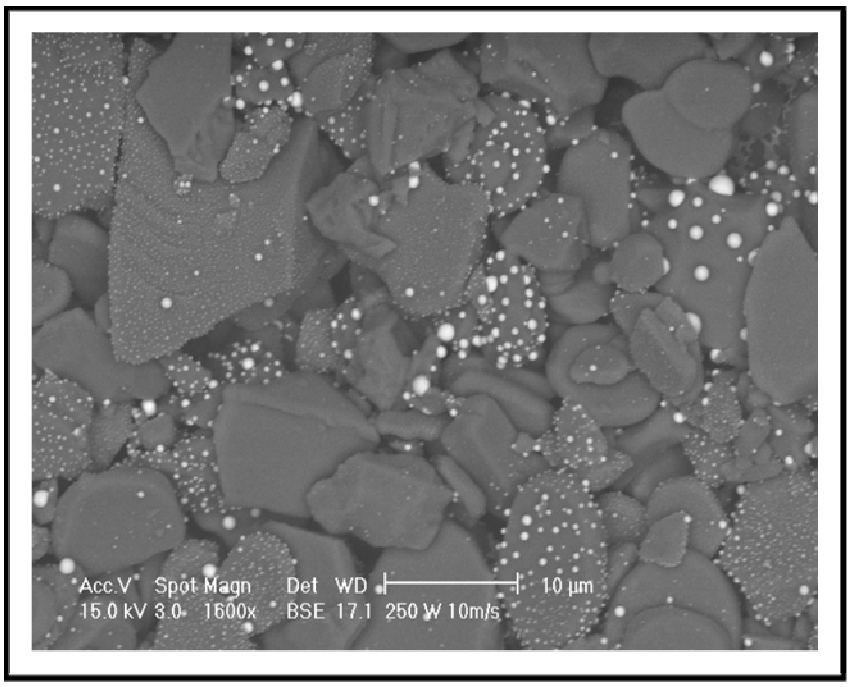

Figure 31 Ni Particle size at a laser power of 250 W

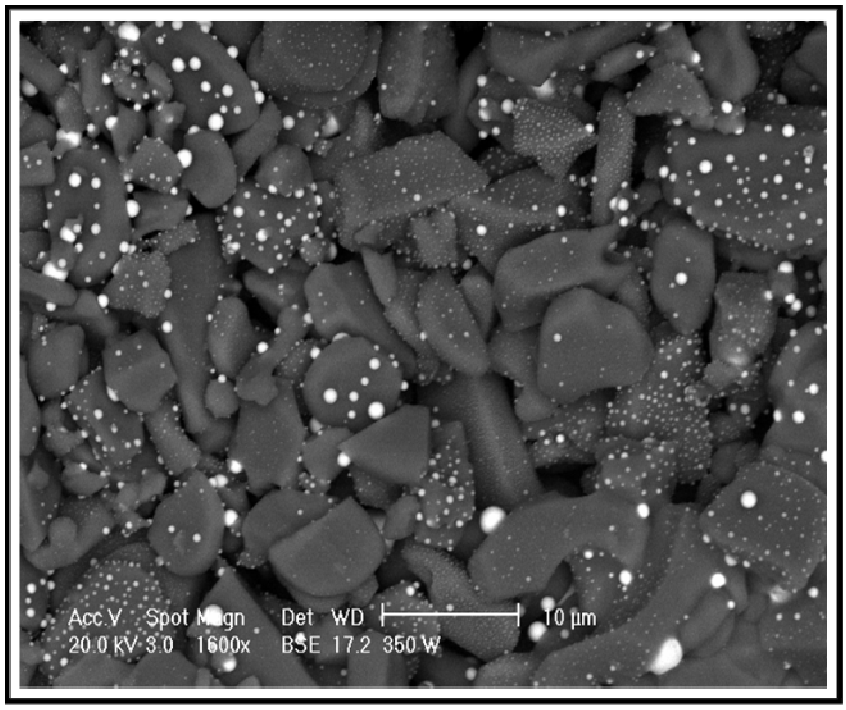

Figure 32 Ni Particle coarsens due to increase in the power of the laser beam to 350W.

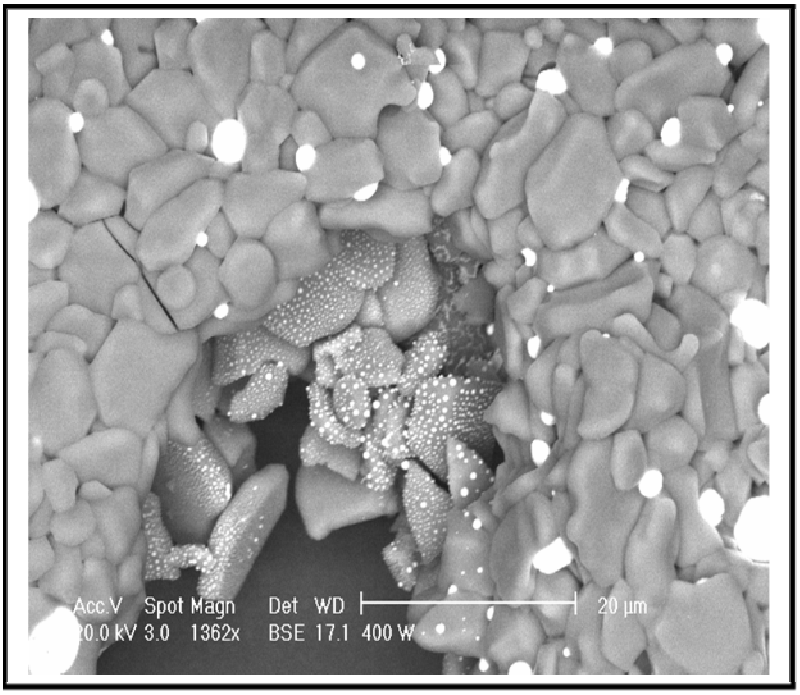

Figure 33 Ni Particle further coarsens at a higher laser power of 400 W

Laser processing is actually advantageous from the fact that power of laser beam can be manipulated to get to the suitable microstructure. The presence of Ni particles as small as 5 nm was revealed in HRTEM analysis of high temperature processed Ni-coated alumina. Lattice fringes of Ni nanoparticles could be resolved in the HRTEM study as shown in Figure 34. The corresponding EDS spectrum (Figure 34b) analyzed from the selected area confirms the presence of Ni, Al and Oxygen. Other elements that are detected are either from the specimen grid or the Si wafer used for specimen preparation. However, consolidation of Ni/alumina to bulk composite fabrication was not achieved, since the whole laser beam energy is absorbed in a thin Ni layer and a fast transformation of Ni layer in to spheroids occurred. Therefore, plasma processing route was chosen to manufacture a free form bulk nanocomposite part.

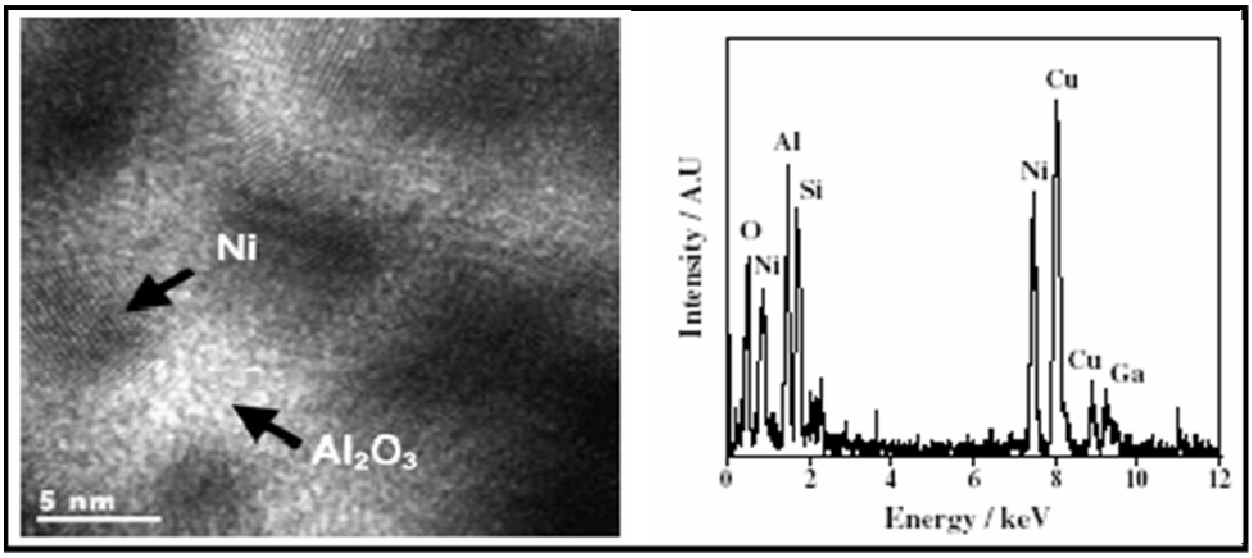

Figure 34 (a) HRTEM Picture revealing the nanostructure retention of Ni-Alumina nanocomposite. (b) EDS peaks confirming the presence of Ni in Alumina matrix.

5.3.5 Plasma Processing

The rationale and science behind using plasma spray as a free form manufacturing technique and aluminum mandrel as a substrate for development of Ni-Alumina bulk part has been discussed in this section.

Plasma-Particle Interaction: Plasma-particle interaction results in the formation of atoms in excited state, ground state, ions, and photons in the plasma plume. As a result of these atomic dissociation and recombination processes, particle that is sprayed is taken to a partial molten state for a brief period of time till it splats on to the substrate. Time of flight, the time required for the particle to reside in the flame depends on material parameters such as the Latent Heat of

fusion, Melting Temperature, particle size. The relation to determine residence time can be given as[90]

$$t_{i-f} = \frac{\rho C_p \nu \left(\ln\left(T_i - T_s\right) - \ln\left(T_m - T_s\right)\right)}{h.As} \quad \text{——— (3)}$$

where ρ , Cp , υ, Ti , Tm, h, As are the density, specific heat capacity, volume , initial temperature, temperature of the plasma plume , melting point, heat transfer coefficient, surface area of the particle and Ts is the plasma plume temperature. The knowledge of residence time is essential before spraying because too much of over heat may lead to evaporation losses. Also, higher the amount of superheating , the particles are subjected to rapid cooling as it impinges on the substrate as a result of which shrinkage stresses will be more . This might lead to cracking of the bulk part. A calculation (Table III) for residence time t_f for different particle size Ni-Alumina system has been tabled. It can be inferred that smaller particles need less residence time which can controlled with the parameters mentioned above. To avoid evaporation and to ensure only surface melting, appropriate gas flow combinations can be selected to obtain the residence time of interest. The residence time calculated was 0.2 microseconds for a 50 nm particle to pass through.

Table 10 Particle radius as a function of dwell time

Particle Radius	Dwell Time (Sec)
50 μm	4.01 x 10-^{04}
30 μm	1.12 x 10^{-04}
20 μm	7.44 x 10^{-05}
1 μm	3.72 x 10^{-06}
50 nm	1.86 x 10^{-07}

Coating Vs Free forms – Engineering Aspects: The section describes the science behind the fabrication of a free form part, which is different from coating. Aluminum and Copper being good conductors of heat are ideal candidate materials for being used as a substrate for material deposition. Besides, they can be fabricated to any desired shape as a result of their malleability and the high Coefficient of Thermal Expansion facilitates easy removal of the sprayed deposit. Aluminum substrate can facilitate easy removal by shrinking more, compared to steel or copper. Cooling and solidification of most materials is accompanied by contraction or shrinkage. As particles strike they rapidly cool and solidify. This generates a tensile stress within the particle and a compressive stress within the surface of the substrate. As the coating builds up, the tensile stresses developed in the deposit also increases. The residual stress developed during the air plasma spray process significantly influences the integrity of the deposit. Stresses developed during spraying can be classified in to two parts, viz quenching stresses and cooling stresses. Quenching stresses are stresses that develop as the splat formation takes place due to particle impingement on the substrate. The quantification of quenching stresses can be done using [91-92]

$$\sigma_q = \frac{E_s t_s (t_s + \beta^{\frac{5}{4}}.\Delta t_d)}{6.\Delta R.\Delta t_d} \quad \text{and} \quad \beta = \frac{E_d}{E_s} \qquad (4)$$

where E is the elastic modulii of the substrate and the deposit indicated by subscripts s and d respectively. Δt is the thickness of the deposit and ΔR is the change in the radius of curvature of the coating. The plots as shown in Figure 35 depict that different materials will develop different quenching stresses as the spray is going on. Based on the thickness of the deposit achieved the quenching stresses will vary. Among various spray materials for which quenching stresses have been calculated (Figure 35). The histogram shown for alumina and nickel particles with deposit

thickness of 0.015mm (15 microns) is of interest to this study. Cooling stresses are stresses that the deposit produces when the spraying is completes and the temperature of the part is plummeting to room temperature. It can be accounted for using an equation [93]

$$\sigma_c = \frac{E_d\left((\alpha_d - \alpha_s)(T_d - T_{RT})\right)}{[1 + 2(E_d.t_d / E_s t_s)]} \qquad (5)$$

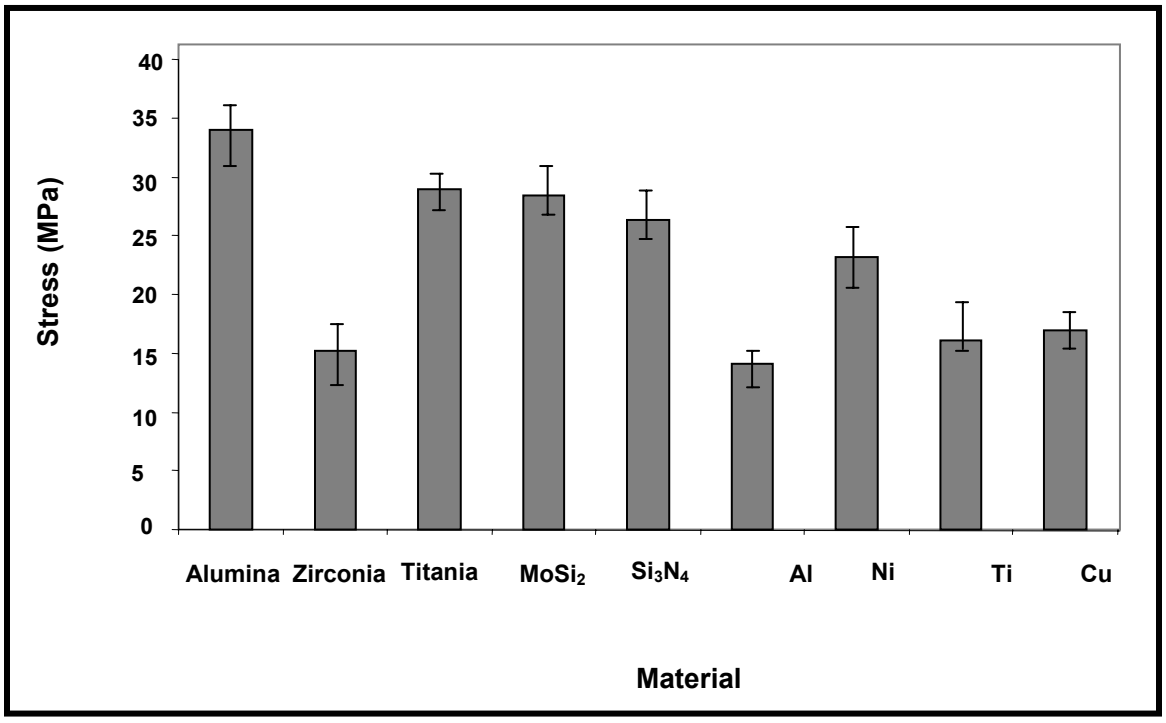

Figure 35 Quenching stresses developed during the spray of different particles

where E_d – Young's modulus of the deposit , T_d – Temperature of the deposit , T_{RT} – Room temperature of the sample after cooling , α_d – Coefficient of Thermal Expansion of the deposition , α_s – Coefficient of Thermal expansion of the substrate , Es- Young's modulus of the substrate , t_s – thickness of the substrate and t_d – thickness of the deposition .

Figure 36 depicts the calculated cooling stresses for different materials for two different substrates Copper and Aluminum. The total amount of stresses developed in the deposit is a combination of both quenching and cooling stresses. Quenching stresses which are tensile in nature keeps increasing with thickness build-up. The thermal stresses (cooling stresses) will be compressive when $\alpha_d < \alpha_s$. Selection of aluminum mandrel for Ni-alumina is justified based on the calculation that the

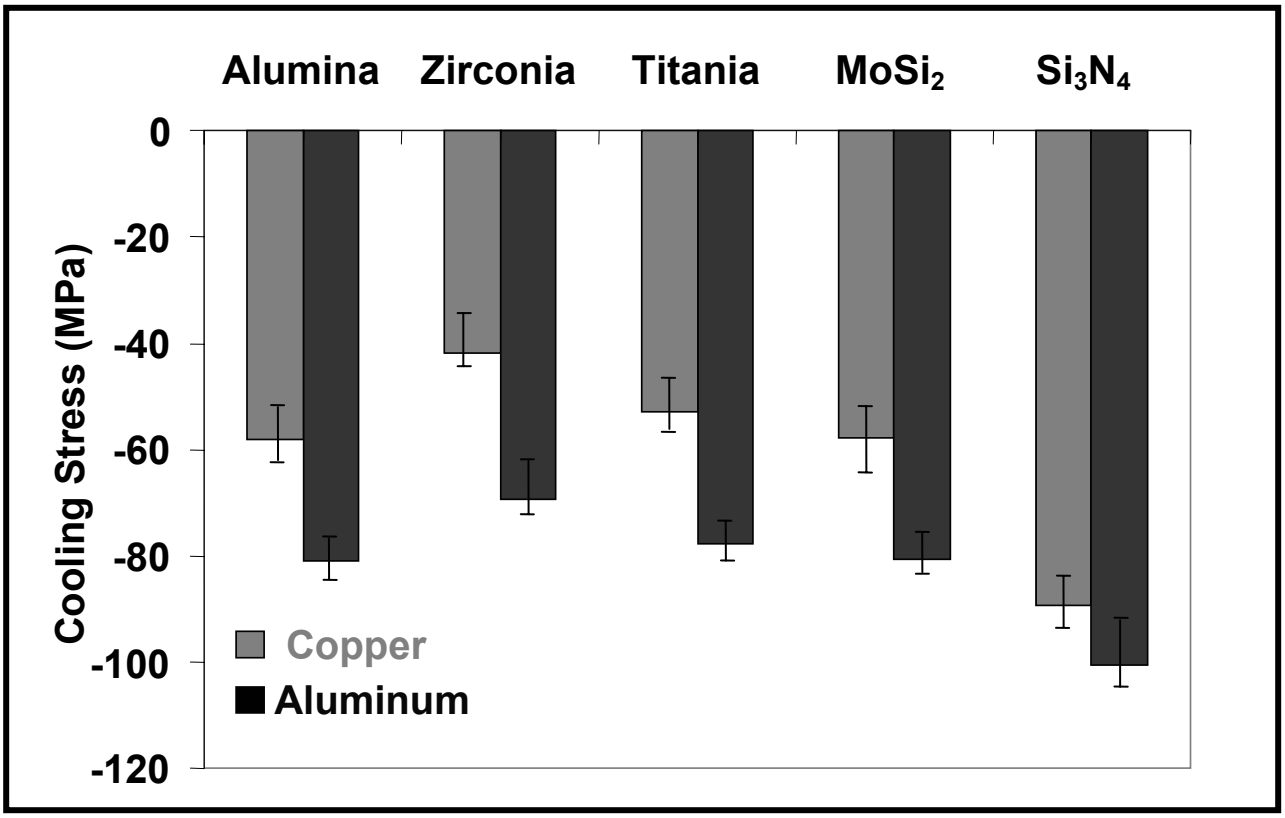

Figure 36 Cooling stresses developed in the deposit for Cu and Al substrates

cooling stresses are compressive in nature. It will facilitate the removal of spray deposit from the substrate. This will eventually lead to free form fabrication of deposits.

Material Characterization: The trial for spraying nano ceramic particles through plasma flame has been successful. The Ni-Alumina cylindrical bulk nanocomposite without any surface defects was manufactured using plasma spray technique (Figure 37). Microstructure Evaluation using SEM and other characterization tools such as XRD and HRTEM is being discussed at length.

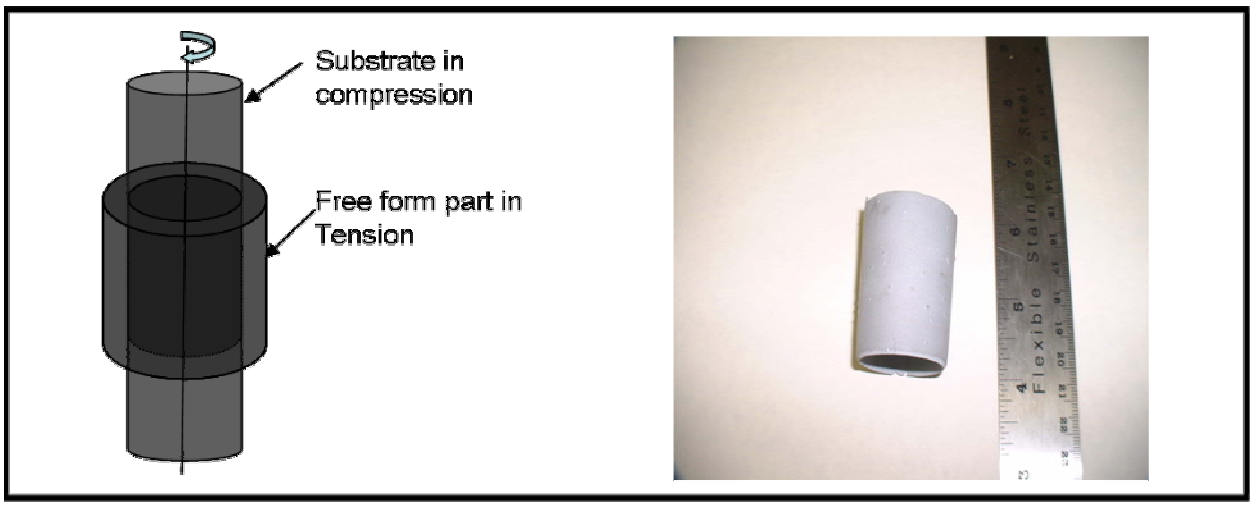

Figure 37 (a) The mandrel is subjected to compressive stresses while the sprayed part acquires tensile stress as the spray continues, (b) A 1.2 ” OD X 1” ID X 1.5” Length was produced with full integrity.

Cross-Section Microscopy: In an effort to study the porosity distribution across the thickness, scanning electron microstructure of the internal, center and outside of the thickness (Figure 38) has been analyzed. The section is 96-98 % dense and does not show any significant cracks or porosity. It also reveals the formation of splats due to higher velocity with which the melted particles impinges on to the substrate. There was no evidence of interconnected pores which could have been detrimental to the integrity of the part. Also, the porosity distribution is more in case of internal thickness and less in outside thickness. This can be explained from the fact that particles temperature gets reduced drastically during the initial stages of spray as a result of

which shrinkage is more, while the particles at the outside thickness has to undergo relatively less temperature difference. SEM micrographs of the cross section revealed a clear demarcation between the formation of folds and the formation of porosity. The porosities are revealed as dark regions compared to less intense folds. Fold formation happens due to the inability of particles to fully splat on top of the existing splat.

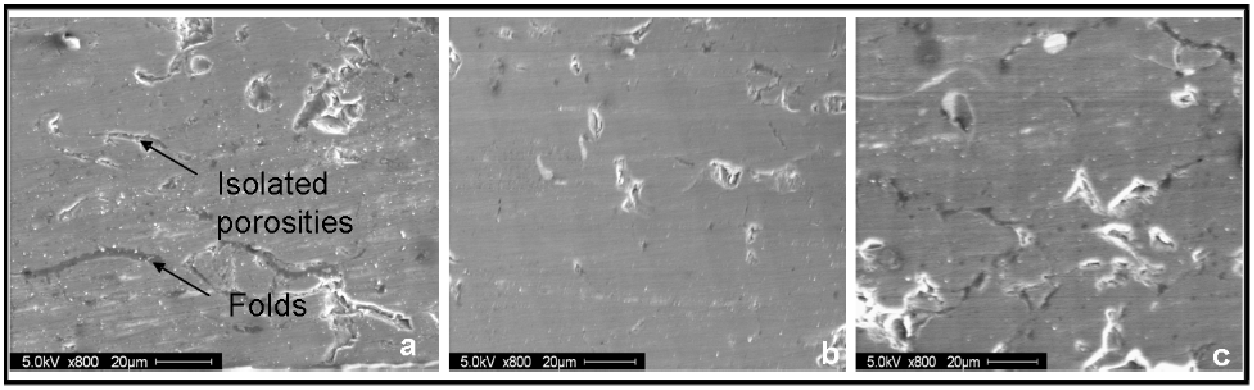

Figure 38 Cross sectional micrographs indicating the extent of porosity formation at the a) external, (b) middle and c) internal portions of the bulk nanocomposite.

Phase transformation: It is being observed that the alumina matrix undergone phase transformation from alpha to gamma structure. The alpha to gamma transition depends on the ratio of the gun power to the primary gas flow in Standard Cubic Feet per Hour (SCFH). It is mentioned elsewhere[94] that if the parent phase is α-alumina, based on this ratio mentioned above the product phase might be a combination of more α-alumina and less γ alumina if the ratio is less than or equal to 240 or a combination of more γ alumina and less α-alumina if the ratio is more than or equal to 310. The density and hardness values achieved [94] with the above ratios show significant differences with the former showing less hardness and density than the latter. The phase transformation achieved in our present case had more γ alumina. The spray parameters were manipulated to keep the ratio above 310 to make sure that dense and hard

nanostructures were obtained. The diffractograms before and after plasma spraying is shown in Figure 39. X-Ray diffraction spectrums from the plasma spray deposition and powder mixture prior to the spraying are compared. Both the diffractograms reveal the presence of FCC Ni and Alumina. The difference between the diffractograms is that of the peak broadening. During the spray, particles literally gets quenched from their melting temperatures towards the substrate

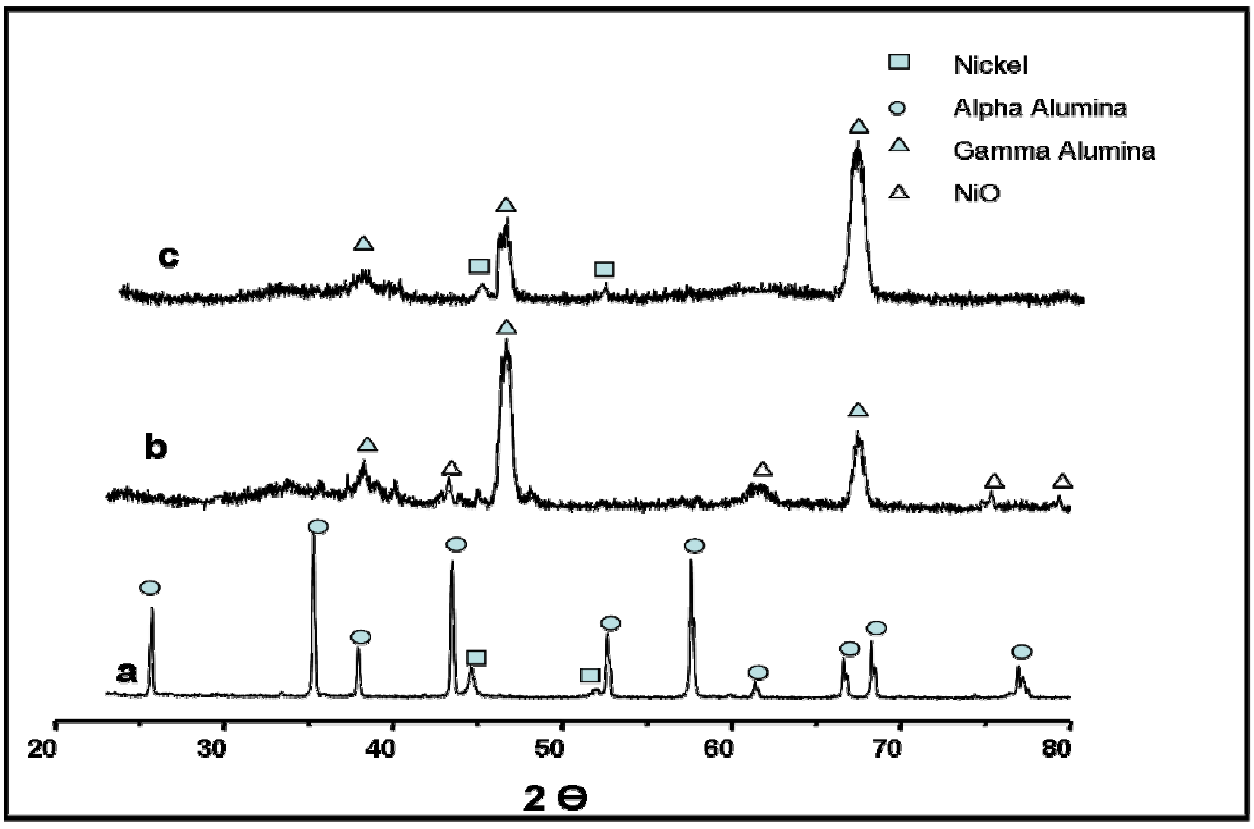

Figure 39 Phase transformations associated with plasma spray of Ni-Al_2O_3 a) Feedstock powder b) plasma sprayed component c) Hydrogen Reduction

preheat temperature. Such large temperatures gradients are expected to impart residual stresses on the sprayed part. The stresses can be calculated based on the difference in "d" spacing of the particles prior to spraying and after spraying. From the modulus of elasticity values, the amount of residual stress can be calculated as follows[95].

$$E_{hkl}^{-1} = \frac{(C_{11}+C_{12})}{(C_{11}-C_{12})(C_{11}+2C_{12})} + \left(\frac{1}{C_{44}} - \frac{2}{(C_{11}-C_{12})}\right)(l^2m^2 + m^2n^2 + n^2l^2) \quad - \quad (6)$$

The compliance constants are C_{11} = 246.5 GPa, C_{12} = 147.3 GPa and C_{44} = 124.7 GPa. . The calculated residual stress values are presented in Table 11.

Table 11 Residual Stress measurements using X-Ray Diffraction Techniques

Composition	Hkl	2Θ*	2Θ (JCPDS)	d* (Å)	d, Å (JCPDS)	Strain (%)	E (GPa)	Stress (MPa)
NiO	200	43.26	43.29	2.09	2.09	0.066	136	90
NiO	111	37.25	37.28	2.41	2.41	0.078	304	236
NiO	220	62.89	62.92	1.48	1.48	0.043	232	99
γ- Alumina	440	67	67.032	1.40	1.39	0.042	408	172

* - Measured values.

Since the process has been carried out in atmospheric air, Ni has the propensity to get converted to its surface oxide. Gibbs free energy of formation of Nickel oxide up to melting point of Nickel is negative. Although Gibbs free energy curve for formation of Nickel oxide is sloped up with temperature, the partial pressure of oxygen at NTP is much higher for the reaction to proceed forward and form NiO. APS process carried out at dehumidified air will have an oxygen partial pressure of 0.2 atm which is more than sufficient for the NiO formation to occur. Moreover, if the stand off distance is more, Nickel in its molten state picks up more oxygen from the atmosphere than it would have if it were in solid state. By reducing the stand off distance the amount of formation of Nickel oxide can be reduced but can not be totally eliminated. XRD peaks confirmed the formation of NiO. An effort has been made to bring NiO back to its metallic state. The plasma spray formed nanocomposite was reduced in an atmosphere of Hydrogen at 1000^0 C for 1 hour.

High Resolution Transmission Electron Microscopy: Alumina grain boundaries being high energy regions, there is more probability of the presence of Nickel along the grain boundaries. In order to determine the location of Nickel, EDS has been performed along the grain boundaries to select spots for imaging of Nickel nano particles. In those spots where strong Nickel signal have been detected, STEM imaging has been done to determine the morphology and the size of the Nickel particles. Spherical Ni particles with 30 nm size have been imaged and are shown in Figure 40. Another evidence of nanostructure retention of Nickel particle is the SAD pattern, which shows a spotty ring pattern as revealed in Figure 40(a) (inset). This pattern is a result of extremely fine grains. The possible explanations of the nano structure retention in Ni-Alumina nanocomposite could be the lack of time permitted for the coarsening of Nickel particles

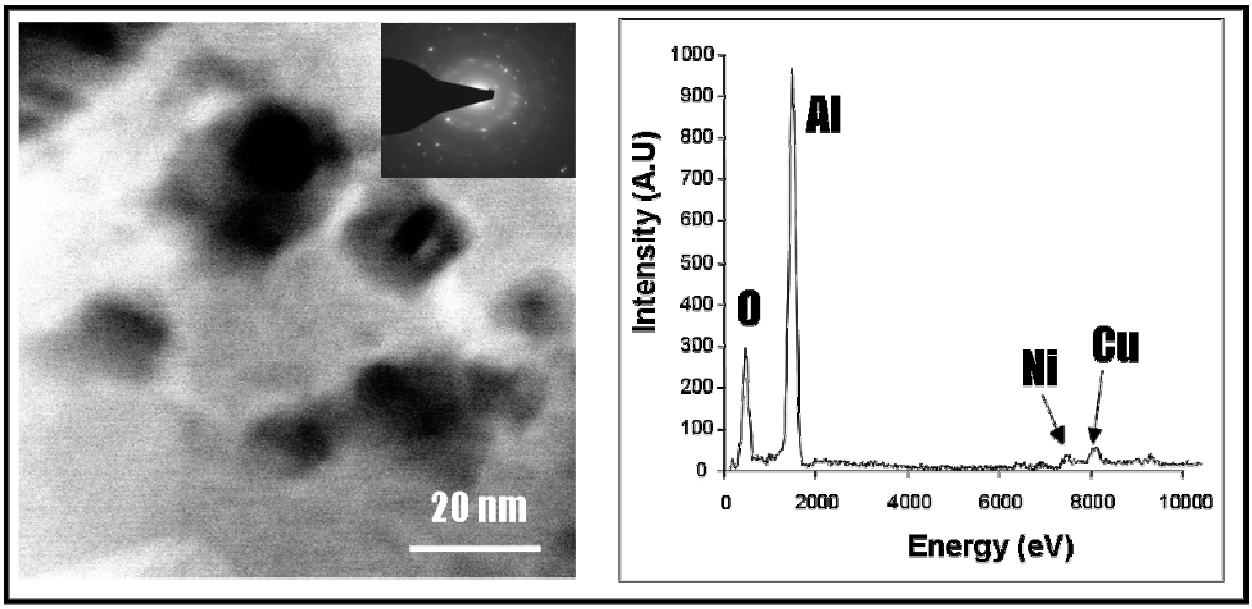

Figure 40 STEM pictures depicting nanostructure retention of Nickel particles and the corresponding EDS spectrum confirming the presence of Nickel

traversing through the high temperature zone (plasma flame). On the other hand during conventional sintering, a significant time is spent in the temperature range where the coarsening

effect is appreciable[76]. Besides, in the nanostructures, surface melting is preferred in the fast translation thus keeping the core intact. From the TEM pictures of plasma sprayed Nickel-Alumina, it is envisioned that plasma processing is considered to be a potential tool to fabricate free form (e.g., cylindrical) bulk composites with nanostructure retention and improved mechanical properties.

Mechanical Properties: Nickel plays a dominant role in increasing the strength of the ceramic matrix. The presence of cracks in ceramics makes them more brittle compared to metals. At the tip of the crack, as shown in Figure 41 there is an enormous amount of stress concentration developed as a result of which the cracks tend to propagate easily . The surface energy required

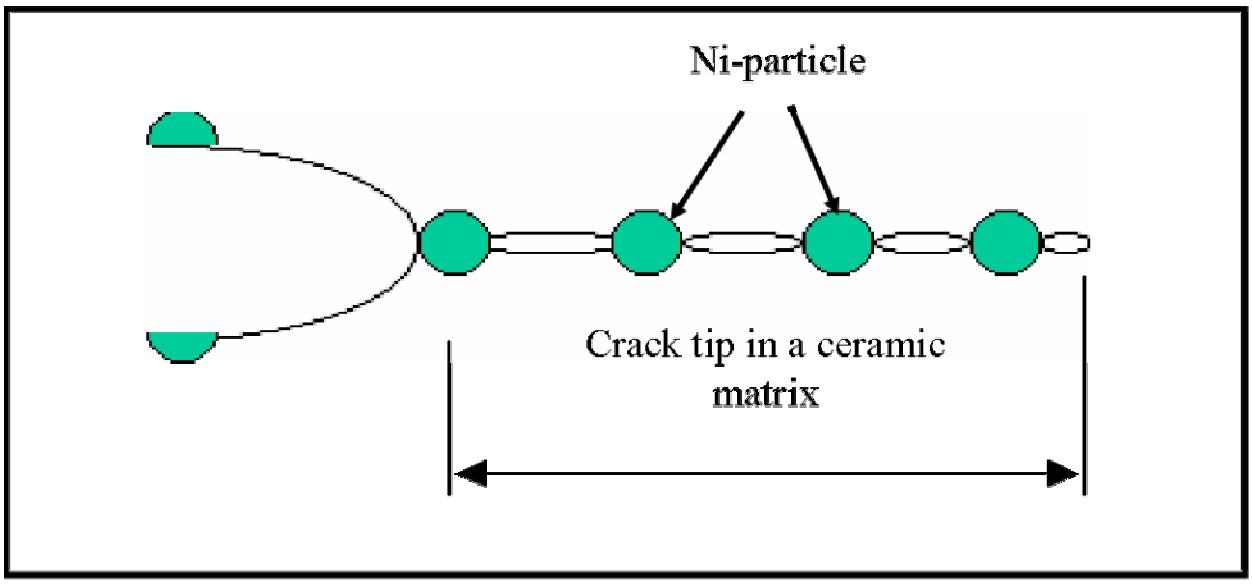

Figure 41 Nickel particles blunts the crack and arrest crack propagation and improves the fracture toughness

to propagate the crack is more than compensated by the release of the elastic strain energy. The presence of Nickel spheroids dispersed uniformly throughout the matrix blunts the crack, thereby making it more difficult to propagate as shown in Figure 41. Nickel particles which are highly

plastic in nature aids in crack blunting and improvement of fracture toughness of the nanocomposite. Lieberthal et.al[72] proposed a model in which a crack propagating along the alumina grain boundaries are deflected along around the Ni particle located in grain boundaries which aid in improving the fracture toughness of the ceramic nanocomposite.

The hardness and fracture toughness of the Ni-Alumina plasma sprayed sample that could be achieved with the given set of plasma spray parameters were measured to be 1025 HV and ~ 5 $MPa.m^{1/2}$. The hardness values achieved were found to be better than that achieved for the monolithic alumina developed using plasma spray (940 ± 20 HV)[96]. The marked increase in the fracture toughness compared to other processing techniques can be attributed to the crack blunting capability of ductile Nickel. It should be noted that Ni-Alumina nanocomposites made through techniques such as Hot press sintering[68] reported a fracture toughness of ~ 3.5 $MPa.m^{1/2}$ In other words, the increase in fracture toughness was approximately 40%.

5.4 Conclusions

Electroless Nickel coated alumina particles have been successfully used to manufacture a free-form bulk nanocomposite with improved hardness and fracture toughness. Wettability study of Nickel on polycrystalline Alumina revealed the contact angle which validated the self affine roughness model being used to calculate the apparent contact angle. Laser processing had shortcomings from the point of view of time and the high laser required to consolidate the powders to bulk form, especially in the case metal/ceramic matrix. For plasma processing, substrate material selection is important based on the material composition to be sprayed. High fracture toughness can be attributed to the nanostructured Nickel which arrests the crack

propagation. Thus, plasma spray processing is an effective technique to make free form bulk nanostructures.

CHAPTER 6 W-HfC NANOCOMPOSITE

6.1 Introduction

Nanostructured materials are widely researched for their mechanical, thermal, optical and electrical properties and variety of other applications. Mechanical properties such as tensile strength, hardness, fracture toughness and wear resistance are quite important for structural applications. Fabrication methods such as sol–gel processing, gas phase condensation, high-energy mechanical milling, chemical precipitation, plasma synthesis, etc., are used to synthesize nano particles but could not be used to consolidate them to an application pertaining to daily life. Consolidation of nanoparticles into near net shape structures and/or bulk engineering components with nano-sized grains is difficult because of the low compressibility, high inter-particle friction and tendency to particle growth during consolidation. Different consolidation processes, viz. hot Isostatic pressing, transformation assisted consolidation, microwave sintering, equal channel angular pressing, gel casting, sol infiltration, cold die pressing, etc., are being adopted to fabricate bulk nanocrystalline structures[97,98]. Rapid solidification techniques viz. direct laser deposition, spray forming, melt infiltration, spark plasma sintering, plasma spray technique that have the potential of arresting the grain growth efficiently, have demonstrated significant promise in achieving nanostructure in bulk components[99,100]. In the present work, an effort has been made to fabricate HfC reinforced Tungsten metal matrix nanocomposite as a proof of concept for making bulk component prototypes. Because of its high melting point, tungsten (W) metal matrix composites have been applied, most particularly, for their favorable thermo-mechanical attributes. One noticeable drawback in the W matrix, however, is a reduction in material strength at high temperature regime. The strength of W decreases up to 80% at 1000 ˚C compared to that at room temperature[101]. Some composites, mainly oxides and carbides, have

been reinforced with the tungsten matrix in successful attempts to further strengthen the thermal resilience of the resulting composite[102,103] . HfC has the highest thermodynamic stability and melting point and has been used especially for the applications in thermal shielding wear resistant environments[104-106]. In addition, due to its interstitial carbide bonding structure, HfC shares physical properties of ceramics and the electronic properties of metals forming primarily ordered non-stoichiometric phases[106]. An extensive comparative high-temperature strength study conducted by Raffo and Klopp (1963) determined that small additions of hafnium (amongst tantalum, niobium, rhenium, and carbon) in Tungsten arc-melted alloys produced a dramatic increase in high temperature tensile strength[107].

Through processes that will be mentioned, the retention of nanostructures will be explored and the mechanical properties of the reinforced bulk component will be obtained through indentation measurements. The focus of this research has explored and characterized multiple combinations and attributable properties of a vacuum plasma formed tungsten alloy that has been reinforced with a homogenous dispersion of nanoscale hafnium carbide for the fabrication of bulk nanocomposites.

6.2. Experimental procedure

6.2.1 Materials

The starting powders for use in the plasma forming of the bulk component were a mixture of tungsten based powder (1.3 μm average particle diameters) with a reinforcement of hafnium carbide nanoparticles of the order of 30 nm. The first sample created for experimentation was 1.3 μm tungsten without any HfC particulate reinforcement (spray dried), the second and third sample is a nanocomposite with the inclusion of 1.3 wt% hafnium carbide nanoparticles mixed

with 1.3 μm tungsten matrix. The difference between the second and third sample is that sample 2 is blended while sample 3 is spray dried before thermal spray. In order to improve the density of sprayed bulk components after thermal spray, both samples 2 and 3 has been subjected to Hot Isostatic Pressing (HIP) at 1800^0C at a pressure of 205 MPa for 4 hours. Spray drying[108] has been carried out using a Niro Mobile Minor spray drier (Niro A/S, Denmark). Processing details and composition of the samples created have been tabled (Table 12).

Table 12 Matrix of powder feedstock materials used during vacuum plasma spray forming and post-spray heat treatment specification.

Sample No.	Composition	Feedstock Agglomeration	Heat Treatment*
1	W (1.3 μm)	Spray-dried	N/A
2	W (13μm) + 1.3 wt% HfC	Blended	HIPed 4 hours 1800ºC and 205 MPa
3	W (1.3 μm) + 1.3 wt% HfC	Spray -dried	HIPed 4 hours 1800ºC and 205 MPa

*- Heat treatment done after plasma spray

6.2.2 Vacuum Plasma Spraying

A 25 mm (1 inch) diameter carbon mandrel was used as a suitable substrate for plasma spraying in vacuum. The powders were sprayed inside a cylindrical (diameter 1524 mm (60 inch)) water cooled vacuum chamber using a Sulzer Metco (Westbury, New York) 03C series plasma gun mounted on a robotic arm. The carbon mandrel could later be removed easily from the free form part due to the coefficient of thermal expansion difference between the substrate and the deposit. The plasma spraying parameters used to produce the spray formed components are listed in Table 13. To further densify the microstructure and reduce porosity, samples 2 and 3 were

further hot isostatically pressed at 1800ºC for 4 hours at a pressure of 205 MPa as listed in Table 12.

Table 13 Vacuum Plasma Spray parameters used for fabrication of bulk nanostructures.

Plasma Gases	Gun Power (kW)	Argon flow rate (s.l.m)	Hydrogen flow rate (s.l.m)	Chamber Pressure	Robot Motion Parameters
Ar- Primary H_2 - Secondary	80-105	117	21-26	75-150 Torr	Torch @ 5000 mm / min, part @ 40 rpm

6.2.3 SEM/FIB Analysis

A JEOL 4600 Scanning Electron Microscope (SEM) was used at a 5 kV acceleration voltage to obtain the images of the particles before and after spray drying and blending. A focused ion beam (FIB) equipment (Model FEI 200, FEI company, Hillsboro, Oregon) that has magnum column workstation with a gallium ion beam was used to produce the samples for the transmission electron microscopic investigation of the bulk components. The samples were thinned to 50 nm thickness for electron transparency. After thinning and cutting loose, the sample was removed using a micromanipulator and placed on a carbon TEM grid as described in the previous publication[109]. A field emission transmission electron microscope (TEM) (Model Tecnai F30, FEI company, Hillsboro, Oregon) was used for the investigation to ascertain the size and location of HfC particulates within the as-sprayed bulk components at an acceleration voltage of 300 keV and extraction voltage between 4.3 and 4.4 keV. The compositional analysis of HfC is tungsten matrix has been studied using a Secondary Ion Mass Spectrometer (Model ADEPT 1010, Physical Electronics Inc., Chanhassen, Minnesota). The equipment was operated with a 3 keV cesium beam at 60^0 off of the specimen normal.

6.2.4 Nano Indentation

A nanoindentation equipment (Model Nanotest 600, Micromaterials Limited, Wrexham, UK) was used to indent the specimens. A diamond Berkovich indenter (sharp indenter) with a loading rate of 4 mN/s and a maximum load of 200 mN was used to measure the hardness of the specimens using the analysis procedure proposed by Oliver and Pharr from the respective nanoindentation load (P)- depth (h) responses[110] . A 2.8 mm diameter diamond spherical indenter was used to indent the specimen to a maximum load of 1N at a loading rate of 50 mN/s to determine the elastic modulus following Alcala et al[111]. Instrumented nanoindentation has previously been used to assess mechanical properties, namely the elastic modulus, strain-hardening exponent, fracture toughness, creep rate, and Poisson's ratio of a material on a nano- or a bulk scale [112-113].

6.3 Results and Discussion

6.3.1 Powder Characteristics

Spherical powders have a lower inter-particle friction coefficient and thus its flow through the torch is facilitated for a given carrier gas flow[114]. Spray-drying was used as a mechanism of feedstock (starting powder material used for Vacuum Plasma Spray) preparation in this study because (1) the feedstock would clog the powder feeding assembly therefore halting production, (2) it is nearly impossible to entrain nanoscaled particles in the plasma stream without evaporation[115] , and (3) the spray-dried product was spherical, dense, and free-flowing. To enable adequate flow of particles during the plasma spray process, particular attention was paid to the feedstock powders' morphology, composition, size distribution, and density which play a dramatic role in the quality of the bulk part (or coating)[116-117]. The particle morphology before and after the spray process were investigated using SEM. The blended 1.3 μm W- 1.3 wt % HfC

powder exhibits a pasty surface structure (Figure 42), which may pose a problem in flowing through the plasma torch.

The spray dried agglomerated powder (Figure 43) exhibits a relatively larger agglomerate size via the attractive Vanderwaals and polymeric binding forces overcoming the smaller dispersive electrical forces that act on the particles in suspension and during the spray drying process[118] . As the smaller particles are bound in a spheroidal shape with relatively larger tungsten particles, this powder is more suitable in vacuum plasma forming system for bulk component

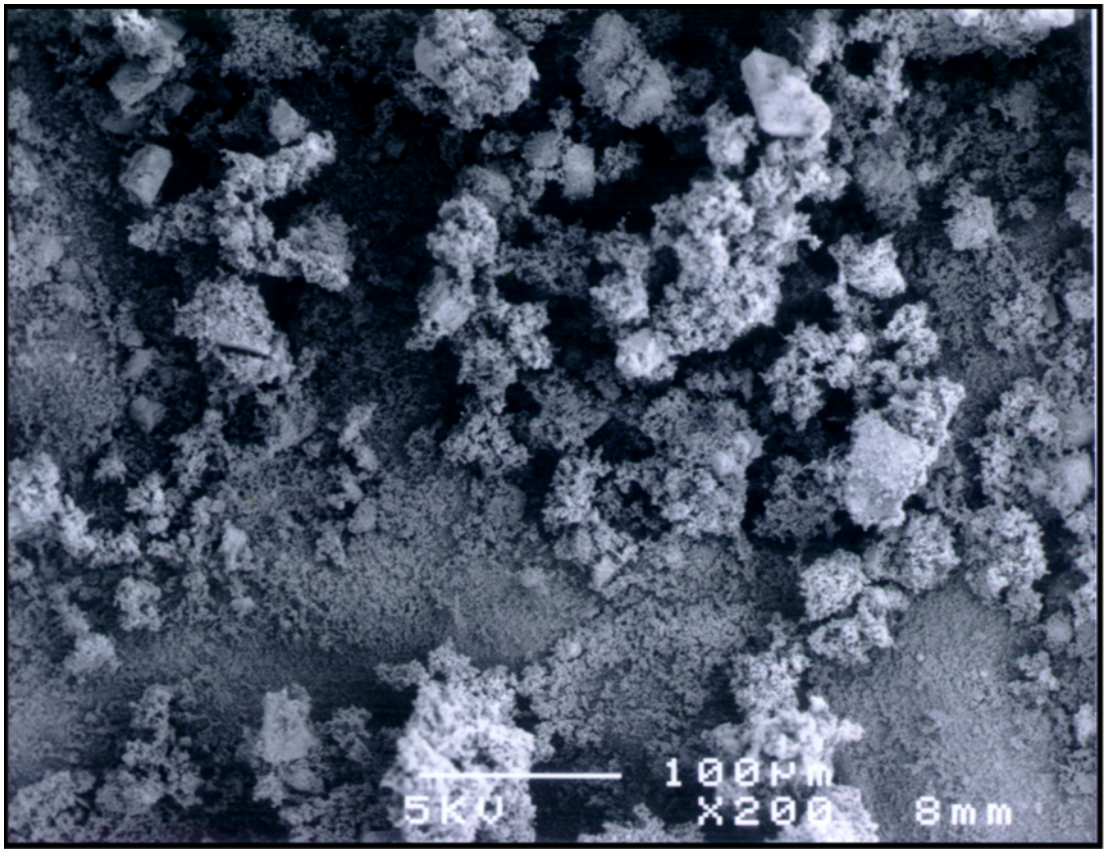

Figure 42 SEM imaging of blended W -1.3 wt% HfC nanoparticles used as a feedstock for vacuum plasma spray.

Manufacturing[119] The spheroidal shape of the feedstock powders will also provide for a higher packing density during the deposition process should the particles' flight in the flame be controlled and monitored[109] . It has also been shown that spray-dried powder has much higher deposition efficiency with a higher level of predictability based on plasma spraying parameters as opposed to ground or ball-milled micron sized powders[120] .

6.3.2 Stiffness of the Matrix

Elastic modulus for each of the samples is listed in Table 14. Sample 3 has a modulus close to double (223 GPa vs. 126 GPa) that of sample 1. It could be observed that the increase in elastic modulus of the nanocomposite is clearly due to the dispersed HfC additions with their high

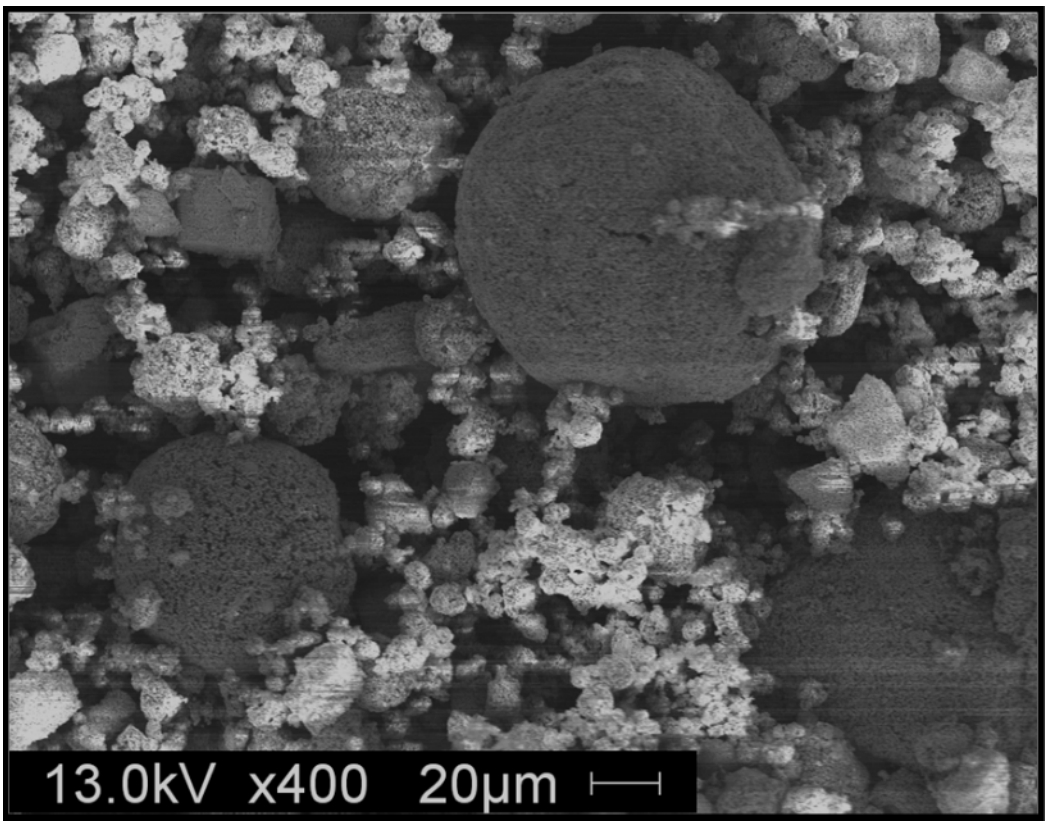

Figure 43 SEM image of spray dried W - 1.3 wt% HfC nanoparticles used as a feedstock for vacuum plasma spray.

Table 14 Mechanical properties of the bulk nano W-HfC composites.

Mechanical Properties	Sample 1	Sample 2	Sample 3
Elastic Modulus (GPa), Mean	126	153	223
Standard Deviation	73	34	85
Hardness (GPa), Mean	4.2	4.9	5.4
Standard Deviation	0.55	0.51	0.71

stiffness and the load bearing dynamics of the second phase particles in the matrix. The hardness data also reveals a trend by confirming that the presence of HfC particles strains the lattice and increases the hardness value of the nanocomposite. Hot isostatic pressing also could be a factor in the increase in the mean elastic modulus as shown in the difference between the measured moduli of samples due to densification of the microstructure and a decrease in sample porosity. Figure 44 shows several examples of spray formed large scale W-HfC nanocomponents produced by vacuum plasma spray forming for the first time in this class of nanocomposites.

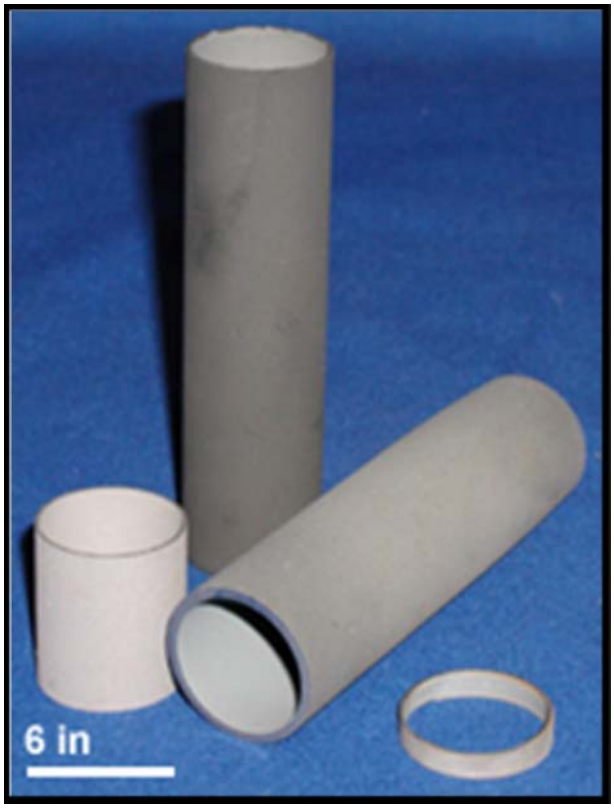

Figure 44 W-HfC bulk nanostructured components fabricated using the plasma spray parameters listed in Table 13.

6.3.3 Elastic modulus – Theoretical Calculations

The following theoretically measured estimation of elastic modulus for elastic behavior of the W-HfC nanocomposite was based on the models described by Lamé and later Eshelby[121,122]. The homogenous transformational inclusion strain of the constrained particulate, after separating the tensor into dilatational (Δ^T) and deviatoric ($\acute{\varepsilon}_{ij}^T$) components in terms of the bulk modulus *K* and the shear modulus *G*, is given in equation 1. When the matrix and reinforcements have different elastic constants, the misfit strain of the inclusion can be written in terms of K and G (Bulk modulus and Shear Modulus) as follows:

$$\in_{ij}{}^{T} = \frac{1}{3}\frac{(K_I - K_m)}{(K_m - K_I)A - K_m}\Delta^{T^*} + \frac{(K_m - K_I)}{3K_I}\Delta^{A} + \frac{(G_I - G_m)}{(G_m - G_I)B - G_m} \in_{ij}{}^{T^*} + \frac{(G_m - G_I)}{G_I} \in_{ij}{}^{A} \quad \text{--1}$$

For the Matrix of tungsten with the poisson ratio of ν= 0.28, the equation can be decimated to

$$\in_{ij}{}^{T} = \frac{(K_m - K_I)}{3K_I}\Delta^{A} + \frac{(G_m - G_I)}{G_I} \in_{ij}{}^{A} \text{ ---------- 2}$$

for axial loading with ν= 0.28 Δ^{T^*} *and* $\in_{ij}{}^{T^*} = 0$

$$\Delta^{A} = \frac{\sigma^{A}}{3E_M}, \in_{33}{}^{A} = \frac{8\sigma^{A}}{9E_M}, \in_{33}{}^{A} = \frac{\sigma^{A}}{E_M}$$

from which $\in_{3}{}^{T}$ can be calculated using equation 2 modified as

$$\in_{ij}{}^{T} = \frac{(K_m - K_I)}{3K_I}\frac{\sigma^{A}}{3E_M} + \frac{(G_m - G_I)}{G_I}\frac{8\sigma^{A}}{9E_M} \quad \text{--------- 3}$$

Where K and G are bulk modulus and shear modulus respectively and subscripts m and I are matrix and inclusion respectively. E_M is the elastic modulus of the matrix. (All units in GPa) The stiffness of the composite can thus be predicted using

$$E = \frac{\sigma^{A}}{\in_{3}{}^{A} + f \in_{3}{}^{T}} \text{ ---------- 4}$$

Substituting terms in 3 to equation 4 , the E-modulus can be approximated,

$$E = \frac{1}{0.0042 - f(2.909x10^{-4})} GPa \quad \text{----------5}$$

The elastic modulus thus calculated for 1.3 wt% HfC inclusion in Tungsten is 238 GPa which closely matches with the experimentally observed value of 223 GPa . It is to be noted that some of the HfC particles are lost during the flight in plasma torch . Since the HfC are encapsulated during the spray, there is considerably less loss of these nano particles as compared to blended samples. Blended samples have shown experimental E-modulus values similar to a pure tungsten sample and hence it is concluded that during the thermal spray, simply blending the nano particles with the tungsten matrix does not serve the purpose.

6.3.4 Microstructure and Strengthening Mechanism

Figure 45 reveals the partial recrystallization of the plasma spray splat morphology achieved through hot isostatic pressing. Hot isostatic pressing at this specific temperature and pressure did not show any noticeable signs of grain growth or unpinning of the nano HfC reinforcing structures as could be seen in the TEM pictures. TEM samples of 150 nm thickness were prepared using FIB liftout as shown (Figure 46). Sample 2 exhibits ultra-fine nanostructures of HfC at the interface

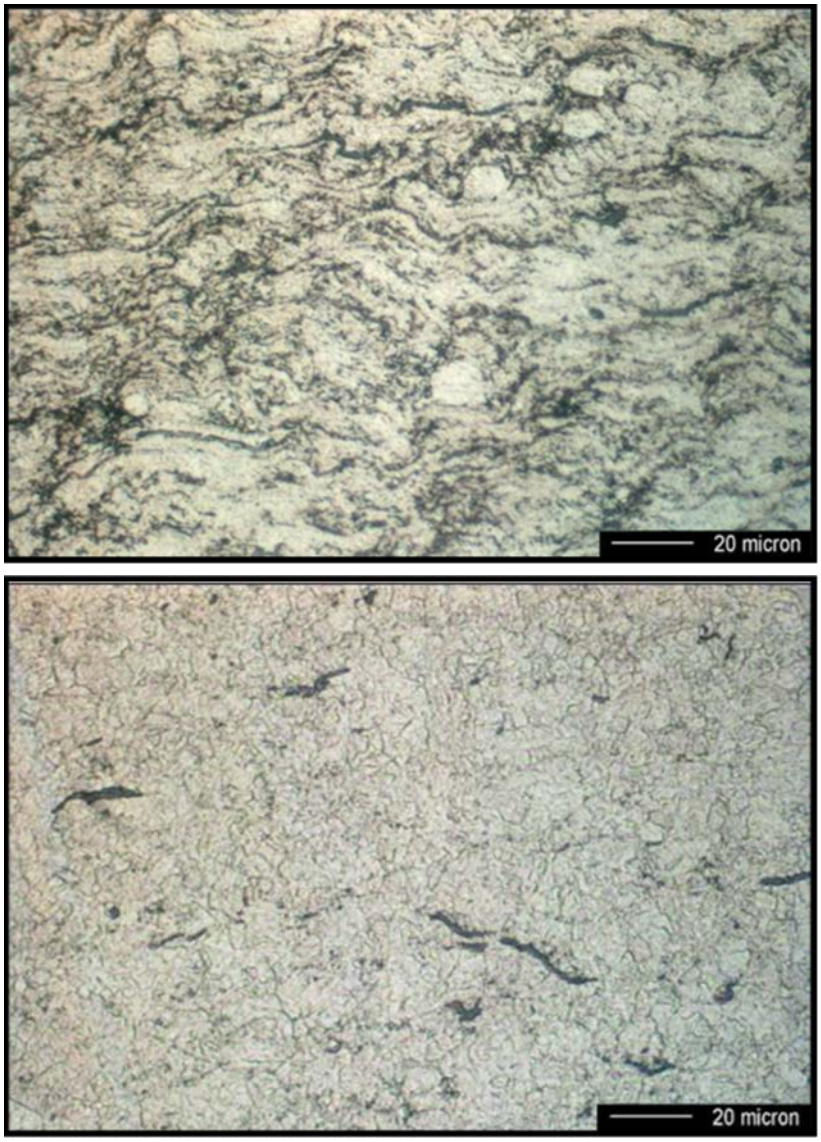

Figure 45 Bright field optical microscopic images of W-1.3wt% HfC bulk component (a) prior to and (b) after hot isostatic pressing at 1800^0C and 205 MPa for four hours.

regions. There were bending lattice fringes and stressed dense structures due to the coefficient of thermal expansion (CTE) differences of the dispersoids and the matrix, thus creating dislocations

which can enhance the mechanical properties of a MMC. The visible contrast fringes indicate the

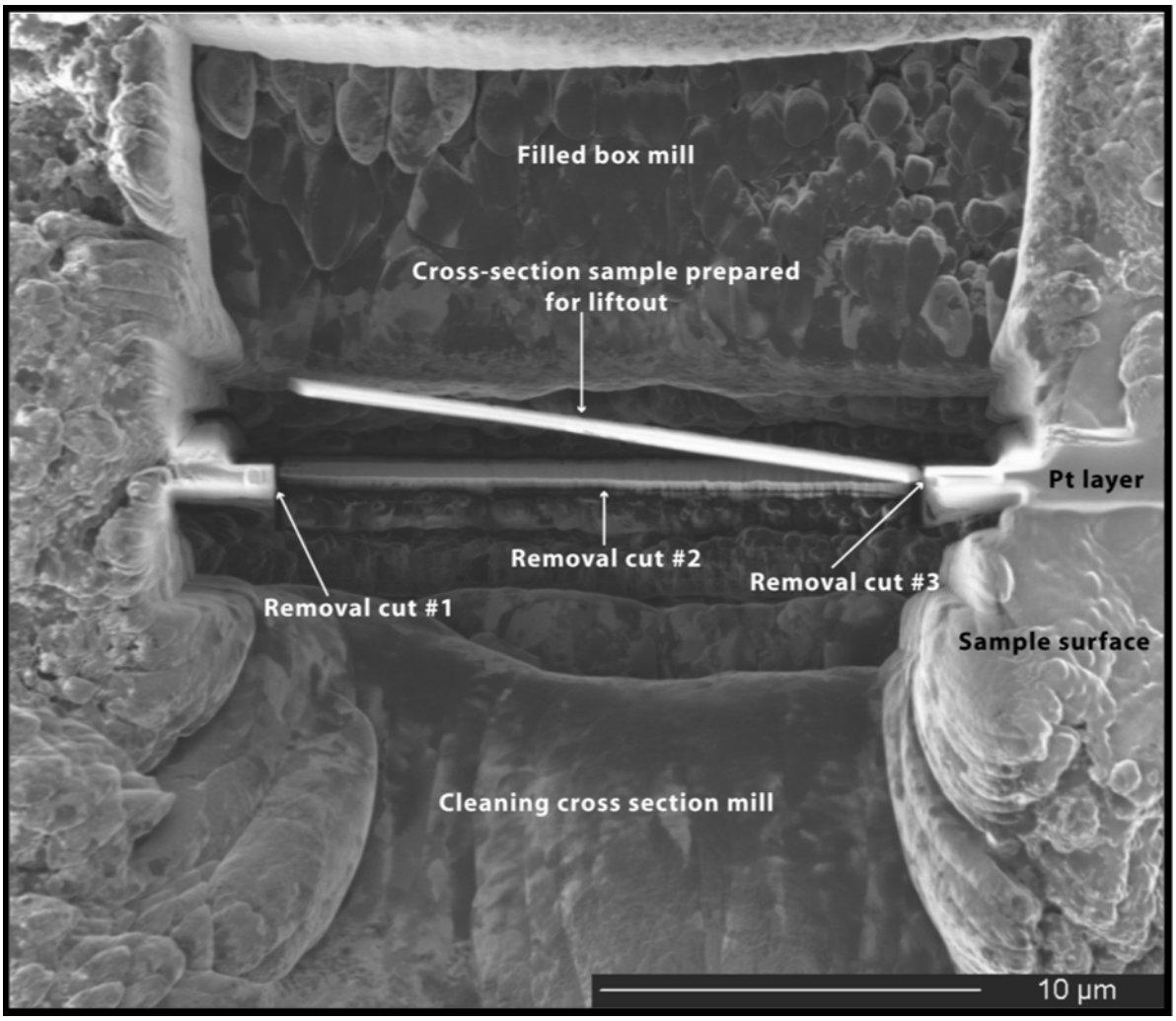

Figure 46 Focused Ion Beam liftout image of the sample gathered from secondary ion imaging. The sample has been subsequently used for TEM imaging.

presence of back stresses built up in the matrix that would tend to oppose the motion of additional dislocations and increase the strength of the material with an increase in the number of grain boundaries (see Figure 47)[123]. Selective area diffraction confirms the presence of both nano and micron-size grains. There was a fine distribution of visible structures within the grains, with grain size lower than 50 nm (Figure 48).

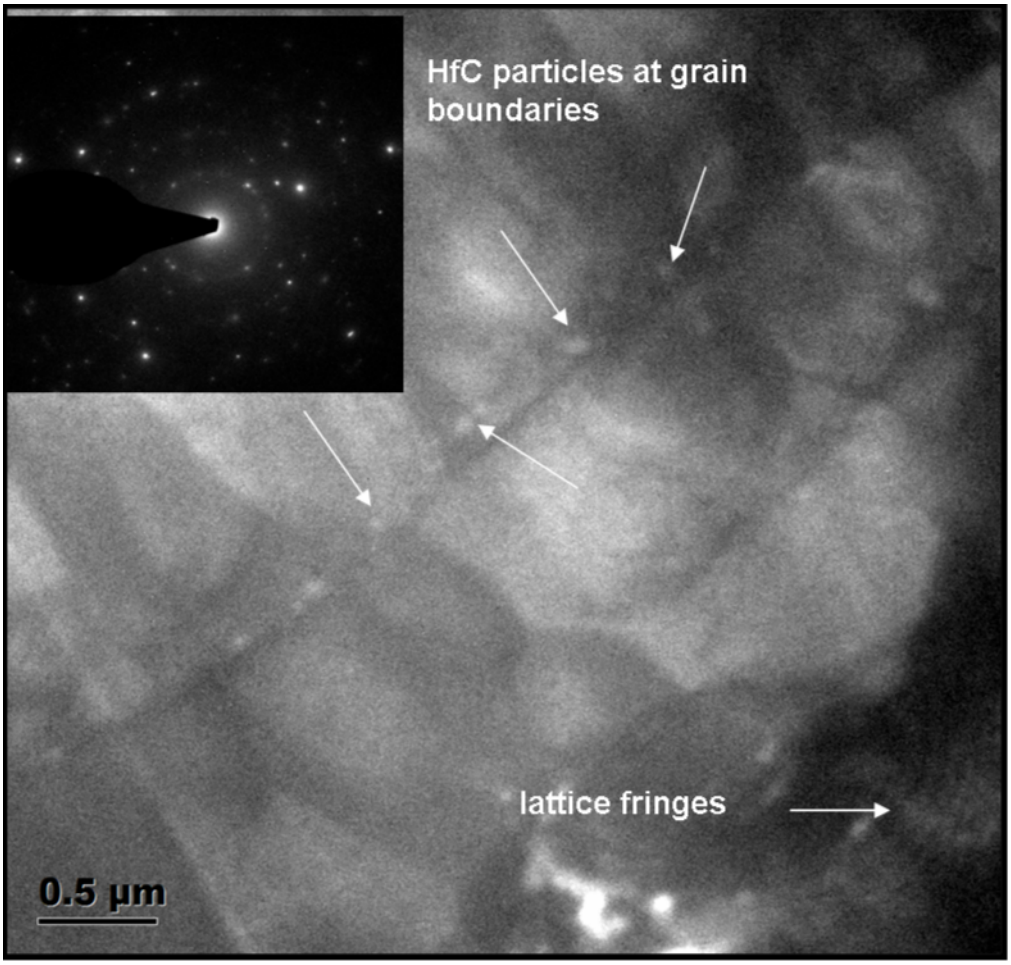

Figure 47 High resolution transmission electron microscopy (HRTEM) of the bulk component. SAD pattern revealing the crystallinity after rapid solidification.

During plasma spray forming, particle attain molten state and are subjected to rapid solidification with an effective cooling rate on the order of $10^2 - 10^4$ Ks^{-1} as opposed to the highest cooling rates of less than 10^2 Ks^{-1} provided by conventional ingot solidification[124]. As a result, there is a refinement in the W microstructure, where the average W grain size is 200-500 nm (starting grain size 1.3 micron).

Sample 3 revealed nanostructures with a HfC grain size of less than 10nm in comparison to sample 2. Grain boundaries were very well defined and distinct (Figure 49a). At higher

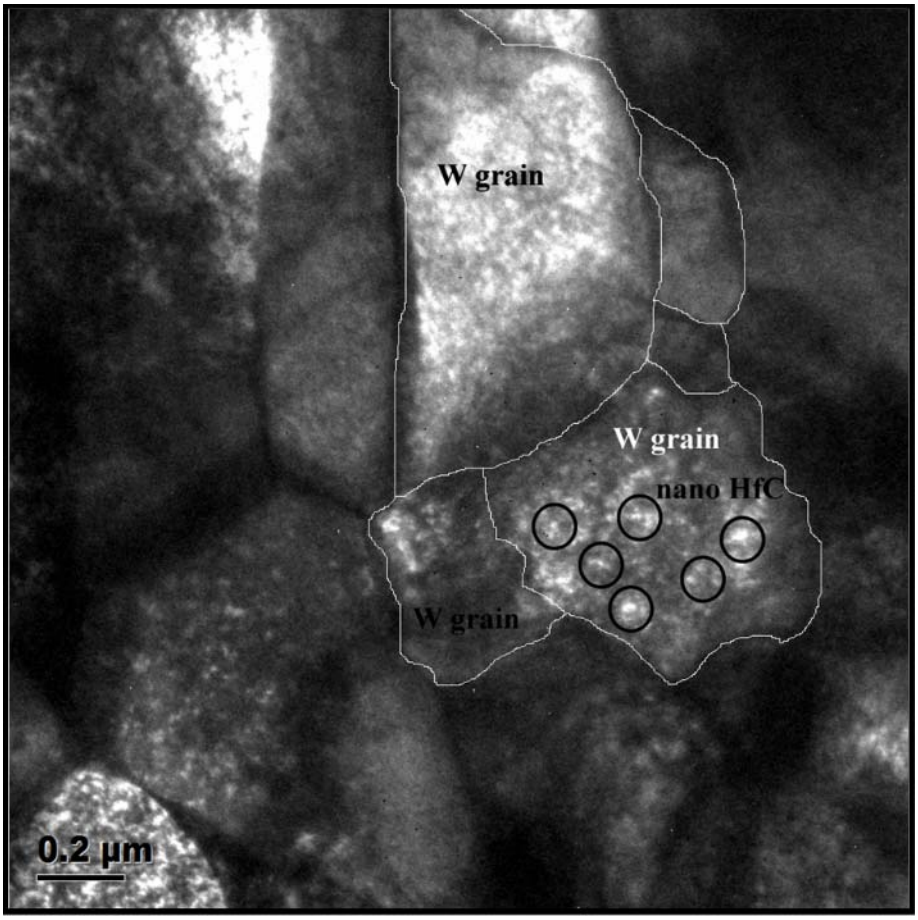

Figure 48 HRTEM image of bulk sample cross-section formed from W-1.3wt% HfC powder with the distribution of nanosize particles throughout W grains (after HIPing).

magnification, smaller reinforcing particles are found uniformly distributed throughout the larger grains (see Figure 49b,c). Nucleation is preferred to proceed at the grain boundaries as this comprises the additional interfaces required for nucleation. Furthermore, at the rapid solidification and super cooling rates present in the plasma spray atomization and deposition environment, nucleation is also known to occur within the grain boundaries themselves[110]. Intergranular nucleation was seen within these components and during characterization of a rapidly solidified Al-Si hypereutectic near-net shape component formed in related studies[117]. Nanosized hafnium carbide was found along the grain boundary (Figure 50) in sample 3.

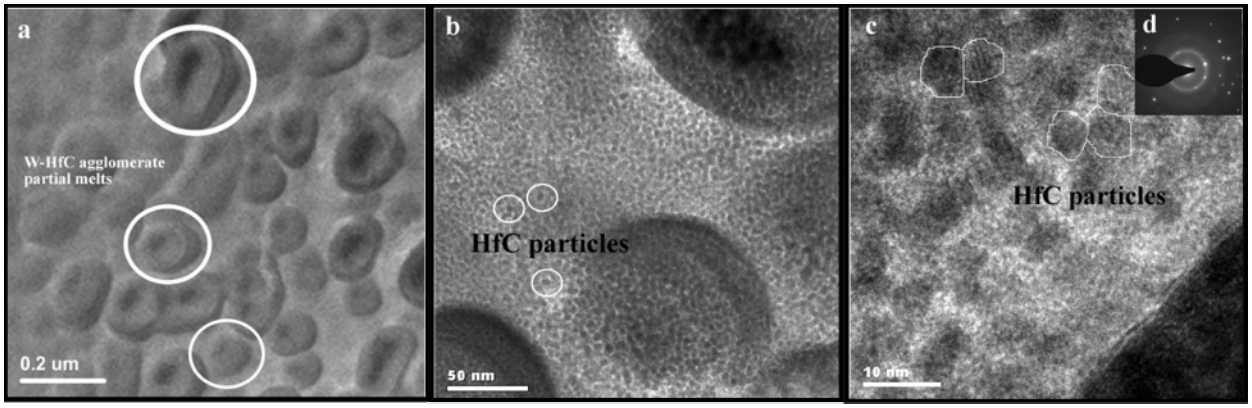

Figure 49 High-resolution transmission electron microscopic image of nanometer-scale and homogenous grain arrangements of sample formed from W-1.3 wt% HfC spray dried powder. The inset (d) SAED pattern shows several reflections of grains with ring diffraction pattern.

The spray-dry agglomeration of the feedstock powder had some unique effects on the microstructure of the final as-sprayed bulk component. Based on a larger mean particle size of the feedstock encasing the nano-reinforcement material, the HfC was able to reach a melted or at

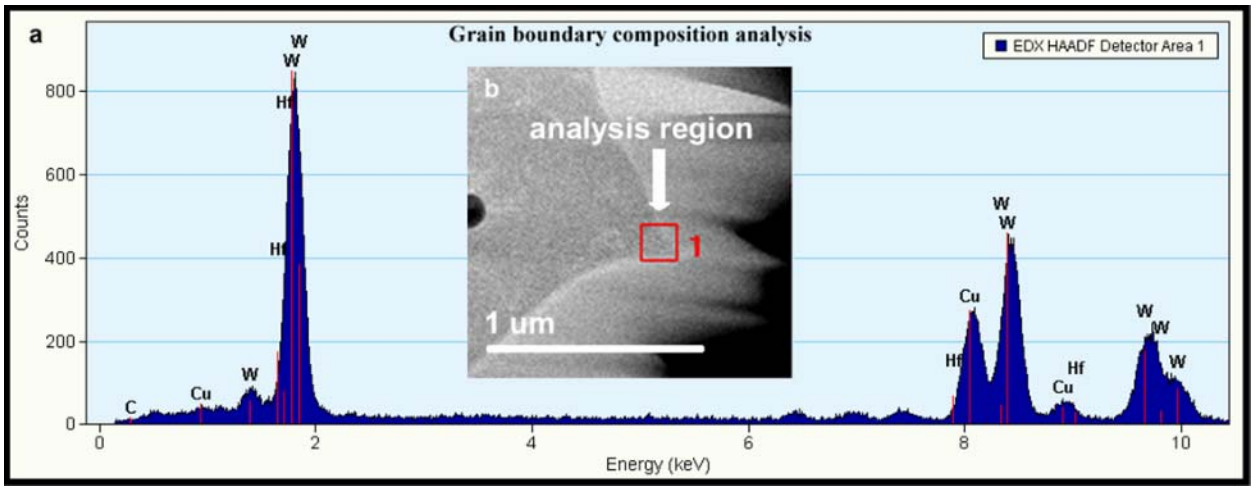

Figure 50 (a) EDX HAADF qualitative and quantitative compositional analysis near the grain interface (analysis of area inside of square box of (b) inset image) of the bulk component formed from W-1.3 wt% HfC spray dried powder.

least semi-solid state prior to deposition and resolidification as seen in Figure 49a. Otherwise, the smaller particles do not reach the critical mass needed to enter the hot zone of the plasma flame, resulting in a poor coating efficiency (and bond strength)[124]. The resulting density of the part could be directly related to the density and size distribution of the inbound agglomerate and the plasma spraying parameters for spraying and deposition[120] . Presence of HfC particulates in the path of dislocation movement provides obstacles to its motion and increase the amount of energy (stress) needed to pull a line of solute atoms from the dislocation line[123] . Within the tungsten matrix, strain hardening occurs through the creation of jogs at the intersection of dislocations. As the jogs become mobile, vacancies are created that act to slow further dislocation motion[125]. Presuming few or no alloying elements present and the number of vacancies increasing with continued stress state and increasing temperature, the edge segments of the dislocation networks begin to climb and reduce the rate of work hardening. The addition of these Hf-C strengtheners is thought to correct for this "dynamic recovery" environment and yield increased high-temperature strength[125] .

Figure 51 shows the results from the Secondary Ion Mass Spectroscopy to identify and successfully describe the presence of uniform hafnium-carbide dispersed within the matrix (sample 3) on both the convex and concave sides of the sample prepared as shown in Figure 44. An investigation by Clark[126] of an electron beam melted W-Hf alloy showed the retention of Hf in the final ingot was rather low. The addition of C to the W-Hf system is proposed to retain a higher concentration of the Hf in solution[101] as was also seen from our SIMS analysis in Figure 51. However, this investigation differs from the findings of the elevated temperature properties of the previous studies conducted by Raffo and Klopp where we conclude the strengthening not

to be due to the solution strengthening mechanism described above, rather it is precipitate-hardening (i.e. that of the carbide, either HfC or complex W-HfC). To further separate these two

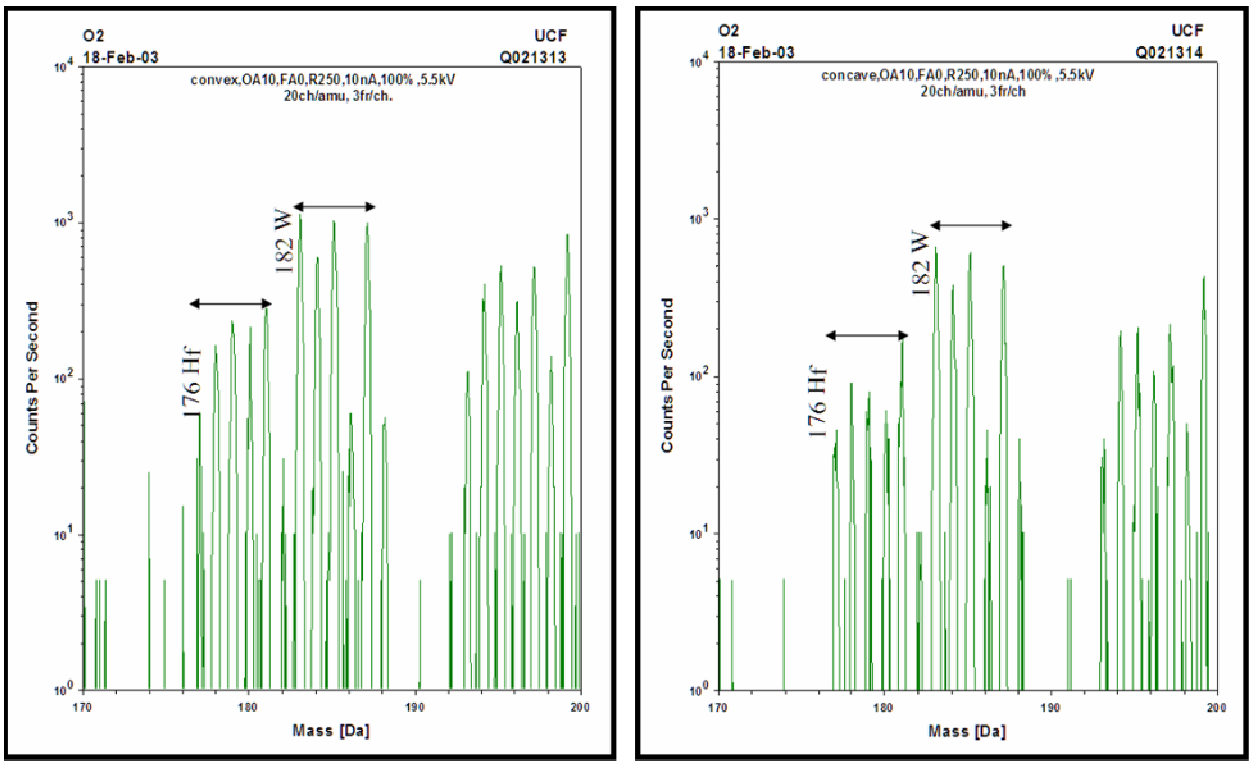

Figure 51 Secondary Ion Mass Spectrometry showing the uniform distribution of HfC for (a) the convex side and (b) the concave side of the nanocomposite fabricated from spray dried powder.

different strengthening mechanisms, the effect of solid solution alloys generally becomes negligible at a temperature above half the absolute temperature of the melting point of the parent matrix metal, in which case the strengthening mechanism would be one of another nature (i.e. dispersion-strengthened or precipitation-hardening alloys).

Because of the high thermodynamic stability and melting point of HfC, the annealing response of a W-HfC and W-Re-HfC is revealed to be slow [127]. Further, because of the low free energy of formation of HfC (much lower than other carbides including WC), this W composite containing

Hf and C would be presumed to be predominantly HfC[125]. Utilizing the size of the HfC particles, feedstock agglomeration, and the disintegration and rapid solidification effects of plasma spray forming, the particles were homogenously distributed and spaced throughout the matrix.

Figure 52a reveals the stacking faults within the matrix of tungsten and columnar tungsten grains while 52b reveals that the HfC particles are creating localized distortion of the dislocations leading to the strengthening of the nanocomposite. Figure 52 also shows the existence of stacking faults and associated strain effects, which would also explain the existence of the striped contrast patterns visible in the bottom right portion of Figure 47 [128].

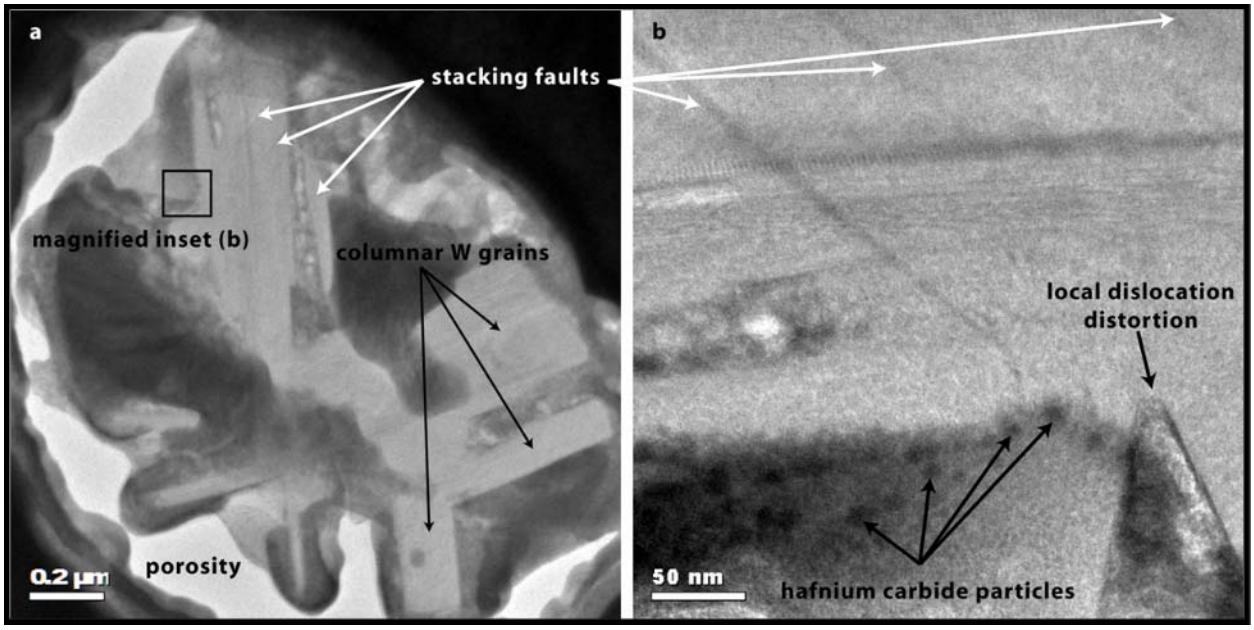

Figure 52 Transmission electron microscopic overview of sample VPS formed from W-HfC nanocomposite and (b) Presence of HfC particles creating localized dislocation distortion and thereby strengthening the nanocomposite.

6.4. Conclusions

The nanoscale hafnium carbide reinforcement noticeably increased the elastic modulus and hardness of vacuum plasma spray formed bulk nanocomponents. The carbide was found to lie in

and around the grain boundaries, which would tend to impede dislocation movement by pinning the grain boundaries and subsequently increasing the strength. VPS forming combined with hot isostatic pressing (HIP) increased the density (~ 99%) and the mechanical properties. Increase in the elastic modulus and the hardness was caused by defect structures, high density, and the presence of reinforcing carbide strengthening throughout grain boundaries. Spray drying of the powder feedstock was found to have a direct effect on the density and the corresponding resultant nanostructure retention in the spray formed composites. Thus, it has been proved that Vacuum Plasma Spray is an effective tool for development of bulk metal matrix composites with improved hardness and elastic modulus.

CHAPTER 7 $MoSi_2$ BULK NANOCOMPOSITE

7.1 Introduction

In the drive toward advanced high thrust-to-weight ratio propulsion systems, the development of high strength, low density structural materials for applications at temperatures above 1600°C, is required. At present, the engine designers are limited to maximum continuous operating temperatures of approximately 1100°C by commercially available super alloys. For higher temperature applications, the $MoSi_2$ system shows considerable promise because of its high melting point (2030°C) and excellent oxidation resistance, suitable for candidate materials in future propulsion applications[129-130]. However, $MoSi_2$ suffers some severe deficiencies, such as low ductility and toughness below 1000°C, and poor strength and creep resistance in the regime above 1200°C[129,131,132] Various composite fabrication strategies have been proposed to improve the room temperature toughness and high temperature strength of $MoSi_2$. Recent efforts to overcome these problems have focused primarily on development of ceramic reinforced $MoSi_2$ composites. Silicon-based ceramic materials such as SiC and Si_3N_4 showed considerable improvement in strength, oxidation resistance, and thermal stability in $MoSi_2$ matrix[133-135]. The Si_3N_4 has a high thermal shock resistance due to its low thermal expansion coefficient (CTE) and has good resistance to oxidation when compared to other structural materials[136-138]. Mechanical properties of $MoSi_2$ has also improved with the addition of Si_3N_4. As a result of such reinforcement, the high temperature creep strength increases by five orders of magnitude and the room temperature toughness doubles. The addition of Si_3N_4 has also permitted the use of reinforcing fibers such as SiC resulting in reduction of the overall CTE[139]. Gac and Petrovic [129, 140] have studied the mechanical properties of hot-pressed $MoSi_2$ and SiC-whisker-reinforced composites and reported improved room temperature toughness and high temperature strength.

Sadananda et al.[141] have observed significantly reduced creep rates in the temperature range of 1100–1400°C in SiC-reinforced $MoSi_2$ composites. Another important feature toward improving the mechanical properties of the near-net-shape forming is the consolidation technique. Traditional consolidation techniques such as cold pressing and sintering at high temperatures, hot pressing, and hot isostatic pressing have strong limitations in the control of grain size at the nanoscale due to excessive grain growth during processing. Several synthesis techniques such as sol–gel amalgamation, chemical vapor deposition, electron beam evaporation, and plasma-assisted techniques have been adapted to process nanocomposite materials[142,143]. In the past decade, plasma spray has been applied in the development of protective coatings. Recently, plasma spray has been used by several research groups to deposit nanostructured coatings such as WC, Cr_3C_2, Al_2O_3–TiO_2, ZrO_2 [144-147]. Plasma spray forming of nanocomposite materials is a promising near-net-shape manufacturing technology, combining melting, blending, and consolidation into a single operation. This article presents the challenges for the successful consolidation of the $MoSi_2$–Si_3N_4–SiC nanocomposite using plasma spray forming. The microstructure, the mechanical, and the oxidation properties of the reinforced $MoSi_2$ bulk nanostructured component have been studied systematically.

7.2 Experimental

7.2.1. Preparation of $MoSi_2$ and Si_3N_4 powder

50 wt% $MoSi_2$ (20μm in size), 50 wt% $Si3N_4$ + $MoSi_2$ (50–100 nm) with 4wt% SiC powder particle were mixed using conventional ball-milling techniques. The resulting powder was characterized using SEM in order to observe the degree of mixing. Figure 53(a) shows the nanosized $MoSi_2$–Si_3N_4 powder. Irregular sized particles are a result of ball milling. Figure 53(b)

shows a homogeneous mixing of the dual size $MoSi_2$–Si_3N_4–SiC powder. To avoid problems associated

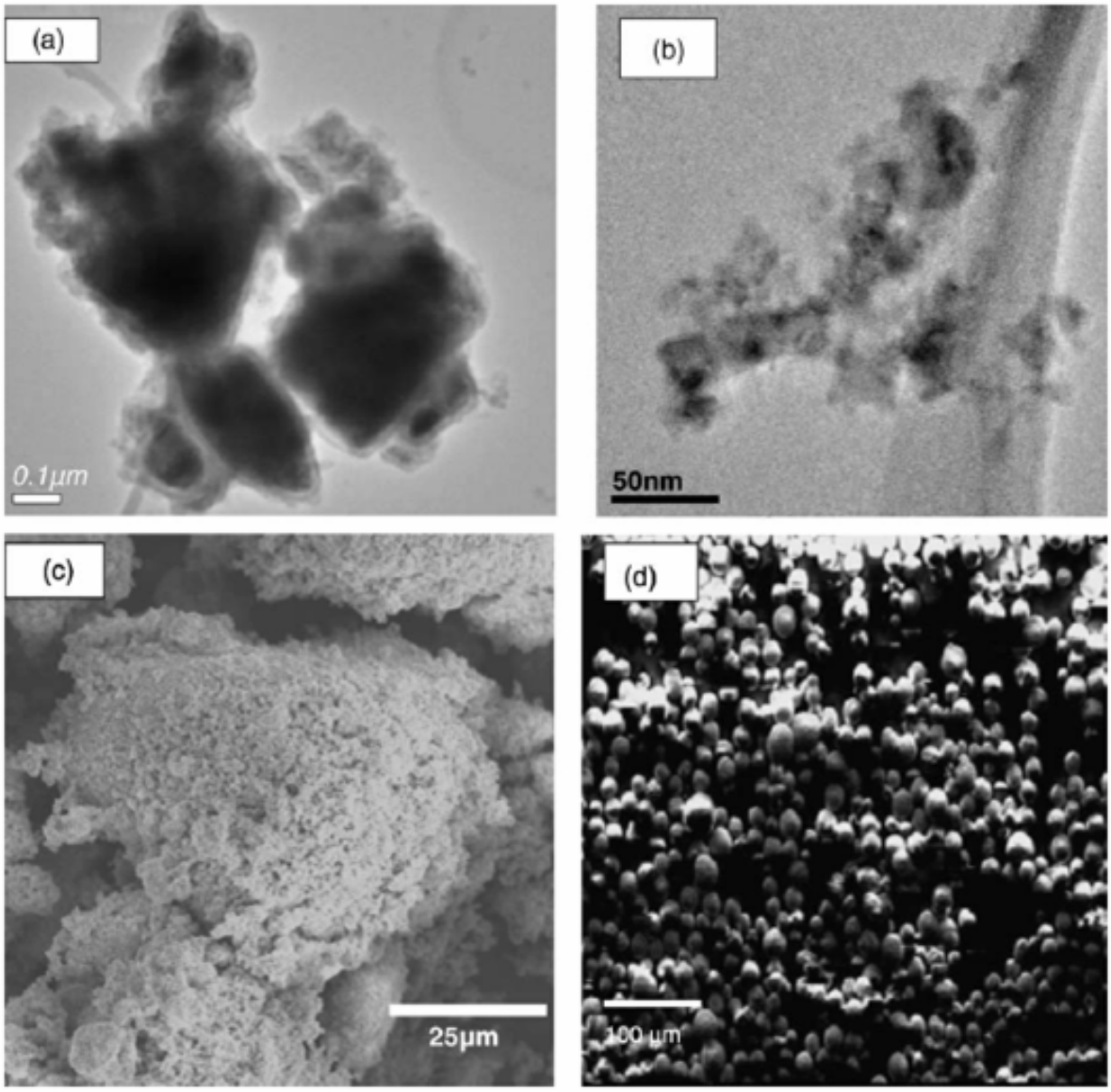

Figure 53 TEM micrograph of as received nanosized (a) $MoSi_2$-Si_3N_4 particles, and (b) after sonification,(c) SEM micrographs of blended $MoSi_2$-Si_3N_4 particles before plasma spray forming (d) agglomerated $MoSi_2$-Si_3N_4-SiC nanoparticles after spray drying

with the flow and other hindrances of nanoparticles in the plasma gun, the powders were agglomerated using a spray dryer. Figure 53(c) shows the agglomerated powder particles in the range of 10–30 μm, ideal for the plasma spraying.

7.2.2. Plasma spray forming

The accelerated powder particles entrained in the plasma flame are deposited on the cooled rotating 1 in. carbon mandrel of a desired shape and size. The details of the mandrel design have been discussed elsewhere in detail[148]. The machined mandrel had a surface finish of 0.5μm. The smoother mandrel surface finish was essential for both deposition and separation of the spray deposited material in order to yield a freestanding nanostructured component. The nano–micro $MoSi_2$–Si_3N_4–SiC powder was sprayed in vacuum using a Praxair Surface Technologies (Indianapolis, IN) SG 100 gun manipulated by robot arm inside a 60 in. diameter water cooled vacuum chamber. Argon was used as the primary gas and helium as the secondary gas. The optimization of the plasma parameters are already reported[149] and presented in Table 15.

Table 15 Plasma spray parameters for fabrication of $MoSi_2$ nanocomposite bulk part

Parameters	**Value**
Torch Power, kW	29
Ar Flow rate, SCFH	170
He Flow rate, SCFH	38
Vacuum Level, Torr	400
Motion parameters	Torch @ 200 in./min, part @ 40 rpm

Plasma parameters were controlled in order to minimize the coarsening and melting of the nanosize powders. For example, 30 min of deposition time formed a 0.25 in. wall thickness tube. After spray deposition, the mandrel was cooled in liquid nitrogen to facilitate the release of the spray-formed bulk nanocomposite due to CTE mismatch between the mandrel and the

composite. Figure 54 shows a plasma spray formed cylindrical near-net-shape bulk reinforced $MoSi_2$ nanocomposite of diameter 3.4 cm, a wall thickness of 0.5 cm, and a height of 2.4 cm.

Figure 54 The appearance of plasma sprayed ring type $MoSi_2$-Si_3N_4-SiC nanocomposite with a diameter of 3.5 cm, a wall thickness of 0.5 cm and a height of 2.4 cm.

7.2.3. Structural characterization and mechanical properties

A detail characterization of the spray-formed bulk nanocomposite was performed using several analytical tools such as scanning electron microscopy (SEM), transmission electron microscopy (TEM), and Vickers hardness tester. Characteristics such as powder shape, size, and porosity in the sprayed nanocomposite was observed using SEM. Vickers hardness measurements were performed on a Shimadzu HMV-2 Vickers hardness tester using a Vickers indenter with a load of 19.6N applied for 15 s. The fracture toughness of the nanocomposite was calculated using an equation, described in [150] by measuring the crack length obtained from the Vickers hardness indenter. Scanning transmission electron microscopy (STEM) measurements were performed to observe the retention of nanosized grains, their morphology, and the distribution of particles

occurring in the spray-formed nanocomposite structures. A FEI (Hillsboro, OR) 200 TEM-FIB (Focused Ion Beam) equipped with a 25–50 kV gallium liquid metal ion source (LMIS) was used for preparing thin TEM specimens from the spray-deposited nanocomposite. A current density of 108Acm^{-2} at the LIMIS surface was approached to induce ion emission. A high beam current was used for removing large quantities of material for cleaning while a low beam current (500 pA) was used for refining the cut area for lifting out of the specimen. A Philips (Tecnai Series) high-resolution transmission electron microscope operated at 300 kV was used for detailed microscopic analysis.

7.2.4. High temperature oxidation

Isothermal oxidation of the nanocomposites was performed in the dry air to study the oxidation kinetics of the spray formed composite component. The ring type sample was machined from the spray deposited composite shell and subjected to 1100°C, and held isothermally for 10, 50, 100, 200 h. The mass change is recorded using a Saratorius balance connected to the oxidation furnace to monitor the oxidation kinetics.

7.3. Results and discussion

7.3.1. Microstructure

In this article, reported for the first time, is the successful fabrication of the $MoSi_2$–Si_3N_4–SiC cylindrical bulk nanocomposite without any defects such as cracks and dimple on the surface using plasma spray technique. The relative density of the nanocomposite measured by Archimedes method was about 90%. It should be noted that the density of the deposited materials depends largely on the plasma processing factors such as current, voltage, plasma gas flow rate, etc. Optimizing the aforementioned parameters will improve the density of the near-

net-shape bulk nanocomposite. Figure 55 shows the SEM micrographs of the polished cross section view of the plasma sprayed nanocomposite as a function of the wall thickness. The

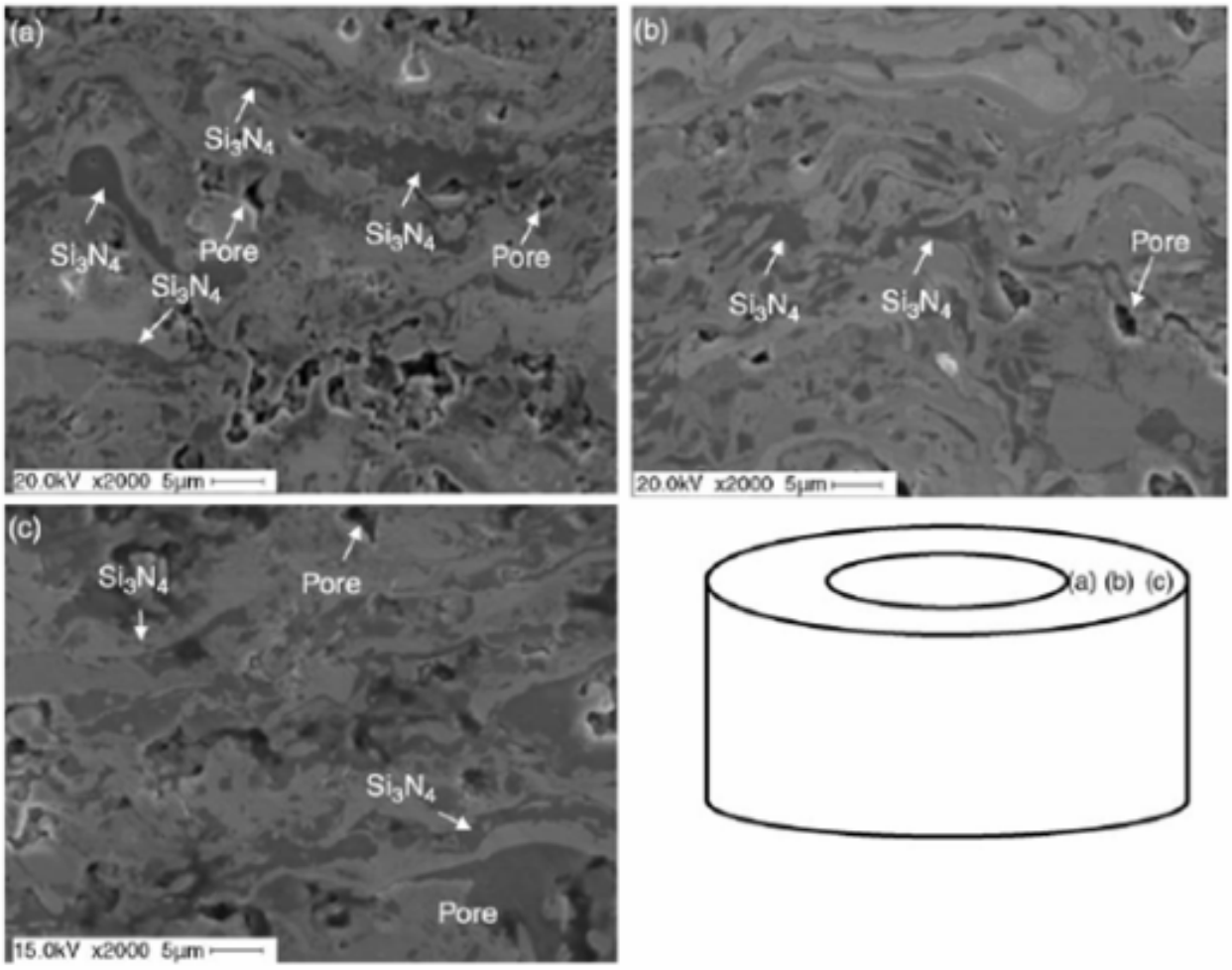

Figure 55 SEM micrographs of the cross section of the plasma sprayed cylindrical bulk nanocomposite with thickness (a) inside (b) middle and (c) outside portion of the cylinder

microstructures at different wall thickness locations exhibit a general view of a plasma sprayed laminate, usually observed in plasma spray processing. Only $MoSi_2$ and Si_3N_4 phases were found in the deposits as confirmed by SEM–EDS. On Figure 55 Si_3N_4 particles (dark gray color), $MoSi_2$ matrix (light gray) and the pores (black) are indicated by arrows. It was rather difficult to

distinguish the SiC particles using SEM–EDS due to the small volume fraction of SiC. The Si_3N_4 phase in the $MoSi_2$ matrix has a lamella-like morphology, as shown in Figure 55. The examination of the microstructures at the different areas of the nanocomposite revealed elongated Si_3N_4 particles (as marked on the micrographs). The features are in the average size of 15 μm for the inner and 10 μm for the outer region of the cylinder. On the contrary, the size range of the Si_3N_4 particle on the middle region of the cylinder was below 5 μm. The Si_3N_4 phase distribution within the $MoSi_2$ matrix was found to be uniform. Using quantitative microscopy, it was estimated that the composite contains 10–17 vol.% Si_3N_4 particles in the $MoSi_2$ matrix. As can be seen by relating the microstructure as a function of the wall thickness of the composite, the microstructural variations are attributed to the deviation in residual heat, residual stress, substrate condition, and surface diffusion. Each of these factors can be directly controlled by the plasma spray forming processes such as mass flow parameters mentioned previously, and the temperature of the substrate. As discussed by Holland [151], the nature and energy of these bombarding species will be dependent on the process parameters and geometrical aspect of the substrate within or outside the plasma zone. As a result of substrate bombardment, numerous changes may take place, such as substrate heating, reemission or sputtering of deposited material, gas incorporation in the deposited bulk, and modification in the deposit structure and density. Thus, plasma–substrate interactions also may have significant effect on the final microstructure and the properties of the near-net-shaped component. Figure 56a shows that the morphology and distribution of Si_3N_4 and SiC nanoparticles in the MoSi2 matrix. The resultant microstructure shows the homogeneously dispersed Si_3N_4 nanoparticles embedded in the $MoSi_2$ matrix. In addition, it was observed that some of the $Si3N_4$ nanoparticles were agglomerated to as high as 200 nm, as indicated by arrows A in Figure 56a. The distributed

particles (arrows B) have a size range of approximately 100 nm with spherical shape. Microstructural investigations at higher magnification (Figure 56b) reveal that the size of the $MoSi_2$ in coarse area varies between 0.5 and 1 μm and the Si_3N_4 particles embedded in matrix, marked by arrows, are in the range of 30–100 nm. It should be noted that in some other areas the

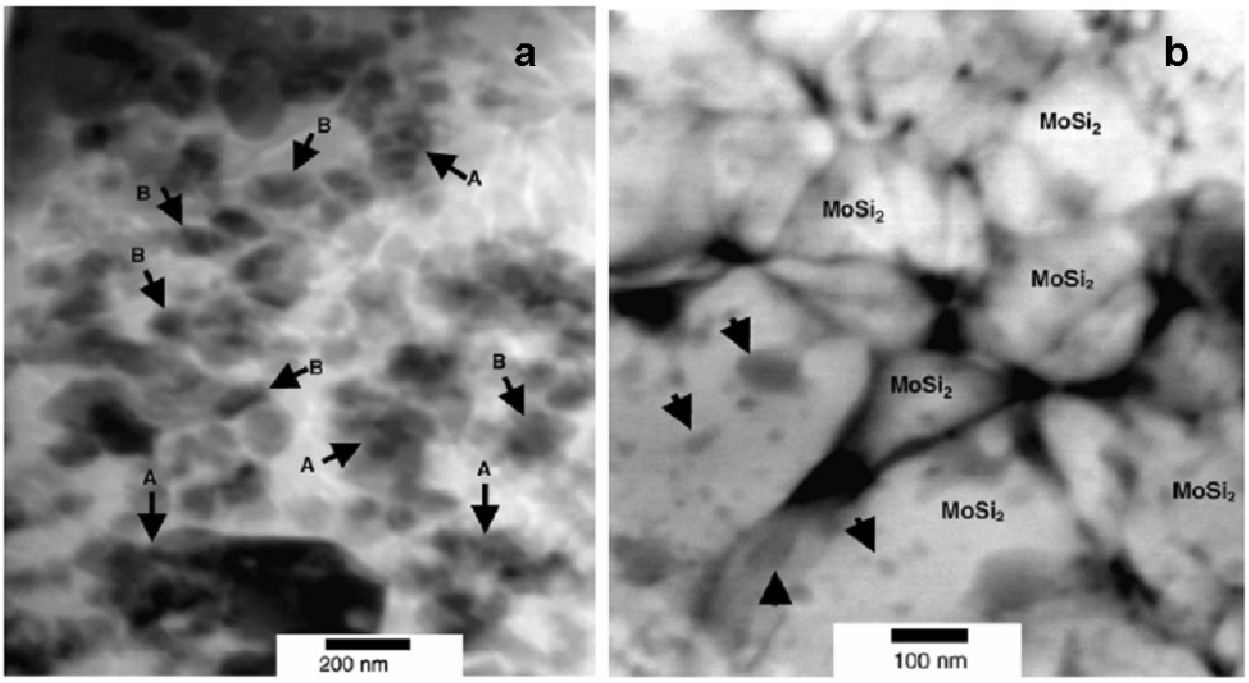

Figure 56 (a) STEM bright field image of the plasma sprayed bulk nanocomposite showing homogenously distributed fine particles in $MoSi_2$ matrix. (A: agglomerated, B: non agglomerated reinforcements), (b) STEM bright field image of the plasma sprayed bulk nanocomposite showing fine particles embedded $MoSi_2$ grains.

$MoSi_2$ phase varies between 100 and 200 nm. STEM analysis thus showed the promise of plasma spray consolidation of nanocomposites with retained nanostructures. The possible explanations of the fine nanosized particles in this bulk nanocomposite could be related to the suppression of the surface diffusion by extremely fast translation of ceramic materials through the high temperature zone (plasma flame), and thus, preventing the coarsening time. During conventional sintering, to the contrary, a significant time is spent in the temperature range where the

coarsening effect of surface diffusion outweigh the densification produced by the grain boundaries and the lattice diffusion[152]. Besides, in the nanostructures, surface melting is preferred in the fast translation thus keeping the core intact. In addition, the small sized particles clearly contribute toward preventing the thermally induced microcracking. Similar microstructure was also observed in hot isostatically pressed $MoSi_2$–Si_3N_4 ceramics pellets[153], however the particle sizes larger than in the present research (such as 200–1000 nm for $MoSi_2$ and 500–1000 nm for Si_3N_4). Hence, it is expected, that the uniformly distributed Si_3N_4 nanoparticles in the $MoSi_2$ matrix definitely enhance the mechanical properties of the plasma spray formed composite.

7.3.2. Mechanical properties and fracture surface morphology

Figure 57 shows the variation in the Vickers hardness as a function of the wall thickness of the nanocomposite. The different Vickers hardness with wall thickness might be associated with the different distribution and the size of the Si_3N_4 particles in the $MoSi_2$ matrix. The narrowed error bar of Vickers hardness correspondent to the middle region of the specimen is related to homogeneously distributed fine particles in the region. In addition, the different amount of porosity in different regions can be another important factor leading to different Vickers hardness as well. Despite the porosities, the homogeneously distributed nanosized particles, and the small interparticles spacing in the matrix can be the foundations of the increased hardness of the composite [154]. The importance of the grain size effect to the strengthening of the $MoSi_2$ based materials is already reported [155]. It is concluded that the grain size is considerably more important for increasing the strength of the composite than the volume fraction of reinforcement.

The fracture toughness of the nanocomposite was calculated by the crack length obtained from the Vickers hardness indent.

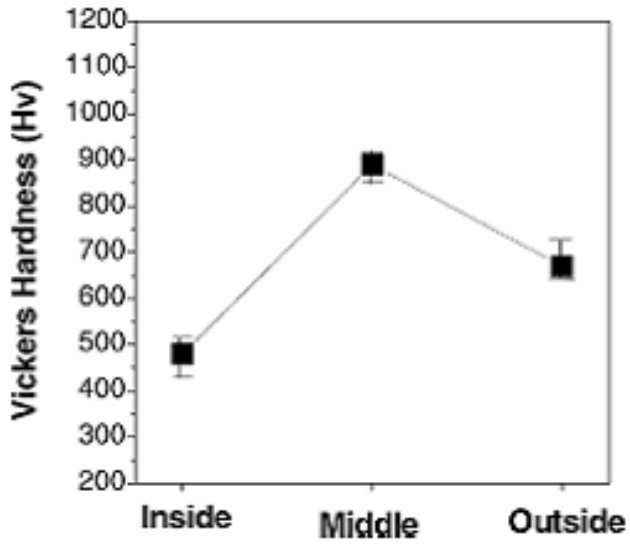

Figure 57 Vickers hardness of the plasma spray formed bulk nanocomposite with thickness.

Despite the secondary cracking, the longest crack was selected as the baseline for the calculation. Internal stresses were produced within the sample as a result of the thermal expansion mismatch. Therefore, the residual stresses may be the reason for the micro-cracking and tortuous crack propagation[156]. Figure 58(a and b) shows representative SEM micrographs of cracks formed from the corner of the indenter. The crack-microstructure interactions which contribute to the fracture toughness are evident in these micrographs. In Figure 58(b), crack deflection was observed as a result of the uniformly dispersed particles in the plasma sprayed nanocomposite. Cracks formed from the corner of the indent propagated easily without tortuous. However, the interaction between the crack and the reinforcement particles resulted in the crack deflection.

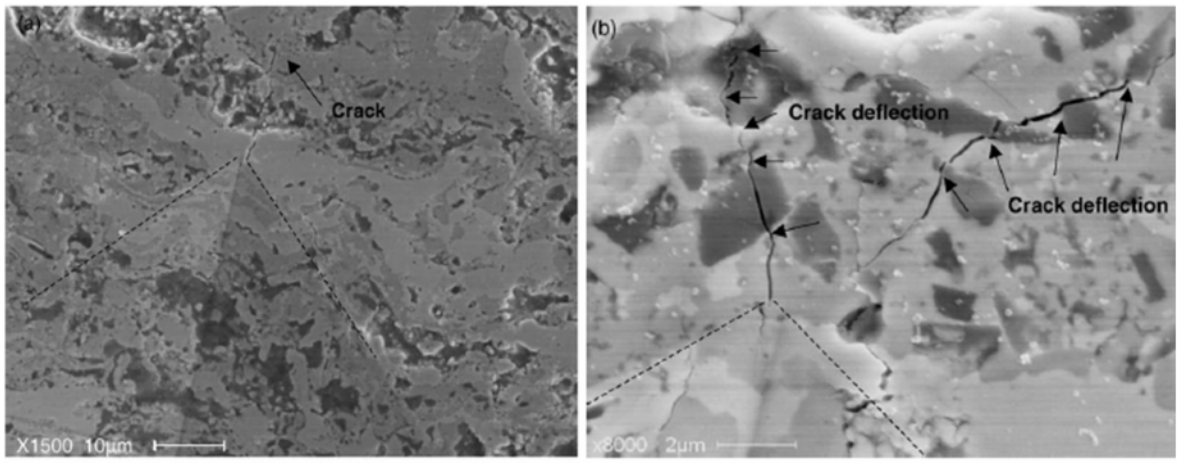

Figure 58 SEM micrographs of bulk nanocomposite showing cracks formed from the corners of hardness indents.

Microscopic analysis (Figure 58(b)) demonstrates that the direction of the crack propagation was changed whenever it meets the particles in the matrix and propagates around them. Finally, it is expected that the small particles and their homogeneous distribution are more prone to the crack deflection. The crack lengths in different wall thickness regions of the composite cylindrical specimen (Figure 58) are used in the calculation of the fracture toughness of the composite. The variations in the fracture toughness as a function of wall thickness are presented in Figure 59.

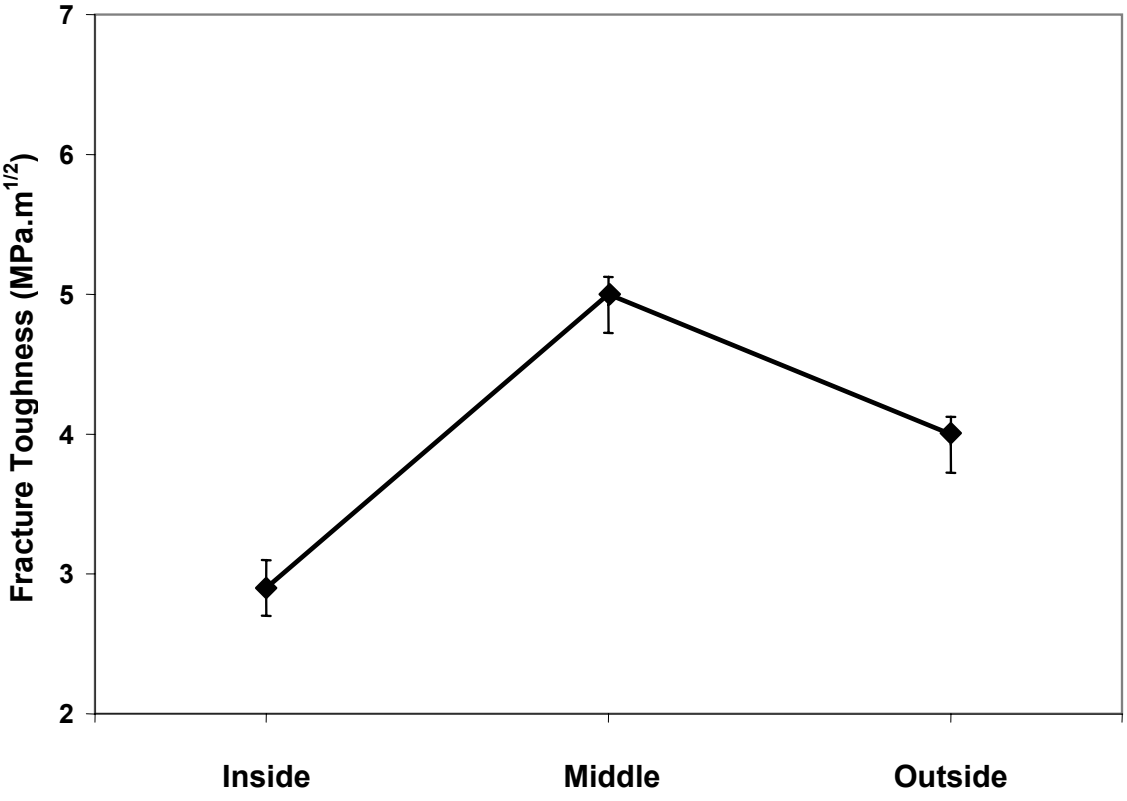

Figure 59 Variation of fracture toughness of bulk nanocomposite as a function of wall thickness.

The room temperature fracture toughness of the nanocomposite at the middle of the composite was ~5MPam$^{1/2}$. It should be noted that this result is almost twice the one reported for a monolithic $MoSi_2$. In addition, this value is similar to that reported for both $MoSi_2$–$30Si_3N_4$ and $50Si_3N_4$ [152] produced by the HIP. The homogeneously distributed fine microstructure in the middle region of the cylinder showed relatively higher fracture toughness than the other regions of the composite. Carter et al.[157] have suggested that such outcome can be achieved by crack deflection and crack bridging. In the current research, a crack deflection phenomenon has been observed. Therefore, it is assumed that Si_3N_4 and SiC nanoparticles reinforcements in the $MoSi_2$ matrix could enhance the fracture toughness by a similar mechanism. Further improvement in the

room temperature fracture toughness of near-net-shape $MoSi_2$–Si_3N_4–SiC composites is attributed to the fine and homogeneously dispersed particles. Furthermore, it can be noted that the porosity of this composite might also prevent the crack growth near the indents. However, the reason behind the increase in the fracture toughness and the hardness is due to the inclusion of SiC and Si_3N_4 nanoparticles in the $MoSi_2$ matrix remains to be explored. Figure 58 shows SEM micrographs of the fracture surface regions of the plasma formed bulk composite. The figure shows fully melted coarse $MoSi_2$ particles and the partially melted/unmelted, retained spherical nanosized particles as indicated by the arrows. It is believed that most of the large agglomerates that pass through the hot core of the plasma flame may undergo "explosion" resulting in a large number of nanoparticles[143]. A large fraction of the nanosized particles are either partially melted or unmelted and embedded both in the molten matrix and on the boundaries as shown in Figure 60(a and b). In addition, porosities were observed at the MoSi2 particles boundary. Marks 'A' of Figure 60(a) show the particles pulled out from the matrix. This can be an indication of a combination of cleavage fracture through the particle and the ductile fracture of the matrix as marked 'B' in Figure 60(b). The homogeneously distributed fine Si_3N_4 nanoparticles in the matrix are shown in Figure 60(c).

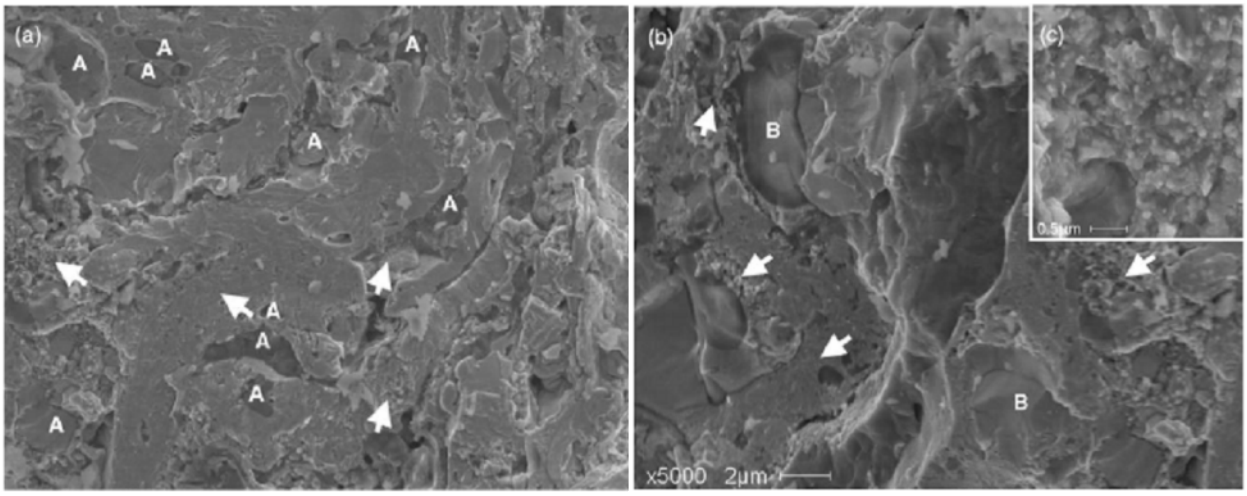

Figure 60 SEM micrographs of the fracture surface of the plasma sprayed reinforced bulk nanocomposite.

7.3.3. Oxidation kinetics

Figure 61 shows the weight change at 1100°C as function of exposure time. It is shown that the oxidation rate (weight gain) is increased at the early stages (10 h), as indicated by an accelerated oxidation behavior. The kinetics was found to saturate after 100 h exposures. Defects such as cracks, pores, and SiO_2 inclusions in $MoSi_2$ matrix have been the probable contributing factors affecting accelerated oxidation[158-161]. During the first cycle, rapid oxidation of the surface is due to the formation of SiO_2 resulting in weight gain. Partial increase in mass gain at early stages may be attributed to the increase in the exposed surface porosity, shown in Figure 55. Hence, the density of this $MoSi_2$–Si_3N_4 nanocomposite is extremely important for controlling its oxidation behavior. At higher temperatures, a thin continuous protective oxide (SiO_2) layer forms, corresponding to very small weight gain over a long period of time. However, the oxidation rate at 200 h was found to decrease. The reason for this variation may be due to the evaporation of MoO3. The volatility of MoO_3 plays an important role in the oxidation behavior of $MoSi_2$. At elevated temperatures (>1000 °C), MoO_3 vaporizes and the diffusion of Si is rapid enough to

form a continuous protective oxide scale, which effectively seals the surface[162]. In the temperature range of 600–1100°C, $MoSi_2$ exhibited a thin oxide layer on the surface due to internal oxidation of Si. A competition between SiO_2 formation and MoO_3 volatilization occurs, keeping the mass gain in ±1mg cm^{-2}. Furthermore, such a high oxidation resistance at 1100°C is due to the presence of a high volume percent Si_3N_4 which affects the suppression of the rapid oxidation of $MoSi_2$ and SiC particles.

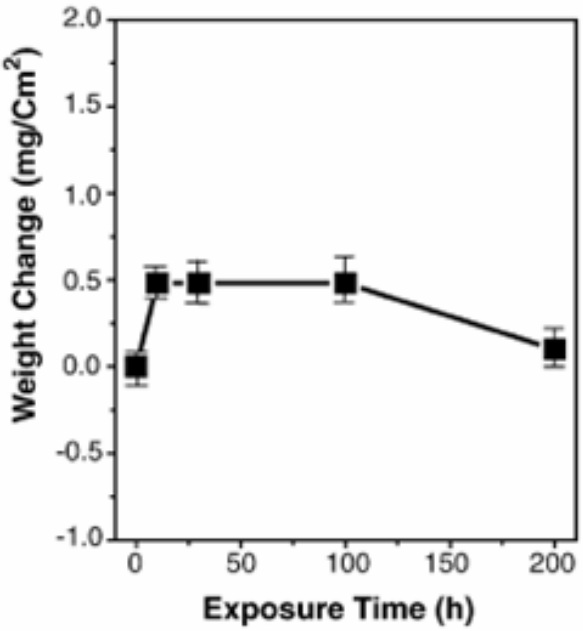

Figure 61 Oxidation kinetics of the nanocomposite exposed at 1100^0C in dry air as a function of time.

7.4. Conclusions

Near-net-shape $MoSi_2$–Si_3N_4–SiC bulk composite has been successfully consolidated with retained nanostructure using plasma spray forming. The homogeneously distributed fine microstructure in the middle region of the cylinder showed relatively higher fracture toughness

than the other regions of the composites. The average fracture toughness of the bulk nanocomposite was 5 $MPa.m^{1/2}$. The higher fracture toughness could be attributed to the crack deflection by homogeneous distribution and the retention of nanostructures. The fracture surface of the nanocomposites shows homogeneously distributed nanoparticles in the melted matrix. The oxidation behavior of the nanocomposite during the initial stages of exposure at 1100°C was accelerated due to SiO_2 formation, however, insignificant mass change is observed during long term exposures. Finally, optimization of the plasma spray forming parameters will lead to the fabrication of bulk nanocomposites with higher density and even further enhanced mechanical properties.

CHAPTER 8 CONCLUSIONS

The research has been focused on utilization of Air Plasma Spray process for processing of nanostructured coatings and bulk components. Nanostructured coatings have been achieved both using powder and solution precursor feedstock.

8.1 Nano Alumina Coating

- Spray drying temperature of 1300C yielded spherical agglomerates and has yielded less micropore volume among the four temperature variants experimented for an easy flow of nanoparticle in the plasma plume.

- The gases for creating the plasma in DC plasma torch and the rationale behind choosing the gas mixtures have been demonstrated through analytical heat transfer calculations.

- The velocity of the particles in the flight plume to achieve complete melting have been calculated and experimentally verified in the resultant APS coatings (240 m/s yields a dense nano structured coating).

- A maximum density of 96-97 % is achieved by using high carrier gas (13 SCFH). Nanostructures (40-50 nm) could be retained using the given set of parameters during APS deposition.

8.2 Nano Ceria Coating

- SPPS was successfully utilized in the fabrication of nanostructured ceria coating on a Martensitic steel.

- Gas flow rates, solution feed rate, substrate stand off distance have been optimized to achieve a dense nanostructured coating.

- the feasibility of the dissociation of cerium nitrate to cerium oxide is found at 298^0C and further correlated with the DSC analysis.

- Subsequent exposure to high temperature oxidation at 1000^0C for 24 hours revealed the protective nature of the nanoceria coating as compared to the bare substrate.

- The oxidation kinetics is parabolic in nature and the kp values were reduced by two orders of magnitude compared to the uncoated sample.

8.3 Ni-Alumina Bulk Nanocomposite

- Electroless Nickel coated alumina particles have been successfully used to manufacture a free-form bulk nanocomposite with improved hardness and fracture toughness.

- Wettability study of Nickel on polycrystalline Alumina revealed the contact angle which validated the self affine roughness model being used to calculate the apparent contact angle.

- High fracture toughness can be attributed to the nanostructured Nickel which arrests the crack propagation.

8.4 W-HfC Bulk Nanocomposite

- The nanoscale hafnium carbide reinforcement noticeably increased the elastic modulus and hardness of vacuum plasma spray formed bulk nanocomponents.

- VPS forming combined with hot isostatic pressing (HIP) increased the density (~ 99%) and the mechanical properties.

- Increase in the elastic modulus and the hardness was caused by defect structures, high density, and the presence of reinforcing carbide strengthening throughout grain boundaries.

8.5 $MoSi_2$ Bulk Nanocomposite

- Near-net-shape $MoSi_2$–Si_3N_4–SiC bulk composite has been successfully consolidated with retained nanostructure using plasma spray forming.

- The average fracture toughness in the middle region of the bulk nanocomposite was 5 $MPa.m^{1/2}$.

- The higher fracture toughness could be attributed to the crack deflection by homogeneous distribution and the retention of nanostructures.

REFERENCES

[1]T. Sekino, T. Nakajima, K. Niihara, Mater. Lett. 29 (1996) 165.

[2]M. Sternitzke, J. Eur. Ceram. Soc. 17 (1997) 1061.

[3]R. Roy, R. A. Roy, D. M. Roy, Mater. Lett. 4 (1986) 323.

[4]H. Riedel, J. Kleebe, H. Schonfelder, F. Aldinger, Nature 374 (1995) 526.

[5]K. Niihara, J. Ceram. Soc. Japan 99 (1991) 974.

[6]D. N. Lambeth, E. M. T. Velu, G. H. Bellesis, L. L. Lee, D. E. Laughlin, J. Appl. Phys. 79 (1996) 4496.

[7]S. Ozkar, G. A. Ozin, R. A. Prokopowicz, Chem. Mater. 4 (1992) 1380.

[8]M. J. Mayo, Int. Mater. Rev. 41 (1996) 85.

[9]C. C. Koch, Nanostruct. Mater. 2 (1993) 109.

[10]W. D. Kingery, H. K. Bowen, D. R. Uhlmann, Introduction to Ceramics, John Wiley & Sons, New York, 1976.

[11]D. Goberman, Y.H. Sohn, L. Shaw, E. Jordan and M. Gell, "Microstructure development of Al_2O_3-13wt% TiO_2 plasma sprayed coatings derived from nanocrystalline powders," Acta Mater. 50[5] 1141-52 (2002).

[12]A. Killinger, M. Kuhn, R. Gadow, "High-Velocity Suspension Flame Spraying (HVSFS), a new approach for spraying nanoparticles with hypersonic speed" Surf. Coat. Technol. 201 [5], 1922-29 (2006).

[13]V. Viswanathan, R. Filmalter, S. Patil, S. Deshpande and S. Seal, "High-Temperature Oxidation Behavior of Solution Precursor Plasma Sprayed Nanoceria Coating on Martensitic Steels" J. Am. Ceram.Soc. (2007) Available online

[14]Wigren, J., Vries, J.-F. de. and Greving, D., Effects of powder morphology, microstructure, and residual stresses on thermal barrier coating thermal shock performance. In Thermal Spray: Practical Solutions for Engineering Problems, ed. C. C. Berndt. ASM International, OH, USA, 1996, pp. 855±861.

[15]Damani, R.J. and Makroczy, P., Heat Treatment Induced Phase and Microstructural Development in Bulk Plasma Sprayed Alumina. Journal of European Ceramic Society, 2000. 20: p. 867-888.

[16]Ramachandran, K., Selvarajan, V., Ananthapadmanabhan, P.V., and Sreekumar, K.P., Microstructure, adhesion, microhardness, abrasive wear resistance and electrical resistivity of the plasma sprayed alumina and alumina-titania coatings. Thin Solid Films, 1998. 315(1-2): p. 144-152.

[17]V. A. Parsegian, Van der Waals forces, Handbook for Biologists, Chemists, Engineers and Physicists, 2005, pp. 1-396.

[18]S. J. Hong, V. Viswanathan, K. Rea, S. Patil, S. Deshpande, P. Georgieva, T. McKechnie, "Plasma spray formed near-net-shape $MoSi_2$–Si_3N_4 bulk nanocomposites—structure property evaluation" Mater. Sci. Eng. A., 404[1-2] 165-72 (2005).

[19]V. Viswanathan, A. Agarwal, V. Ocelik, J. T. M. De Hosson, N. Sobczak, S. Seal, "High Energy Density Processing of a Free Form Nickel Alumina Nanocomposite" J. Nanosci. Nanotechnol., 6[3] 651-60 (2006).

[20]J. F. Bisson, M. Lamontagne, C. Moreau, L. Pouliot, J. Blain, and F. Nadeau, "Ensemble in-flight particle diagnostics under thermal spray conditions" Proceedings of International Thermal Spray Conference, Singapore, 2001 pp705-714.

[21]S. Brunauer, P.H. Emmett, E. J. Teller, "Adsorption of Gases in Multimolecular Layers" J. Am. Chem. Soc. 60, 309, (1938).

[22]K. Masters, Spray drying Handbook 1991, Fifth edition, pp 32-39.

[23] M. I. Boulos, P. Fauchais, E. Pfender, Thermal Plasmas Fundamentals and Applications, Vol. 1, Plenum Press, NY (1994) p 339.

[24]J. F. Coudert, M. P. Planche, P. Fauchais, "Characterization of DC plasma torch voltage fluctuations" Plasma. Chem. Plasma. Proc. 16[1], 47 (1995).

[25]M. Vardelle, A. Vardelle, P. Fauchais, M. I. Boulos, "Influence of particle parameters at impact on splat formation and solidification in plasma spraying processes", J. Therm. Spray Technol. 4[1] 50-58 (1995).

[26]I. Levin, L. A. Bendersky, D. G. Brandon, M. Ruhle, "Cubic to monoclinic phase transformations in Alumina" Acta Mater.45[9] 3659-69 (1997).

[27]I. Levin, D. Brandon, "Metastable Alumina Polymorphs: Crystal Structures and Transition sequences" J. Am. Ceram. Soc., 81[8] 4007 (1995).

[28]A. Agarwal, T. McKechnie, S. Seal, “Net Shape Nanostructured Aluminum Oxide Structures Fabricated by Plasma Spray Forming” J. Therm. Spray Technol, 12[3] 350-59 (2003).

[29]Cullity BD, Elements of X-Ray Diffraction, 2nd Edition, Addison Wesley Publishing Company, Reading MA 1978.

[30]Shillington EAG, Clarke DR, “Spalling failure of a Thermal Barrier Coating associated with aluminum depletion in the bond-coat” Acta Mater, 1999;47:1297.

[31]Y. Y. Chen, H. J. Tzeng, L. I. Wei, L. H. Wang, J. C. Oung and H. C. Shih, "Corrosion resistance and mechanical properties of low-alloy steels under atmospheric conditions," Corr. Sci., 47 [4] 1001-21 (2005).

[32]F. Smith, Principles of Materials Science and Engineering; McGraw Hill, New York, 777 pages, 1999.

[33]H. Sahlaoui, K. Makhlouf, H. Sidhom and J. Philibert, "Effects of ageing conditions on the precipitates evolution, chromium depletion and intergranular corrosion susceptibility of AISI 316L: experimental and modeling results," Mater. Sci. Eng., A, 372 [1-2] 98-108 (2004).

[34]H. Buscail and J. P. Larpin, "The influence of cerium surface addition on low-pressure oxidation of pure iron at high temperatures," Solid State Ionics, 92 [3-4] 243 (1996).

[35]R. J. Hussey, P. Papaiacovou, J. Shen, D. F. Mitchell and M. J. Graham, "The Effect of Ceria Coatings on the High-Temperature Oxidation of Iron-Chromium Alloys," Mater. Sci. Eng., A, 120 147-51 (1989).

[36]J. Stringer, "The Reactive Element Effect in High-Temperature Corrosion," Mater. Sci. Eng., A, 120 129-37 (1989).

[37]H. H. Uhlig and R. W. Revie, Corrosion and Corrosion Control; John Wiley and Sons, NewYork, 464 pages, 1985.

[38]M. Hocking, V. Vasantasree and P. Sidky, Metallic and Ceramic Coatings: High Temperature Properties and Applications; Wiley, NewYork, 252 pages, 1989.

[39]F. Riffard, H. Buscail, E. Caudron, R. Cueff, C. Issartel and S. Perrier, "Yttrium sol-gel coating effects on the cyclic oxidation behaviour of 304 stainless steel," Corr. Sci., 45 [12] 2867 (2003).

[40]C. Issartel, H. Buscail, E. Caudron, R. Cueff, F. Riffard, S. Perrier, P. Jacquet and M. Lambertin, "Influence of nitridation on the oxidation of a 304 steel at 800 degrees C," Corr. Sci., 46 [9] 2191 (2004).

[41]A. P. Tschiptschin, "Predicting Microstructure Development during high temperature nitriding of Martensitic stainless steels using Thermodynamic Modeling.," Materials Research, 5 [3] 257-64 (2002).

[42]S. Seal, S. K. Bose and S. K. Roy, "Improvement in the oxidation behavior of austenitic stainless steels by superficially applied, cerium oxide coatings," Oxid. Met., 41 [1 - 2] 139-78 (1994).

[43]S. Seal, S. K. Roy, S. K. Bose and S. C. Kuiry, "Ceria-Based High-Temperature Coatings for Oxidation Prevention," Journal of Materials, 52 [1] (2000).

[44]M. Gell, L. Xie, X. Ma, E. H. Jordan and N. P. Padture, "Highly durable thermal barrier coatings made by the solution precursor plasma spray process," Surface and Coatings Technology, 177 97-102 (2004).

[45]A. Agarwal, T. Mckechnie and S. Seal, "Net Shape Nanostructured Aluminum Oxide Structures Fabricated by Plasma Spray Forming," J. Therm. Spray Technol., 12 [3] 350-59 (2003).

[46]L. Xie, E. H. Jordan, N. P. Padture and M. Gell, "Phase and microstructural stability of solution precursor plasma sprayed thermal barrier coatings," Mater. Sci. Eng., A, 381 [1-2] 189 (2004).

[47]N. P. Padture, K. W. Schlichting, T. Bhatia, A. Ozturk, B. Cetegen, E. H. Jordan, M. Gell, S. Jiang, T. D. Xiao, P. R. Strutt, E. Garcia, P. Miranzo and M. I. Osendi, "Towards durable thermal barrier coatings with novel microstructures deposited by solution-precursor plasma spray," Acta Mater., 49 [12] 2251-57 (2001).

[48]J. Karthikeyan, C. C. Berndt, J. Tikkanen, S. Reddy and H. Herman, "Plasma spray synthesis of nanomaterial powders and deposits," Mater. Sci. Eng., A, 238 [2] 275-86 (1997).

[49]J. Karthikeyan, C. C. Berndt, S. Reddy, J. Y. Wang, A. H. King and H. Herman, "Nanomaterial deposits formed by DC plasma spraying of liquid feedstocks," J. Am. Ceram. Soc., 81 [1] 121 (1998).

[50]T. Bhatia, A. Ozturk, L. D. Xie, E. H. Jordan, B. M. Cetegen, M. Gell, X. Q. Ma and N. P. Padture, "Mechanisms of ceramic coating deposition in solution-precursor plasma spray," J. Mater. Res., 17 [9] 2363-72 (2002).

[51]B. Pateyron, M. F. Elchinger, G. Delluc and P. Fauchais, "Thermodynamic and transport properties of Ar-H_2 and Ar-He plasma gases used for spraying at atmospheric pressure. I: Properties of the mixtures," Plasma Chem. Plasma Process., 12 [4] 421-48 (1992).

[52]S. Deshpande, S. Patil, S. V. N. T. Kuchibhatla and S. Seal, "Size dependency variation in lattice parameter and valency states in nanocrystalline cerium oxide," Appl. Phys. Lett., 87 [13] 133113-1-3 (2005).

[53]L. Xie, X. Ma, E. H. Jordan, N. P. Padture, D. T. Xiao and M. Gell, "Identification of coating deposition mechanisms in the solution-precursor plasma-spray process using model spray experiments," Mater. Sci. Eng., A, 362 [1-2] 204-12 (2003).

[54]S. Patil, S. C. Kuiry and S. Seal, "Nanocrystalline ceria imparts better high-temperature protection," Proc. R. Soc. London, Ser. A, 460 [2052] 3569-87 (2004).

[55]F. Czerwinski and J. A. Szpunar, "Optimizing properties of CeO2 sol-gel coatings for protection of metallic substrates against high temperature oxidation," Thin Solid Films, 289 [1-2] 213-19 (1996).

[56]S. Seal, R. Nardelli, A. Kale, V. Desai and E. Armacanqui, "Role of surface chemistry on the nature of passive oxide film growth on Fe–Cr (low and high) steels at high temperatures," J. Vac. Sci. Technol., A, 17 [4] 1109-15 (1999).

[57]http://srdata.nist.gov/xps

[58]W.H. Tuan and R.J. Brook, J. Eur. Ceram. Soc. 6, 31 (1990)

[59]T. Sekino and K. Niihara, J. Mater. Sci. 32, 3943 (1997)

[60]T. Sekino and K. Niihara, J. Eur. Ceram. Soc. 18, 31 (1998)

[61]A.Nakahira and K.Niihara, Fract. Mech. 9, 165 (1992)

[62]Y.K. Jeong and K. Niihara, Nanostruct. Mater. 9, 193 (1997)

[63]S. C. Wang and W.C.J. Wei, Nanostruct. Mater. 10, 983 (1998)

[64]B. Budiansky, J.C. Amazigo and A.J. Evans, J. Mech. Phys. Solids, 36, 167 (1988)

[65]S.Ozkar, G.A. Ozin and R.A. Prokopowicz, Chem. Mater. 4, 1380(1992)

[66]S.T. Oh, T. Sekino and K. Niihara, J. Eur. Ceram. Soc. 18, 31–37 (1998)

[67]O.Aharon, S. Bar-Ziv, D.Gorni, T.Cohen-Hyams and W.D.Kaplan, Scripta Mater. 50,1209 (2004)

[68]T. Sekino, T. Nakajima and K. Niihara, Mater. Lett. 29,165 (1996)

[69]S.I. Cha, S.H. Hong and B.K.Kim, Mater. Sci. Eng. A 351, 31 (2003)

[70]S.Seal, S.C.kuiry, P.Georgieva and K.Rea, Scripta Mater. 50, 1237 (2004)

[71]R.Z.Chen and W.H Tuan, J. Eur. Ceram. Soc. 19, 463 (1999)

[72]M. Lieberthal and W.D. Kaplan, Mater. Sci. Eng. A 302, 83 (2001)

[73]K.Niihara, B.S. Kim, T. Nakayama, T. Kusunose, T. Nomoto, A. Hikasa and T. Sekino, J. Eur. Ceram. Soc. 24, 3419 (2004)

[74]U. L. Adisorn, T. Matsunaga, Y. Kobayashi, S.M. Choi and H. Awaji, Ceram. Intl. 31, 803 (2005)

[75]S. Seal, S.C. Kuiry, P. Georgieva and A. Agarwal, MRS Bull. 29, 16 (2004)

[76]J. Michalski, K. Konopka and M.Trzaska, Mater. Chem. Phys. 81, 407 (2003)

[77]A.G. Evans and E.A. Charles, J. Am. Ceram. Soc. 59, 371 (1976)

[78]W.H. Tuan and R.J. Brook, J. Eur. Ceram. Soc. 10, 95 (1992)

[79]W.H. Tuan and W.B. Chou, J. Am. Ceram. Soc. 80, 9, 2418 (1997)

[80]E. Breval, G. Dodds and C.G. Pantano, Mater. Res. Bull. 20,10,1191 (1985)

[81]E. Breval, Z. Deng, S. Chiou, and C.G. Pantano, J. Mater. Sci. 27, 1464 (1992)

[82]E.D. Rodeghiero, O.K. Tse, J. Chisaki and E.P. Giannelis, Mater. Sci. Eng. A 195, 151 (1995)

[83]J.F. Moulder, W.F. Stickle, P.E. Sobol and K.D. Bomben, in Handbook of X-Ray Photoelectron spectroscopy edited J. Chastain and R.C. King Jr., Physical Electronics Inc. Minnesota (1995), p.71.

[84]T.L. Barr and S. Seal, J. Vac. Sci. Technol. A13, 1239 (1995)

[85]E. Saiz, R. M. Cannon and A. P. Tomsia, Acta Mater. 47, 4209 (1999)

[86]W.D. Kingery, J. Am. Ceram. Soc. 37, 42 (1954)

[87]G. Palasantzas and J. Th. M. De Hosson, Acta. Mater. 49, 3533 (2001)

[88]N. Eustathopolous, Acta. Mater. 46, 2319 (1998)

[89]J. A. Vreeling, V. Ocelık, Y. T. Pei, D. T. L. Van Agterveld and J. Th. M.De Hosson, Acta mater. 48, 4225 (2000)

[90]R Ye, T. Ishigaki, J. Jurewicz, P. Proulx and M.I. Boulos, Plasma Chem. Plasma Process. 24, 555 (2004)

[91]A. Brenner and S. Senderoff, J Res. Natl. Bur. Stand. 42, 105 (1949)

[92]S. Kuroda and T.W. Clyne, Thin Solid Films 200, 49 (1991)

[93]M. W. Hunt, Guide to Engineering Materials, Adv. Mater. Proc. 158, 6 (2000)

[94]L.L.Shaw, D. Goberman, R. Ren, M. Gell, S. Jiang, Y. Wang, T.D. Xiao, and P.R.Strutt, Surf. Coat. Technol. 130, 1 (2000)

[95]O.D. Slagle and H.A. Mckinsky, J Appl. Phys. 38, 437 (1967)

[96]M. Vural, S. Zeytin, A.H.Ucisik, Surf. Coat. Technol. 97, 347 (1997)

[97]S. Seal, S.C. Kuiry, P. Georgieva, A. Agarwal, MRS Bull., 29 (2004) 16-21.

[98] B. J. Mac Donald, M. S. J. Hashmi, J. Mater. Proc. Technol., 120[1-3] (2002) 341-47.

[99]E. J. Lavernia, Q. J. Xu, Japan Inst. Light Met. 50 (2000) 479-485.

[100]R. B. Dandliker, R. D. Conner, W.L. Johnson, J Mater. Res. 13 (1998) 2896-2901.

[101]S. Yih and C. Wang., "Tungsten: Sources, Metallurgy, Properties and Applications", Plenum Publishing Corporation, New York, 1978, pp. 500-515.

[102]G. M. Song, Y. J. Wang and Y. Zhou, International Journal of Refractory Metals & Hard Materials, 21 (2003) 1-12.

[103]P. G. Caceres, Mater. Characterization, 49 (2002) 1-9.

[104]Y. Saito, T. Matsumoto, and K. Nishikubo, Carbon, 35[12] (1997) 1757-1763.

[105]M. Opeka, I. Talmy, E. Wuchina, J. Zaykoski and S. Causey, J. Eur. Ceram. Soc. 19, (1999) 2405-2414.

[106]O. Pierson, in Handbook of Refractory Carbides and Nitrides: Properties, Characteristics, Processing and Applications, Noyes Publications, New Jersey, 1996 pp. 331-334.

[107]A. C. Fischer-Cripps, Nanoindentation, Springer-Verlag, New York, 2002, pp. 265-269.

[108]E. Lavernia and Y. Wu, Spray Atomization and Deposition, John Wiley & Sons, West Sussex, 1996, pp. 627-631.

[109]A. Agarwal and T. McKechnie, Adv. Mater. Proc. 159, (2000) 44-46.

[110]W. C. Oliver and G. M. Pharr, J. Mater. Res. 7 (6) (1992) 1564- 1583.

[111]J. Alcala, A. E. Giannakopoulos, and S. Suresh, J. Mater. Res. 13(5) (1998) 1390-1400.

[112]P. Raffo and W. Klopp., NASA Technical Memorandum TM X-52131 (1965) 1-21.

[113]S. Rajagopalan and R. Vaidyanathan , J. Min. Met. Mat. S 54[9] (2002) 45-48.

[114]M. Boulos, "Powder Densification and Spheroidization Using Induction Plasma Technology" Metal Powder Report, 59 (2004) 16-21.

[115]S. L. Girshick, High Temp. Mater. Proc., 4 (2000) 379-384.

[116]G. Bertrand, C. Filiatre, H. Mahdjoub, A. Foissy, and C. Coddet, Journal of the European Ceramic Society, 23 (2003) 263-271.

[117]K. E. Rea, A. Agarwal, T. McKechnie and S. Seal, Microscopy Research Techniques, 66 (1) (2005) 10-17.

[118]S. Lukasiewicz., J. Am. Ceram. Soc. 72 [4] (1989) 617-624.

[119]T. Laha, A. Agarwal, T. McKechnie, K. Rea and S. Seal, Acta Mater. 53 (2005) 5429-5438.

[120]J. Li, H. Liao, X. Wang, C. Coddet, H. Chen, and C. Ding, Thin Solid Films 460[1-2] (2004) 101-115.

[121]J. D. Eshelby, Proc. Roy. Soc. London A 241 (1959) 376-396.

[122]O.B. Pederson, "Mean Field Theory and the Bauschinger effect in composites" in Proc. IUTAM Eshelby Mem. Symp. Sheffield, UK, K. J. Miller , B. Bilby and J. R. Willis (eds), Cambridge university press, Cambridge, 1989, pp. 263-273.

[123]G. E. Dieter, "Mechanical Metallurgy", McGraw-Hill, Boston, 2000, pp. 31-41.

[124]X. Cao, R. Vassen, S. Schwartz, W. Jungen, F. Tietz, D. Stoever, "Spray-drying of ceramics for plasma spray coating", J. Eur. Ceram. Soc., 20 (2000) 2433-2439.

[125]P. Raffo and W. Klopp, NASA Technical Memorandum TN D-3248 (1966) 1-12.

[126]Clark, J. S., Mincher, A. L., and Villee, G. N, Rept E. I. Du Pont de Nemours and Company. RTD-TDR 63 (1963) 4236.

[127]W. D. Klopp and W. R. Witzke, J. Less-Common Metals 24 (1971) 427-443.

[128]Y. Nakayama, S. Weissmann, and T. Imura, Proceedings of Technical Conference. Interscience Publishers, New York, 1962, pp. 93-95.

[129]F.D. Gac, J.J. Petrovic, J. Am. Ceram. Soc. 68 (8) (1985) 200.

[130]R.R. Giler, Met. Eng. Q. 48–52 (November) (1973).

[131]J.M. Yang, W. Kai, S.M. Jeng, Scr. Metall. 23 (1989) 1953–1958.

[132]J.J. Petrovic, R.E. Honnel, Ceram. Eng. Sci. Proc. 11 (7–8) (1990) 734–744.

[133]J.J. Petrovic, R.E. Honnell, Second International Ceramic Science and Technology Congress of the American Ceramic Society, 12–15 November 1990, Orlando, FL, American Ceramic Society, Columbus,OH, 1990, pp. 817–830.

[134]J.M. Yang, S.M. Jeng, J. Mater. Res. 6 (3) (1991) 505–513.

[135]A.K. Vasudevan, J.J. Petrovic, Mater. Sci. Eng. A 155 (1992) 1–17.

[136]H. Huang, L. Yin, L. Zhou, J. Mater. Process. Technol. 141 (2003) 329–336.

[137]T. Otani, M. Hirata, Thin Solid Films 442 (2003) 44–47.

[138]S. Ogata, N. Hirosaki, C. Kcer, Y. Shibutani, Acta Mater. 52 (2004) 233–238.

[139]M.G. Hebsur, Mater. Sci. Eng. A 261 (1999) 24–37.

[140]J.J. Petrovic, A.K. Vasudevan, Mater. Sci. Eng. A 261 (1987) 1–5.

[141]K. Sadananda, H. Jones, J. Feng, J.J. Petrovic, A.K. Vasudevan, Ceram. Eng. Sci. Proc. 12 (1991) 1671–1678.

[142]S. Shukla, S. Seal, Nanostruct. Mater. 11 (8) (1999) 1181–1193.

[143]G. Skandan, Nanostruct. Mater. 5 (2) (1995) 111–126.

[144]C.C. Berndt, J. Therm, Spray Technol. 10 (1) (2001) 147–182.

[145]J. He, M. Ice, J.M. Schoenung, D.H. Shin, E.J. Lavernia, J. Therm. Spray Technol. 10 (2) (2001) 293–300.

[146]Y. Zhu, K. Yukimura, C. Ding, P. Zhang, Thin Solid Films. 388 (2001) 277–282.

[147]Y. Wang, S. Jiang, M. Wang, S. Wang, T.D. Xiao, P.R. Strutt, Wear 237 (2000) 176–185.

[148]A. Agarwal, T. Mckechnie, NASA Goddard Space Flight Center, Technical Report NAS5-0008, November 2001.

[149]A. Agarwal, T. Mckechnie, S. Seal, J. Therm. Spray Technol. 12 (3) (2003) 350–359.

[150]A.G. Evans, E.A. Charless, J. Am. Ceram. Soc. 59 (1976) 371. [23] L. Holland, Surf. Technol. 11 (1980) 145–169.

[151]L. Holland, Surf. Technol. 11 (1980) 145–169.

[152]K. Upadhya, Proceedings of a Symposium Sponsored by the Structural Materials Division of TMS, TMS Annual Meeting, Denver, CO, February 22–25, 1993.

[153]M.G. Hebsur, Dev. Mater. Sci. Eng. A 261 (1999) 24–37.

[154]N. Ramakrishnan, Acta Mater. 44 (1996) 69.

[155]J.S. Jayashankar, E.N. Ross, P.D. Eason, M.J. Kaufman, Mater. Sci. Eng. A 239–240 (1997) 485–492.

[156]A. Newman, S. Sampath, H. Herman, Mater. Sci. Eng. A 261 (1999) 252–260.

[157]D.H. Carter, J.J Petrovic, R.E. Honnell, W.S. Gibbs, Re LA-11577-MS, Los Alamos National Laboratory, 1989.

[158]C.G. Mckamey, P.F. Tortorelli, J.H. Devan, C.A. Carmichael, J. Mater. Res. 7 (1992) 2747.

[159]S. Becker, A. Rahmel, M. Schutze, Solid State Ionics 53 (1992) 280.

[160]K. Kurokawa, H. Houzumi, I. Saeki, H. Takahashi, Mater. Sci. Eng. A 261 (1999) 292.

[161]H.J. Grabke, G.H. Meier, Oxide Met. 44 (1995) 147.

[162]D.A. Berztiss, R.R. Cerchiara, E.A. gulbransen, F.S. Pettit, G.H.Meier, Mater. Sci. Eng. A 155 (1992) 165–181.